Strain-balanced InAs-InAsSb Type-II Superlattices on GaSb Substrates for Infrared Photodetector Applications

by

Elizabeth H. Steenbergen

A Dissertation Presented in Partial Fulfillment
of the Requirements for the Degree
Doctor of Philosophy

Approved March 2012 by the
Graduate Supervisory Committee:

Yong-Hang Zhang, Chair
Gail Brown
Shane Johnson
Dragica Vasileska

ARIZONA STATE UNIVERSITY

May 2012

ABSTRACT

Infrared photodetectors, used in applications for sensing and imaging, such as military target recognition, chemical/gas detection, and night vision enhancement, are predominantly comprised of an expensive II-VI material, HgCdTe. III-V type-II superlattices (SLs) have been studied as viable alternatives for HgCdTe due to the SL advantages over HgCdTe: greater control of the alloy composition, resulting in more uniform materials and cutoff wavelengths across the wafer; stronger bonds and structural stability; less expensive substrates, i.e., GaSb; mature III-V growth and processing technologies; lower band-to-band tunneling due to larger electron effective masses; and reduced Auger recombination enabling operation at higher temperatures and longer wavelengths. However, the dark current of InAs/$Ga_{1-x}In_xSb$ SL detectors is higher than that of HgCdTe detectors and limited by Shockley-Read-Hall (SRH) recombination rather than Auger recombination. This dissertation work focuses on InAs/$InAs_{1-x}Sb_x$ SLs, another promising alternative for infrared laser and detector applications due to possible lower SRH recombination and the absence of gallium, which simplifies the SL interfaces and growth processes.

InAs/$InAs_{1-x}Sb_x$ SLs strain-balanced to GaSb substrates were designed for the mid- and long-wavelength infrared (MWIR and LWIR) spectral ranges and were grown using MOCVD and MBE by various groups. Detailed characterization using high-resolution x-ray diffraction, atomic force microscopy,

photoluminescence (PL), and photoconductance revealed the excellent structural and optical properties of the MBE materials.

Two key material parameters were studied in detail: the valence band offset (VBO) and minority carrier lifetime. The VBO between InAs and $InAs_{1-x}Sb_x$ strained on GaSb with $x = 0.28 – 0.41$ was best described by $Q_v = \Delta E_v/\Delta E_g = 1.75 \pm 0.03$. Time-resolved PL experiments on a LWIR SL revealed a lifetime of 412 ns at 77 K, one order of magnitude greater than that of $InAs/Ga_{1-x}In_xSb$ LWIR SLs due to less SRH recombination. MWIR SLs also had 100's of ns lifetimes that were dominated by radiative recombination due to shorter periods and larger wave function overlaps. These results allow $InAs/InAs_{1-x}Sb_x$ SLs to be designed for LWIR photodetectors with minority carrier lifetimes approaching those of HgCdTe, lower dark currents, and higher operating temperatures.

This work is dedicated to my loving husband, John Leon Steenbergen, who has sacrificed much during the past five years to support and encourage me to reach my full potential.

ACKNOWLEDGEMENTS

First of all, I would like to acknowledge my advisor, Dr. Yong-Hang Zhang, for challenging me technically, for inspiring me to dig deeper into physics, for working with me to find a project that overlapped with my future work at AFRL due to the SMART scholarship, and for support and encouragement to attend multiple conferences. I thank my mentor at AFRL, Dr. Gail Brown, for many helpful discussions, learning photoconductance measurements in her lab, and for access to x-ray diffraction, AFM, and photoluminescence measurements at AFRL. Dr. Shane Johnson taught me the importance of excellent scientific writing and a lot about hiking in the desert. Dr. Dragica Vasileska taught me excellence in modeling and to be sure to understand the physics behind the models and code.

Without the support of many others, this work would not have been accomplished. At AFRL/RXPS, I am thankful for Gerry Landis helping me to etch samples, Larry Grazulis acquiring and interpreting AFM data, Dr. Kurt Eyink for numerous discussions, Dr. David Tomich for x-ray diffraction discussions, Dr. Bruno Ullrich for teaching me how to run the PL measurements, and Dr. Frank Szmulowicz for the three-band EFA model and many theory discussions. I appreciate Dr. Said Elhamri at the University of Dayton providing temperature-dependent Hall data. At IQE, I thank Drs. Amy Liu, Joel Fastenau, Dmitri Loubychev, and Yueming Qiu for MBE growth of the last set of samples in this work. At Georgia Institute of Technology, Dr. Russ Dupuis, Dr. Jae-Hyun Ryou,

and Dr. Yong Huang were responsible for the MOCVD-grown samples. At UCLA, Dr. Kalyan Nunna did the MBE growth of two sets of samples with support from Dr. Dianna Huffaker. At ASU, I thank Dr. Oray Orkun Cellek for helping with PL measurements, teaching me more about the FTIR and infrared detectors, and many excellent discussions. I also thank my research group at ASU for numerous conversations: Dr. Ben Green, Dr. Robin Scott, Jing-Jing Li, Songnan Wu, Jin Fan, Michael DiNezza, Hank Dettlaff, Dr. Kevin O'Brien, Dr. Ding Ding, and Dr. Shui-Qing (Fisher) Yu. At ARL, Dr. Blair Connelly spent two weeks of long days helping me to acquire the time-resolved PL data, and Dr. Grace Metcalfe, Dr. Michael Wraback, and Dr. Paul Shen helped to interpret the results.

In addition, funding from several sources has made this work possible. My first year of graduate school was funded by the Science Foundation Arizona and the next four years funded by the Department of Defense SMART scholarship. Two years of generous funding from the Douglas family through the ARCS Foundation enabled me to attend several conferences and obtain samples from IQE, Inc. The ASU Graduate and Professional Student Association grant from the ASU Office of the Vice-President for Research and Economic Affairs, the Graduate Research Support Program, and the Graduate College funding allowed GaSb substrates to be bought. Also, I am grateful for the funding support of ARO MURI program W911NF-10-1-0524 and AFOSR Grant FA9550-10-1-0129.

"Lord, you establish peace for us; all that we have accomplished you have done for us."

Isaiah 26:12 NIV

TABLE OF CONTENTS

APPENDIX Page

LIST OF TABLES

TABLE Page

TABLE Page

LIST OF FIGURES

FIGURE Page

FIGURE Page

FIGURE Page

FIGURE Page

FIGURE Page

FIGURE Page

FIGURE Page

FIGURE Page

FIGURE Page

LIST OF ACRONYMS

AFM – atomic force microscopy

IR - infrared

LPE – liquid phase epitaxy

LWIR – long-wavelength infrared (8-12 μm)

MBE – molecular beam epitaxy

MOCVD – metalorganic chemical vapor deposition

MOVPE – metalorganic vapor phase epitaxy

MWIR – mid-wavelength infrared (4-6 μm)

PL – photoluminescence

SLS - strained-layer superlattice

SL - superlattice

TRPL – time-resolved photoluminescence

T2SL – type-II superlattice

XRD – x-ray diffraction

1. INTRODUCTION

Infrared photodetectors are useful for many sensing and imaging applications, including chemical/gas detection and identification, industrial automation and electrical wiring/thermal loss diagnostics, night vision enhancement for aviation, automobiles, and heavy equipment, astronomy, airborne spectroscopy, and military target acquisition and identification. Several direct bandgap materials are used to cover the infrared range, such as InSb, PbSnTe, and HgCdTe, but HgCdTe is the most prominent material today for the mid-wavelength and long-wavelength infrared (MWIR and LWIR) ranges and has been studied since the 1960s. The composition can be tuned to cover the optical spectral range 1-20 μm, and after being investigated for over 50 years, the material crystalline quality has substantially improved, the doping is accurately controlled, and the surfaces and band structure are well understood [1]. The minority carrier lifetime of state of the art LWIR HgCdTe detectors is limited by intrinsic Auger recombination [2], and the small effective mass results in a lower limit of tunneling currents that may practically limit the longest detectable wavelength to 20 μm [1].

Type-II superlattices (T2SL) enable bandgap engineering which results in larger effective masses and greater Auger recombination suppression than in HgCdTe, giving T2SLs the potential to reach longer wavelengths and to operate at higher temperatures [1]. These T2SLs enable energy transitions that are smaller than the bandgaps of the constituent materials, even far beyond the smallest bandgap of any unstrained bulk III-V material, which is 9 μm for

$InAs_{0.39}Sb_{0.61}$ at 77 K [6]. The following advantages make III-V SL photodetectors viable alternatives for expensive HgCdTe infrared detectors: greater control of the alloy composition, resulting in more uniform materials and cutoff wavelengths across the wafer [7]; stronger bonds and structural stability [8]; less expensive, closely lattice-matched substrates, i.e., GaSb [9]; mature III-V growth and processing technology [9]; lower band-to-band tunneling due to larger electron effective mass [7]; and strain band edge engineering in combination with larger effective masses reducing Auger recombination [7, 9-11].

T2SLs have been extensively investigated for infrared applications since their initial proposal [3, 4], and the first $InAs/Ga_{1-x}In_xSb$ SL experimental demonstration [5]. Recently, MWIR and LWIR focal plane arrays using $InAs/Ga_{1-x}In_xSb$ SLs have been demonstrated by several groups [12-16]. The dark current of $InAs/Ga_{1-x}In_xSb$ SL detectors is decreasing and approaching that of HgCdTe detectors [9, 2], but the minority carrier lifetime of the $InAs/Ga_{1-x}In_xSb$ SLs is limited by Shockley-Read-Hall (SRH) recombination and the background carrier concentration is considerably higher than that of HgCdTe [17]. For high performance photodetectors, the normalized thermal generation rate, which is proportional to the thermal carrier concentration and inversely proportional to the carrier lifetime and absorption, must be minimized to increase the signal to noise ratio [1]. Thus, longer carrier lifetimes and lower background carrier concentrations are desirable.

$InAs/InAs_{1-x}Sb_x$ SLs represent another alternative for infrared laser and detector applications [18] due to possible lower SRH recombination [19] and the

absence of gallium (Ga), which simplifies the SL interfaces and the growth process [20, 31, 33]. An ideal theoretical comparison of a 10-μm InAs/$InAs_{1-x}Sb_x$ SL with an 11-μm InAs/$Ga_{1-x}In_xSb$ SL on GaSb substrates revealed that the performance of the InAs/$Ga_{1-x}In_xSb$ SL only slightly exceeds that of the InAs/$InAs_{1-x}Sb_x$ SL so that the real distinction between choice of materials will possibly come from practical, growth-related variations [19]. With the major improvements in molecular beam epitaxy (MBE) and metalorganic chemical vapor deposition (MOCVD) technologies in the last couple of decades, it is an ideal time to investigate the InAs/$InAs_{1-x}Sb_x$ SL system experimentally using both methods. MOCVD technology compared to MBE has very high throughput, which is desirable for mass production, and thus is worth investigating despite it being a challenge to grow high-quality antimonides compared to MBE at present.

To be suitable for infrared detectors, high-quality materials that are several microns thick are necessary, which can be achieved via strain-balancing the individual SL layers on the substrate to minimize misfit dislocations. Despite GaSb substrates being the best choice for strain-balancing InAs/$InAs_{1-x}Sb_x$ SLs without complicated metamorphic buffer layers, the growth of InAs/$InAs_{1-x}Sb_x$ SLs on GaSb is the least reported, with only a couple of demonstrations of MBE-grown [21, 33] and MOCVD-grown SLs [20, 22]. GaSb is the ideal substrate for strain-balancing InAs/InAsSb SLs due to its lattice constant being between that of the two layers, eliminating the need for complicated metamorphic buffer layers, and thus simplifying the growth process [20]. As the Sb concentration in the $InAs_{1-x}Sb_x$ layer increases, the strain of the layer on GaSb increases, making the

growth more difficult; but reaching LWIR wavelengths (8 – 12 μm) requires higher Sb concentrations to maintain larger electron-hole wave function overlaps for stronger absorption. This study sought to investigate InAs/$InAs_{1-x}Sb_x$ T2SLs with higher Sb concentrations of $x \leq 0.41$ which had not been previously explored. First, however, a review of the previous work on InAs/$InAs_{1-x}Sb_x$ T2SLs will be given.

1.1 A brief history of InAs/$InAs_{1-x}Sb_x$ superlattices

Figure 1 gives a brief history of antimonide SLs and the InAs/$InAs_{1-x}Sb_x$ SL in the form of a timeline. The semiconductor SL, a periodic one-dimensional variation in the semiconductor potential or band structure due to doping [35] or heterostructures, was first proposed in 1970 by Esaki and Tsu [3]. Electron tunneling through the periodic potential barriers and the large period with respect to the lattice constant, which reduced the size of the Brillouin zone, sparked great interest in the unique transport properties of SLs. The development of MBE in the early 1970's enabled GaAs/AlGaAs type-I SLs to be experimentally investigated due to the accurate control of atomic layer growth, leading to abrupt interfaces between different materials [36]. Type-II staggered and broken-gap SLs, based on InAs/GaSb and $In_{1-x}Ga_xAs/GaSb_{1-y}As_y$, with the conduction band in GaSb strongly interacting with the valence band in InAs, were introduced in 1977 [4] and first experimentally demonstrated in 1978 [5]. These SLs show a strong dependence of the bandgap on the layer thicknesses and require Bloch wave function solutions rather than plane wave solutions, unlike the previously

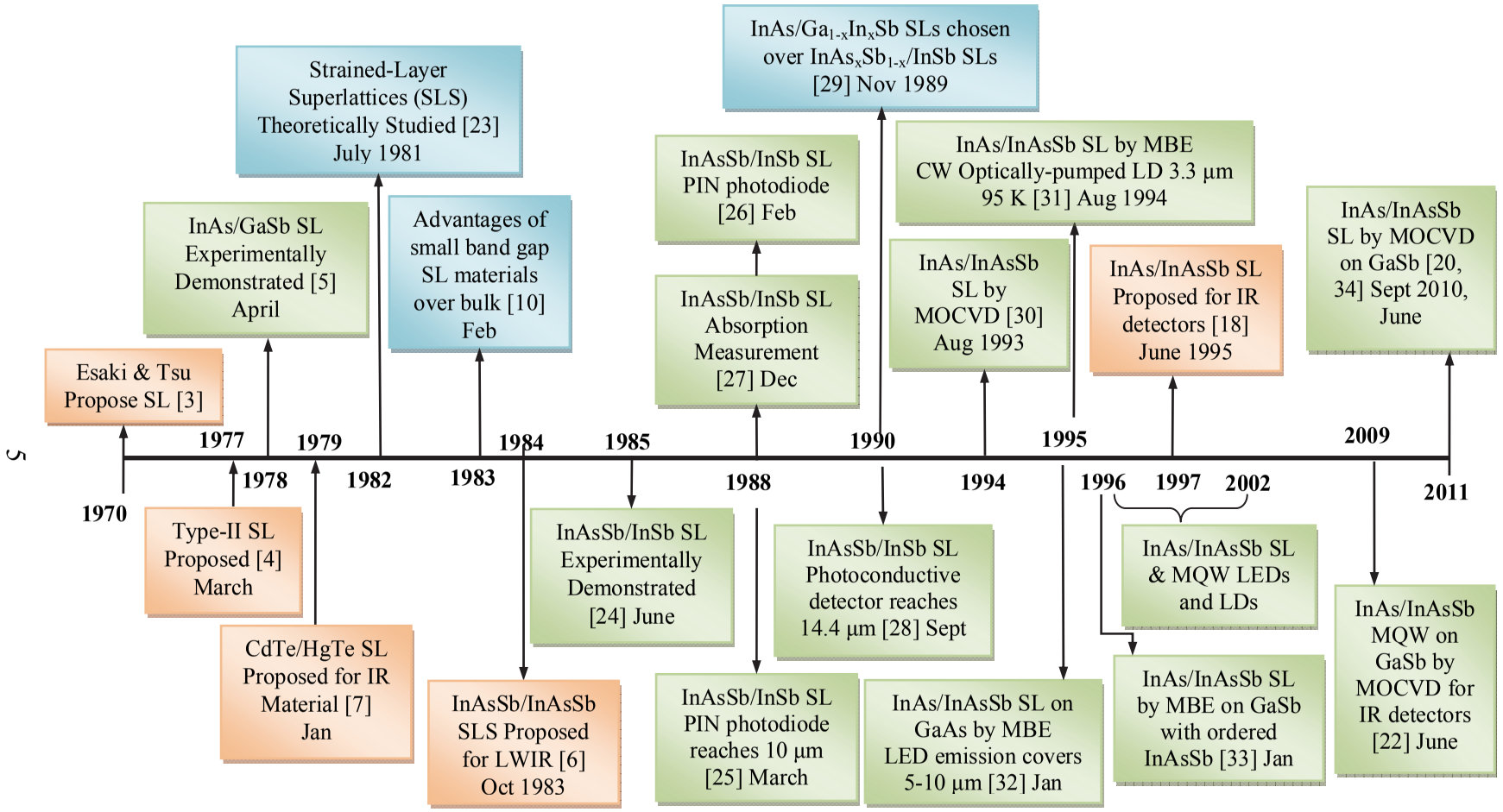

Figure 1. A timeline showing an overview of the history of the InAs/InAs$_{1-x}$Sb$_x$ SL. The orange signifies a proposal, the blue a theoretical study, and the green an experimental report. The submission dates are listed after the reference number.

proposed SLs with noninteracting conduction and valence bands between the two materials. The bandgap varying independently of the lattice constant by changing the layer thicknesses was a novel property of SLs compared to bulk materials [37].

The CdTe/HgTe SL was suggested for an infrared detector material [7] due to its many advantages over bulk HgCdTe: i) shorter tunneling length, defined as the length for wave function exponential decay in forbidden energy regions, suggested less band-to-band tunneling across pn junctions; ii) less fractional precision required for the SL layer thicknesses than the alloy composition for the same cutoff wavelength tolerance; and iii) higher electron effective mass perpendicular to the SL layers reduced electron diffusion and p-region diffusion currents in photovoltaic detectors [10]. These advantages were significant for arrays of photovoltaic detectors for infrared imaging and were expected to hold true for other small bandgap zinc blende semiconductors, such as InAs and InSb, that also have very small electron effective masses and large tunneling lengths [10].

With these advantages in mind, $InAs_{0.4}Sb_{0.6}/InAs_{1-x}Sb_x$ strained-layer superlattices (SLSs) were theoretically proposed for LWIR detectors as a competitor to bulk HgCdTe [23]. The LWIR (8 – 12 μm) window was of interest for detectors due to its minimal atmospheric absorption and high room temperature blackbody radiation flux. These SLSs had the advantages of III-V metallurgy and device processing and less bandgap dependence on the composition, which offered better material uniformity for focal plane arrays.

Auger recombination may also be reduced due to the increased electron effective mass and the substantial splitting of the light- and heavy-hole bands due to strain [11]. At the time of this proposal, conventional bulk III-V materials were not expected to cover the entire 8 – 12 μm range, with $InAs_{0.39}Sb_{0.61}$ having the longest cutoff wavelength of 9 μm at 77 K, but a more recent study found a longer wavelength for $InAs_{0.39}Sb_{0.61}$ of 11.4 μm at 77 K [38]. Several $InAs_{0.4}Sb_{0.6}/InAs_{1-x}Sb_x$ SLS designs with $x > 0.73$ could have effective bandgaps reaching 12 μm for the conduction-to-light-hole transition in the $InAs_{0.4}Sb_{0.6}$ layer [6]. This was a spatially direct transition in one layer of the SL (the spatially indirect type-II electron-to-heavy-hole transition was mentioned but not treated). An additional advantage of the III-V SLS over the II-VI bulk HgCdTe is the increased bond strength and structural stability shown by the difference in the microhardness values (InSb 220, InAs 330, and $Hg_{0.8}Cd_{0.2}Te$ 37 kg/mm^2) and shown indirectly by the growth temperatures (SLS 425 – 475 ºC) versus HgCdTe 200 ºC) [8]. The importance of the structural strength advantage is expected to appear in the device yield, reliability, and radiation tolerance [8].

Unlike the initially proposed SLs, SLSs are not composed of lattice-matched (mismatch less than 0.1%) materials, which introduces strain as an additional variable affecting the SL bandgap [23]. Lattice mismatch up to 7% can be accommodated without dislocation formation if the layers are thin enough [39]. The thickness of the layers is limited by the critical thickness, above which misfit dislocations occur and degrade the material quality [40]. Graded buffer layers have been used to generate the average lattice constant of the free-standing SL to

reduce the dislocations generated at the substrate-SL interface [39, 41], but this complicates the structure growth. The strain effects that can lower the superlattice bandgap are in competition with the quantum size effects that increase the SL bandgap as the layers become thinner. Thinner layers allow greater overlap between the electron and hole wave functions for these type-II SLs.

Some researchers chose to invest in InAs/$In_xGa_{1-x}Sb$ SLSs instead of $InAs_xSb_{1-x}$/InSb SLs because the $InAs_xSb_{1-x}$/InSb SLs required comparatively thick periods (75 Å vs 40 Å [11]) to reach the far infrared [29]. Thicker layers decrease the wave function overlap, as the spatial separation between electrons and holes is increased, and degrade the optical absorption [29], which is proportional to the wave function overlap and the density of states. However, the InAs/$In_xGa_{1-x}Sb$ and InAs/$InAs_xSb_{1-x}$ SL material systems have many similarities: both i) can be lattice-matched to GaSb; ii) can cover 8-14 μm; iii) use an intrinsic, type-II, spatially indirect, valence-to-conduction band transition for absorption [11]; and iv) use strain to reduce the SL bandgap [29]. A theoretical comparison of an ideal 10 μm (70.7 Å) InAs/(21Å) $InAs_{0.61}Sb_{0.39}$ SL and an 11 μm (39.8 Å) InAs/(15 Å) $In_{0.4}Ga_{0.6}Sb$ SL on a GaSb substrate cited even more similarities: i) suppressed band-to-band Auger recombination; ii) InAs and GaSb have similar lattice constants, as well as $In_xGa_{1-x}Sb$ and $InAs_{1-x}Sb_x$ having similar lattice constants for the same x; and iii) similar heavy-to-light-hole band splitting [19]. The InAs/$InAs_{1-x}Sb_x$ SL may have the advantage of fewer mid-gap states for SRH recombination if the intrinsic point defect levels in InAs-rich alloys are indeed in

or near the conduction band instead of in the middle of the bandgap [19, 42]. The theoretically calculated absorption was higher, approximately 2000 cm^{-1} versus 1500 cm^{-1}, in the InAs/$In_{0.4}Ga_{0.6}Sb$ SL than in the InAs/$InAs_{0.61}Sb_{0.39}$ SL due to its thinner layers and thus larger wave function overlap and larger optical matrix element [19]. However, an absorption coefficient of 1500 cm^{-1} does not rule out the InAs/$InAs_{1-x}Sb_x$ SL as an LWIR photodetector material. In fact, the authors claimed the theoretical performance of the InAs/$In_xGa_{1-x}Sb$ SL only *slightly* exceeds that of the InAs/$InAs_{1-x}Sb_x$ SL and thus the real distinction may come from practical, growth-related variations since SRH recombination was neglected in the comparison [19].

In the past fifteen to twenty years, the technology involved in MBE and MOCVD growth has changed and been greatly improved. With improved growth capabilities, it is reasonable to further investigate the InAs/$InAs_{1-x}Sb_x$ SL on GaSb substrates to see if they are indeed comparable to InAs/$In_xGa_{1-x}Sb$ SLs for MWIR and LWIR photodetectors. The absence of Ga in the InAs/$InAs_{1-x}Sb_x$ SL may simplify interface configurations and the growth process, making these SLs a more practical alternative technology to the InAs/$In_xGa_{1-x}Sb$ SLs for infrared detectors.

Appendix A tabulates the previously studied $InAs_{1-x}Sb_x$/$InAs_{1-x}Sb_x$ SL structures. Note that only three entries in the table were grown on GaSb substrates, and most of the other growths used metamorphic buffer layers, indicating very little investigation of these SLs grown strain-balanced on GaSb has been done in the past. Therefore, this study has addressed the design of

strain-balanced InAs/$InAs_{1-x}Sb_x$ T2SLs on GaSb (Chapter 2), the structural and optical characterization of MOCVD- (Chapter 3) and MBE-grown (Chapter 4) SLs, the valence band offset between InAs and $InAs_{1-x}Sb_x$ (Chapter 5), and the minority carrier lifetime of a set of InAs/$InAs_{1-x}Sb_x$ T2SLs (Chapter 6). Conclusions and future recommendations are given in Chapter 7.

2. MODELING

The procedure used to design strain-balanced InAs/$InAs_{1-x}Sb_x$ SLs on GaSb with particular transition energies is shown in the flowchart in Figure 2. InAs/$InAs_{1-x}Sb_x$ SLs can be strain balanced on GaSb by choosing appropriate combinations of layer thicknesses and $InAs_{1-x}Sb_x$ compositions. In order to achieve high quality materials with low misfit dislocation densities, the critical thicknesses [40] of InAs and $InAs_{1-x}Sb_x$ on GaSb are used as the upper limits for the layer thicknesses in the strain-balanced SL designs. To attain strain-balance, the average in-plane stress for the tensile and compressive layer pair should be zero. The zero-stress method [43], which takes the elastic constants of the layers into account, is used rather than the thickness-weighted method for strain-

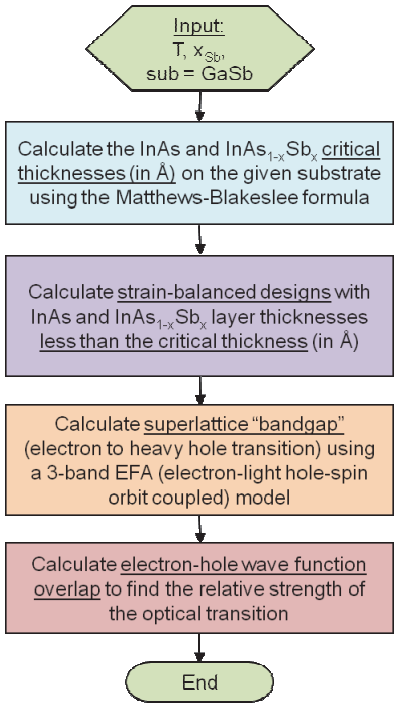

Figure 2. Flowchart describing the design process for strain-balanced InAs/$InAs_{1-x}Sb_x$ T2SLs.

balancing the InAs and $InAs_{1-x}Sb_x$ layers because it is more exact; however, the thickness-weighted method may be sufficient in this specific case due to the similar Poisson ratios for InAs and InSb. Once the strain-balanced layer thicknesses are known, they are used in a three-band envelope function approximation model [44], which includes coupling between the electrons, light holes, and spin-orbit split-off holes, to calculate the SL effective bandgap defined as the electron-to-heavy-hole transition energy. The corresponding wave functions for the electron and heavy hole are used to calculate the wave function overlap, which allows comparison of the relative strength of the optical transition for different designs.

The calculated results are highly dependent upon the material parameters that are entered into the model. The InAs, InSb, and $InAs_{1-x}Sb_x$ parameters were taken from a comprehensive review paper with consistent sets of parameters for III-V materials [45]. The band alignment of InAs and $InAs_{1-x}Sb_x$ was debated for several years between type-I, type-IIa (electron well in the alloy layer), and type-IIb (electron well in the binary layer). The type-I alignment was reported for samples with low Sb compositions and ordering present in the $InAs_{1-x}Sb_x$ layer[46], which lowered the alloy's bandgap. The results of a first principles band structure calculation method paralleling a core photoemission measurement agreed that the type-I alignment was possible for low Sb compositions when ordering is present due to the small type-IIb conduction band offset [47]. However, without ordering and in the presence of strain, the calculated alignment is type-IIb [47]. The opposing type-IIa alignment is supported by contradictory

results obtained from reduced-mass measurements [48, 49] from which the type-IIa alignment was chosen as a better fit to the data. Nonetheless, supporters of type-IIa stated that apart from interface defects interfering with the band alignment, a large bowing of the $InAs_{1-x}Sb_x$ valence band is necessary for the $InAs/InAs_{1-x}Sb_x$ type-IIb alignment to be compatible with the accepted type-II $InAs_{1-x}Sb_x/InSb$ alignment [49]. Recent studies using the type-IIb alignment have found the bowing of the $InAs_{1-x}Sb_x$ valence band to be between 60 – 70% of the bandgap bowing [22, 50, 51], contrary to the widely accepted expectation that the majority of the bowing in III-V materials occurs in the conduction band. The initial calculations presented here are based on the type-IIb alignment with 65% of the $InAs_{1-x}Sb_x$ bandgap bowing attributed to the valence band and an InAs/InSb valence band offset of 0.59 eV [45].

The individual sections of the calculation, as shown in the flowchart, are discussed in more detail in the following subsections.

2.1 Critical thickness

When a thin layer of a material is grown on a substrate with a different lattice constant, the lattice misfit is accommodated by strain in the layer until a certain layer thickness is reached. Above this critical thickness, dislocations occur to accommodate the misfit. These dislocations negatively impact the electronic properties of the materials by causing undesirable energy levels in the crystals that degrade the device performance.

Matthews and Blakeslee [40] developed a model to calculate the critical thickness using a mechanical balance between two forces: the tension in the

dislocation line and the stress due to the film strain. They started with an existing dislocation line at the interface, and the result is the following expression for zinc blende (001) substrates

$$h_c = \frac{a_o\left(1-\frac{\upsilon}{4}\right)\left[\ln\left(\frac{\sqrt{2}h_c}{a_o}\right)+1\right]}{\sqrt{2}\pi|f|(1+\upsilon)}, \quad (1)$$

$$f = \frac{(a_o - a_l)}{a_l}, \quad (2)$$

$$\upsilon = \frac{C_{12}}{C_{11}+C_{12}}, \quad (3)$$

where f is the layer strain when on the substrate, a_o is the substrate lattice constant, a_l is the layer lattice constant, υ is Poisson's ratio, C_{11},C_{12} are the elastic constants of the layer, and h_c is the critical thickness. The critical thickness for various structures is shown in Table 1 when using Eq. (1).

Table 1. Critical thickness values for different layer structures using Eq. (1).

Structure	Critical Thickness
Superlattice	h_c
Quantum Well	$\frac{h_c}{2}$
Single Strained Layer	$\frac{h_c}{4}$

An approximation for Matthews and Blakeslee's expression for the quantum well case obtained from energy minimization is [52]

$$h_c = \frac{a_l}{2f}. \quad (4)$$

People and Bean calculated the critical thickness using only energy considerations [53] instead of mechanical forces. Their calculations were based on screw dislocations having the smallest energy density of the different defects,

and their system had no dislocations to begin with. The strain energy density is balanced with the screw dislocation energy density to obtain the critical thickness for single layers on zinc blende (001) substrates

$$h_c = \frac{a_o^2(1-\upsilon)\ln\left(\frac{\sqrt{2}h_c}{a_o}\right)}{32\sqrt{2}\pi f^2 a_l(1+\upsilon)}. \tag{5}$$

Downes, Dunstan, and Faux [54, 55] numerically calculated the elastic energy for an edge dislocation, compared the numerical calculations to the Matthews-Blakeslee expression in Eq. (1), and modified the Matthews-Blakeslee expression for the critical thickness for generation of an edge dislocation dipole in a single layer on a substrate with a cap layer (quantum well)

$$h_c = \frac{a_o \ln\left|\frac{\sqrt{2}h_c}{a_o}+1\right|}{4\pi\sqrt{2}f^2(1+\upsilon)}. \tag{6}$$

People and Bean investigated Ge_xSi_{1-x} on Si substrates while Matthews and Blakeslee's work was based on multi-layers of GaAs and $GaAs_{0.5}P_{0.5}$ on GaAs substrates. The Matthews-Blakeslee expression for critical thickness of GeSi on Si resulted in smaller values than experimental results for misfit less than 1.4% and greater values for misfits up to 3% [53]. Downes *et al.* agree with the Matthews-Blakeslee expression (Eq. 1) for an infinite strained layer with an infinite dislocation, but for short dislocations with end effects or for small critical thicknesses (i.e. h_c divided by the Burgers vector ≤ 20), they state Eq. (1) is not valid. In fact, the Matthews-Blakeslee expression is double-valued for strains less than ~0.03 and may not give results at all for larger strains. For strain higher than

0.01, the Matthews-Blakeslee expression did not agree with their calculations due to only one dislocation being considered in the derivation rather than the interaction of the two dipole dislocations.

Understanding the applications and limitations of the different critical thickness expressions leads to using the critical thickness calculations as a guideline rather than a specific rule. Experimentally, the critical thickness may be higher than the calculated value, but to be conservative, the SLs in this work are designed with layers thinner than the single strained layer critical thickness from Eq. (1). As an example, consider the critical thicknesses of InAs and InSb on a (001) GaSb substrate at 300 K as shown in Table 2. The different methods give critical thicknesses that vary by an order of magnitude.

Table 2. Critical thicknesses of InAs and InSb on (001) GaSb.

Structure	Matthews and Blakeslee [40] $h_c\ (nm)$	$Approx$ [52] $h_c\ (nm)$	People and Bean [53] $h_c\ (nm)$
	InAs		
Superlattice	95.4		
Quantum Well	47.7	48.8	
Single Strained Layer	23.9		361.3
	InSb		
Superlattice	5.5		
Quantum Well	2.8	5.5	
Single Strained Layer	1.4		Not solvable

2.2 Strain balance

The critical thickness limits the thickness of dislocation-free materials grown under strained conditions, but if two layers under alternating tension and compression are strain-balanced, there will be no shear forces at the interfaces to generate dislocations [43] and the total thickness of the repeating layers should, in principle, be unlimited. Strain-balanced is defined as zero average in-plane stress

for the compressively/tensile strained layers [43]. The InAs and $InAs_{1-x}Sb_x$ superlattice layers alternate between tension and compression with equal in-plane lattice constants when pseudomorphically grown on GaSb [39]. The conduction band shifts up for layers under tensile strain and down for layers under compressive strain, and the degenerate valence bands at the Γ point are split, with the heavy hole band shifting up under compressive strain and the light hole band shifting up under tensile strain [56]. The equations describing the shifts in the band edges due to strain, $\delta E_c, \delta E_{v\_LH}, \delta E_{v\_HH}, \delta E_{v\_SO}$, are given below [44],

$$\varepsilon_{\parallel} = \frac{a_o}{a_l} - 1, \tag{7}$$

$$a_{\perp} = a_l \left(1 - 2\frac{C_{12}}{C_{11}}\varepsilon_{\parallel}\right), \tag{8}$$

$$\varepsilon_{\perp} = \frac{a_{\perp}}{a_l} - 1, \tag{9}$$

$$\frac{\Delta\Omega}{\Omega} = 2\varepsilon_{\parallel} + \varepsilon_{\perp}, \tag{10}$$

$$\Delta E = 2b_l(\varepsilon_{\perp} - \varepsilon_{\parallel}), \tag{11}$$

$$\delta E_c = a_c \frac{\Delta\Omega}{\Omega}, \tag{12}$$

$$\delta E_{v\_LH} = a_v \frac{\Delta\Omega}{\Omega} + \frac{\Delta E}{2}, \tag{13}$$

$$\delta E_{v\_HH} = a_v \frac{\Delta\Omega}{\Omega} - \frac{\Delta E}{2}, \tag{14}$$

$$\delta E_{v\_SO} = a_v \frac{\Delta\Omega}{\Omega}, \tag{15}$$

where $\varepsilon_{\parallel}$ and $\varepsilon_{\perp}$ are the parallel and perpendicular layer strains when on the substrate, a_o is the substrate lattice constant, a_l is the layer lattice constant, C_{11},

C_{12} are the elastic constants of the layer, a_c, a_v, are hydrostatic deformation potentials, and b_l is a shear deformation potential of the layer.

There are three common expressions used for strain-balancing. The average-lattice method uses the thickness average of the lattice parameters for the compressive and tensile layers [43]

$$a_o = \frac{t_1 a_1 + t_2 a_2}{t_1 + t_2}. \tag{16}$$

a_o is the substrate lattice constant, a_1, a_2 are the relaxed layer lattice constants, and t_1, t_2 are the layer thicknesses.

The thickness-weighted method uses a force balance argument resulting in the strain-thickness products being equivalent for the tensile and compressive layers

$$t_1 \epsilon_1 + t_2 \epsilon_2 = 0, \tag{17}$$

$$\epsilon_i = \frac{(a_o - a_i)}{a_i}, \tag{18}$$

$$a_o = \frac{(t_1 + t_2) a_1 a_2}{t_1 a_2 + t_2 a_1}. \tag{19}$$

The above two methods are physically intuitive but assume that the elastic constants of the two layers are equal. Accounting for the difference in elastic constants by using the parameter A [43], defined below for cubic lattices,

$$A = C_{11} + C_{12} - \frac{2C_{12}^2}{C_{11}}, \tag{20}$$

the thickness-weighted expression becomes

$$A_1 t_1 \epsilon_1 + A_2 t_2 \epsilon_2 = 0, \tag{21}$$

$$a_o = \frac{(A_1 t_1 + A_2 t_2) a_1 a_2}{A_1 t_1 a_2 + A_2 t_2 a_1}. \quad (22)$$

The third method is the zero-stress method, which seeks to achieve zero average in-plane stress for the paired compressive and tensile layers because this condition gives the lowest energy state [43]. Using classical elastic theory for cubic structures

$$A_1 t_1 \epsilon_1 a_2 + A_2 t_2 \epsilon_2 a_1 = 0, \quad (23)$$

$$a_o = \frac{A_1 t_1 a_1 a_2^2 + A_2 t_2 a_2 a_1^2}{A_1 t_1 a_2^2 + A_2 t_2 a_1^2}. \quad (24)$$

The thickness-weighted and zero-stress methods differ simply by the factor $\frac{a_1}{a_2}$ due to the definition of strain using either the substrate (then technically defined as misfit instead of strain) or the average lattice constant in Eq. 9 in the denominator [43]. If both methods use the same strain definition, the results are equivalent.

As a first example, consider 100 Å of InAs and 100 Å of $InAs_{1-x}Sb_x$ as the two layers on a GaSb substrate. The Sb composition is calculated using the three methods above and the results are shown in Table 3 for 0 K. The thickness-weighted model accounting for the elastic constant differences is the closest to the zero-stress model, as expected. It is apparent that taking the differing elastic constants into account makes the composition increase from 15.2 to 15.5 percent. This small disparity is difficult to distinguish during the practical growth of the device. For a second example, consider an $InAs_{1-x}Sb_x$ layer with x = 0.30 on a GaSb substrate at its critical thickness of 32.2 nm. The strain-balanced InAs thickness is found using the different methods with the results shown in Table 3.

Again, the zero-stress model and thickness-weighted model with elastic constants agree within ~2 nm, whereas the other two models are within ~7 and 9 nm. In example 3, the thickness of the $InAs_{1-x}Sb_x$ layer with x = 0.30 is reduced to 2 nm to significantly decrease the SL period, and the strain-balanced InAs thicknesses are calculated and shown in the table. These SL structures with 50 periods were simulated using the Philips X'pert Epitaxy software program to see how the different methods affect the expected XRD patterns. Figure 3 shows that while none of the methods result in a SL zero-order (SL0) peak overlapping with the substrate peak, the zero-stress method SL0 peak is the closest to the substrate peak. Due to the Poisson ratios of InAs (0.352) and InSb (0.353) being very similar, the differences between the four methods, as shown in Table 3 and Figure 3, are practically insignificant. Nonetheless, the SLs in this work are strain balanced using the zero-stress method.

Table 3. Example calculations using the different strain-balancing methods.

Method		Average-lattice	Thickness-weighted	Thickness-weighted with elastic constants	Zero-stress
Example 1	x_{Sb} (%)	15.12	15.20	15.50	15.41
Example 2	t_{InAs} (nm)	95.7	93.8	86.9	88.7
Example 3	t_{InAsSb} (nm) = 2, t_{InAs} (nm)	5.9	5.8	5.4	5.5

2.3 $InAs/InAs_{1-x}Sb_x$ band alignment

The valence band offset between InAs and $InAs_{1-x}Sb_x$ is a critical parameter necessary to predict the SL bandgap because it, along with the bandgaps, determines how the valence and conduction bands align in energy. The band alignment of InAs and $InAs_{1-x}Sb_x$ has been debated for years between type-I,

type-IIa (electron well in the $InAs_{1-x}Sb_x$ (alloy) layer), and type-IIb (electron well in the InAs (binary) layer). Figure 4a schematically shows these different

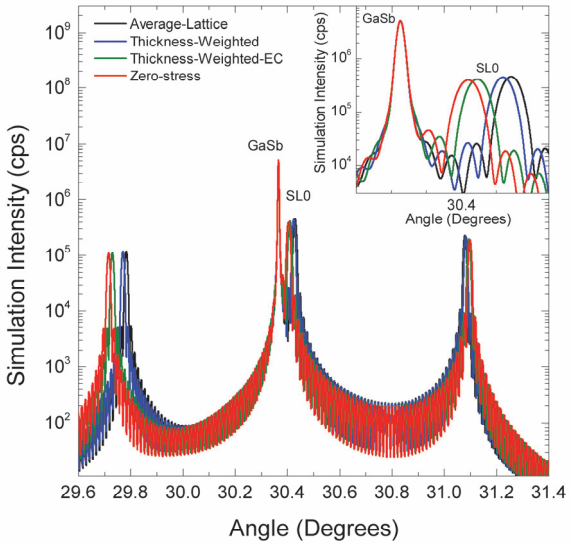

Figure 3. Simulated X-ray diffraction (004) rocking curves for an InAs/(2 nm) $InAs_{0.70}Sb_{0.30}$ SL with the InAs layer thicknesses calculated with the different strain-balancing methods.

alignments and the magnitude range and sign of the fractional band offsets defined as [57]

$$Q_c = \frac{\Delta E_c}{\Delta E_g} = \frac{E_{c\_InAs} - E_{c\_InAsSb}}{E_{g\_InAs} - E_{g\_InAsSb}}, \tag{25}$$

$$Q_v = \frac{\Delta E_v}{\Delta E_g} = \frac{E_{v\_InAsSb} - E_{v\_InAs}}{E_{g\_InAs} - E_{g\_InAsSb}}, \tag{26}$$

$$Q_c + Q_v = 1. \tag{27}$$

When the $InAs_{0.40}Sb_{0.60}/InAs_{1-x}Sb_x$ SLs were first proposed in 1984 [6], the conduction band offset was not known for InAs/InSb, and estimates from various methods differed by 0.3 eV [6]. In 1995, Wei and Zunger did a comprehensive review and a theoretical study of the band alignment of InAs, InSb, and $InAs_{1-x}Sb_x$ using a first principles band structure calculation method paralleling core

photoemission measurements [47]. At that time, the type-II alignment of $InAs_{1-x}Sb_x$/InSb was well accepted but the alignment of InAs/$InAs_{1-x}Sb_x$ was debated

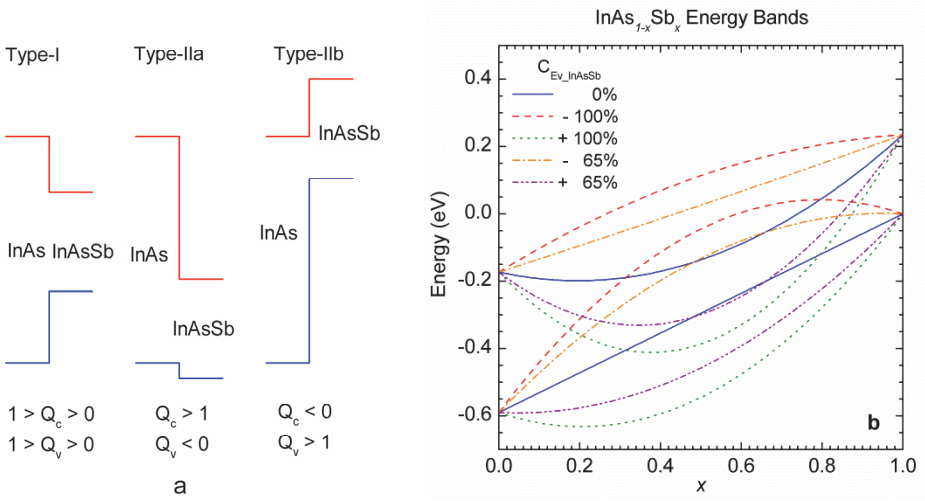

Figure 4. a) Three possible band alignments between InAs and $InAs_{1-x}Sb_x$. b) $InAs_{1-x}Sb_x$ conduction and valence bands calculated at 0 K with an InAs/InSb valence band offset of 0.59 eV, C_{Eg_InAsSb} of 0.67 eV, and different scenarios for the $InAs_{1-x}Sb_x$ bandgap bowing distribution between the conduction and valence bands, which can result in different band edge alignments of InAs-$InAs_{1-x}Sb_x$ heterojunctions.

due to the large bowing of the $InAs_{1-x}Sb_x$ bandgap. The $InAs_{1-x}Sb_x$ bandgap is given by [45]

$$E_{g\_InAsSb} = (1-x)E_{g\_InAs} + xE_{g\_InSb} - x(1-x)C_{Eg\_InAsSb}, \qquad (28)$$

where C_{Eg_InAsSb} is the bandgap bowing factor. The $InAs_{1-x}Sb_x$ valence band edge can be written as

$$E_{v\_InAsSb} = (1-x)E_{v\_InAs} + xE_{v\_InSb} - x(1-x)C_{Ev\_InAsSb}, \qquad (29)$$

which includes the fraction of the bandgap bowing that is attributed to the valence band, C_{Ev_InAsSb}. Figure 4b shows possible scenarios for the $InAs_{1-x}Sb_x$ band edges as a function of x and C_{Ev_InAsSb}. It is evident that the sign and magnitude of C_{Ev_InAsSb} can result in different band edge alignments of InAs/$InAs_{1-x}Sb_x$ heterojunctions at particular x values.

Various experimental results have indicated three different band edge alignments: i) type-I based on magneto-photoluminescence (PL) measurements of metalorganic chemical vapor deposition (MOCVD)-grown strained $InAs/InAs_{0.91}Sb_{0.09}$ multiple quantum wells on InAs substrates with varying well thicknesses [46]; ii) type-IIa from PL and magneto-transmission measurements on molecular beam epitaxy (MBE)-grown $InAs/InAs_{1-x}Sb_x$ SLs on GaAs substrates with InAsSb buffer layers [32, 49]; and iii) type-IIb from PL measurements on As-rich $InAs/InAs_{1-x}Sb_x$ SLs on InAs substrates with conventional [49] and modulated-MBE-grown alloys [18, 31, 58, 59].

2.3.1 Type-I alignment

The type-I alignment was reported for samples with low Sb compositions and ordering present in the $InAs_{1-x}Sb_x$ layer [46], which resulted in a lower alloy bandgap than that of a random alloy with the same composition *x*. With an 8x8 **k.p** Hamiltonian and a transfer matrix technique, Kurtz and Biefeld [46] calculated the energy levels in the $InAs/InAs_{0.91}Sb_{0.09}$ multiple quantum wells with varying thicknesses and used the InAsSb bandgap and the conduction band offset as fitting parameters to compare the results with the experimental data. They claimed that a type-I alignment was the best fit to their data, while a type-II alignment would have resulted in negligible quantum size shifts given the 500 Å InAs barriers used. Compositional ordering and phase separation, as revealed by electron diffraction, in the low temperature grown As-rich InAsSb contributed to the bandgap reduction and the type-I alignment [46]. Wei and Zunger's calculated results agreed that the type-I alignment was possible for low Sb

compositions when ordering is present due to the small type-IIb conduction band offset [47]. However, without ordering and in the presence of strain, Wei and Zunger's calculated band edge alignment is type-IIb [47].

2.3.2 Type-IIa alignment

The type-IIa alignment is supported by contradictory results for the reduced mass values of the lowest two transitions obtained from PL and magneto-transmission measurement results [32, 49]. The PL for an InAs/$InAs_{0.68}Sb_{0.32}$ SL sample grown on a 1μm $InAs_{0.84}Sb_{0.16}$ buffer layer on a GaAs substrate had a peak at 142 meV, while the magneto-transmission showed an absorption feature lower than the PL peak at 115 meV [49]. The authors stated the 115 meV feature was not due to an impurity transition because the absorption was too strong for an impurity. The reduced mass,

$$\frac{1}{m_r^*} = \frac{1}{m_e^*} + \frac{1}{m_h^*} \tag{30}$$

from the magneto-transmission data was larger for the 115 meV transition than the 142 meV transition, so the lower energy transition was attributed to the light hole due to the heavy hole becoming lighter in a strained quantum well [49]. Assuming the $InAs_{0.84}Sb_{0.16}$ buffer layer was completely relaxed, resulting in the InAs layer being tensile strained and the $InAs_{1-x}Sb_x$ layer being compressively strained, the electron well was assigned to the $InAs_{1-x}Sb_x$ alloy layer since the light-hole level in tensile InAs is higher in energy than the heavy-hole level [49].

Another magneto-PL study on InAs/$InAs_{0.865}Sb_{0.135}$ multiple quantum wells [48] with varying $InAs_{0.865}Sb_{0.135}$ thicknesses on InAs substrates found the

lowest energy transition (262 meV) to have a smaller reduced mass than the higher energy transition (291 meV), contradictory to the previous result for SLs grown on $InAs_{1-x}Sb_x$ buffers on GaAs substrates [49]. The PL peak separation of 30 meV was thought to be too large to be attributed to hole confinement or thermal population given the constant 47.5 nm InAs barrier layers, and therefore, the type-IIb alignment was ruled out. After including valence band mixing in a full 8x8 **k.p** band structure calculation to be able to calculate in-plane hole masses, a type-IIa alignment best fit the data [48] and previous data [46] without considering any ordering-induced bandgap reduction, which did not occur in the MBE samples [48]. Using the 8x8 **k.p** band structure calculation, Li *et al.* fit the experimental transitions from magneto-transmission measurements to their calculated absorption curves using the conduction band offset as a fitting parameter [57]. They could fit the lowest energy transition with both types of type-II alignments, but the type-IIa better fit some higher energy transitions [57]. A type-IIa fractional conduction band offset ($Q_c = \Delta E_c/\Delta E_g$) of 2.06 ± 0.11 was determined from the fit. In order to fit a type-I transition, 50 – 190 meV of $InAs_{1-x}Sb_x$ bandgap reduction was necessary, which is unrealistic from ordering, so again the type-IIa alignment was confirmed [57]. A very similar type-IIa result with $Q_c = 2.3$ was obtained for InAs/$InAs_{1-x}Sb_x$, $InAs_{1-x}Sb_x$/$InAs_{0.945}P_{0.055}$, and $InAs_{1-x}Sb_x$/InAsSbP multiple quantum wells grown by MOVPE on InAs substrates [60].

The PL peak energies for four InAs/$InAs_{1-x}Sb_x$ SLs with $x = 0.14 – 0.39$ were less than either of the individual layers' bandgaps, indicating a large type-II

alignment [32, 61]. A Kronig-Penney model including strain and non-parabolicity effects with only the valence band offset as a fitting parameter best fit the data using a type-IIa offset. The valence band offset fits for the four samples had a smaller standard deviation assuming the electron wells were in the $InAs_{1-x}Sb_x$ layer rather than in the InAs layer. These reasons coupled with the magneto-transmission result led the authors to conclude a type-IIa offset occurs [32].

A lower reduced mass for the lowest energy transition [48] suggests a type-IIb alignment, but the type-IIa was chosen as a better fit to the data. When the lowest energy transitions could be fit with type-IIa or type-IIb, type-IIa was chosen based on higher lying transitions. It was stated that apart from interface defects interfering with the band alignment, a large bowing of the $InAs_{1-x}Sb_x$ valence band is necessary for the $InAs/InAs_{1-x}Sb_x$ type-IIb alignment to be compatible with the accepted type-II $InAs_{1-x}Sb_x/InSb$ alignment [49]. The valence band bowing was consequently investigated with recent studies using the type-IIb alignment indicating large bowing of the $InAs_{1-x}Sb_x$ valence band: 60 – 70% of the bandgap bowing [22, 50, 51].

2.3.3 Type-IIb alignment

The third band alignment option, type-IIb, was chosen for $InAs/InAs_{0.93}Sb_{0.07}$ superlattices on InAs substrates [58]. An envelope function approximation was used with the Kronig-Penney model and accepted material parameters to predict the bandgap of the SLs for a laser diode active region. A valence band offset of 610 meV gave predictions that were slightly higher than

the experimental results, indicating the valence band offset may be even larger [58].

Wei and Zunger concluded the InAs/InSb offset is type-II with and without strain with the conduction band of InAs below the valence band of InSb, and the valence band offset was calculated to be 500 meV from first principles [47]. The Sb-rich $InAs_{1-x}Sb_x$/InSb unstrained alignment is also type-II with strain effects and CuPt ordering enhancing the type-II alignment. For the As-rich InAs/$InAs_{1-x}Sb_x$ alignment, CuPt ordering pushes the alignment towards type-I, while strain effects further a type-II alignment, but the top of the valence band is always in the $InAs_{1-x}Sb_x$ layer. They calculated the unstrained alignment to be type-I for InAs/$InAs_{0.9}Sb_{0.1}$ using the InAs/InSb band offsets ΔE_v = 500 meV and ΔE_c = 320 meV and all the bandgap bowing in the conduction band. When InAs/$InAs_{0.9}Sb_{0.1}$ is strained on InAs, however, it is type-IIb. They disagreed with the type-IIa alignment based on Van de Walle's [62], Qteish and Needs'[63], and their own calculations supporting the opposite conclusion, type-IIb, and thus were doubtful of the method of obtaining band offsets from a few emission lines even if the calculated fit is very good [47]. They predict a type-I alignment for unstrained As-rich InAs/$InAs_{1-x}Sb_x$ with $x < 0.5$ and type-II for the strained case on InAs, noting the small conduction band offset makes the alignment susceptible to convert to type-I even in the strained situation if ordering is present in the $InAs_{1-x}Sb_x$.

Wei and Zunger's conclusions were based on all the bandgap bowing occurring in the conduction band with the valence band varying linearly with *x*

[47], as shown in Figure 4b. PL data from InAs/$InAs_{1-x}Sb_x$ multiple quantum wells with x = 0.065 – 0.137 on InAs substrates was fit with the type-IIb alignment and 60% bowing in the valence band [50]. The samples could have had Sb segregation while the InAs layer was grown, but the authors stated that would result in increasing the valence band bowing [50]. A similar result of 65% bowing in the valence band was reported for $InAs_{1-x}Sb_x/InAs_{0.67}P_{0.23}Sb_{0.10}$ quantum wells with x = 0.05 – 0.13 using Wei and Zunger's 0.5 eV valence band offset between InAs and InSb. A valence-band anti-crossing model was used to explain the valence band bowing, and these results for the As-rich region were noted as contrary to the widely accepted expectation that III-V materials contain the majority of the bowing in the conduction band. Lackner *et al*. also used Wei and Zunger's type-IIb alignment citing that the electron well being in the $InAs_{1-x}Sb_x$ layer is not consistent with the lower electron affinity of InSb compared to InAs and arrived at 60 – 70 % bandgap bowing in the valence band for their InAs/$InAs_{1-x}Sb_x$ multiple quantum wells with varying x = 0.138 – 0.267 on GaSb substrates [22]. The differing results for the band alignments and offsets are summarized in APPENDIX B B. The initial calculations presented in this work are based on the type-IIb alignment with 65 % of the $InAs_{1-x}Sb_x$ bandgap bowing attributed to the valence band and an InAs/InSb valence band offset of 0.59 eV [45]. Further investigation into the InAs/$InAs_{1-x}Sb_x$ valence band offsets and $InAs_{1-x}Sb_x$ valence band bowing is discussed in Chapter 5.

2.4 Material parameters

The calculated SL bandgap results are highly dependent upon the material parameters entered into the model. The valence band offset has been reviewed in the previous section. In this section, the $InAs_{1-x}Sb_x$ bandgap is reviewed and the other material parameters are summarized.

2.4.1 $InAs_{1-x}Sb_x$ bandgap

The bandgap of $InAs_{1-x}Sb_x$ versus x at different temperatures has been experimentally measured by several investigators. The optical properties of polycrystalline $InAs_{1-x}Sb_x$ were first investigated by Woolley and Warner for $0 < x < 0.2$ and $0.55 < x < 1$, but they could not measure $InAs_{1-x}Sb_x$ with $0.2 < x < 0.55$ due to a miscibility gap in which the alloys do not form homogeneously when grown under equilibrium conditions [64]. Stringfellow and Greene investigated $InAs_{1-x}Sb_x$ grown by liquid phase epitaxy (LPE) on InAs substrates for $0 < x < 0.35$ and on InSb substrates for $0.89 < x < 1$, and their result for the band gap at 300 K agreed well with Woolley and Warner's data [65].

Because MBE and MOCVD are non-equilibrium growth methods, single crystal $InAs_{1-x}Sb_x$ can be grown within the miscibility gap. The first systematic study of $InAs_{1-x}Sb_x$ on InAs substrates grown by MBE was done by Yen, *et al.* and found $InAs_{1-x}Sb_x$ the most difficult to grow for $0.3 < x < 0.8$ [65]. The As incorporation into the thin film depended on the In and Sb fluxes, and for a sample with $x = 0.68$, they obtained a 12.5 μm cutoff wavelength at 300 K. Fang. *et al.* reported a small shift in the PL peak energy location with temperature for $InAs_{1-x}Sb_x$ samples on InAs substrates with $x < 0.3$ grown by OMVPE [66]. They

used wave-vector-nonconserving transitions to explain the small change in the peak energy location with temperature [66]. The FWHM were comparable to Yen, *et al.*'s MBE grown samples, indicating similar sample quality.

The various expressions for the $InAs_{1-x}Sb_x$ bandgap are summarized in Table 4 and the bandgap for $InAs_{0.6}Sb_{0.4}$ using the different equations is given in Table 5. At 300 K, Wieder [67] and Yen's [65] expressions agree but are 16 meV higher than Vurgaftman's [45] (see Figure 5a). At low temperatures (0 – 10 K), the spread in $InAs_{0.6}Sb_{0.4}$ bandgap values is 17 meV (Figure 5c). The most recent data for the $InAs_{1-x}Sb_x$ bandgap from Belenky *et al*. gives significantly lower values, 30 meV, than the previous expressions at 77 K, as shown in Figure 5b.

2.4.2 Material parameter summary

The majority of the InAs, InSb, and $InAs_{1-x}Sb_x$ parameters were taken from a comprehensive review paper with consistent sets of parameters for III-V materials [45], with the actual parameters used in the calculations listed in Appendix C. However, for comparison, effective mass values from two sources are given, but the calculations use the values from Ref. [45]. Also, for consistency, the $InAs_{1-x}Sb_x$ bandgap used is from Ref. [45].

2.5 Band structure models

The SL bandgap is determined by the energy band structure, and models of varying complexity, such as the Kronig-Penney, envelope function approximation, multiband $\mathbf{k}\cdot\mathbf{p}$, and tight-binding models, are used to determine the band structure. Near the band edges, at $k = 0$ (Γ point), of direct bandgap

Table 4. Different equations for the $InAs_{1-x}Sb_x$ bandgap.

$InAs_{1-x}Sb_x$ Bandgap [eV]	Temp [K]	Longest λ_g [μm]	x	Reference
$E_g = 0.354(1-x) + 0.174x - x(1-x)0.67$	300	14.7	0.634	[45]
$E_g = 0.417(1-x) + 0.235x - x(1-x)0.67$	0	8.5	0.636	[45]
$E_g = 0.235 - \frac{3.4x10^{-4}T^2}{210+T} - (0.524 - 3.4x10^{-4}T)(1-x) + (0.7 - 3.4x10^{-4}T)(1-x)^2$	300	12.3	0.647	[67]
$E_g = 0.235 - \frac{3.4x10^{-4}T^2}{210+T} - (0.524 - 3.4x10^{-4}T)(1-x) + (0.7 - 3.4x10^{-4}T)(1-x)^2$	0	9.1	0.626	[67]
$E_g = 0.4324 - 0.8831x + 0.6853x^2$	10	8.4	0.644	[68]
$E_g = 0.415(1-x) + 0.235x - x(1-x)0.672$	10	8.5	0.634	[66]
$E_g = 0.35 - 0.771x + 0.596x^2$	300	12.3	0.647	[65]
$E_g = 0.418 - 0.903x + 0.722x^2$	4	9.1	0.625	[56A, 69]
$E_g = 0.418 - 0.851x + 0.671x^2$ better fit to interband data in bulk	4	8.4	0.634	[56B]
$E_g = 0.228x^2 - 0.0363x(1-x) + 0.404(1-x)^2$	77	9.0	0.632	[6]
$E_g = 0.404(1-x) + 0.232x - x(1-x)0.8$	77	11.4	0.607	[38]

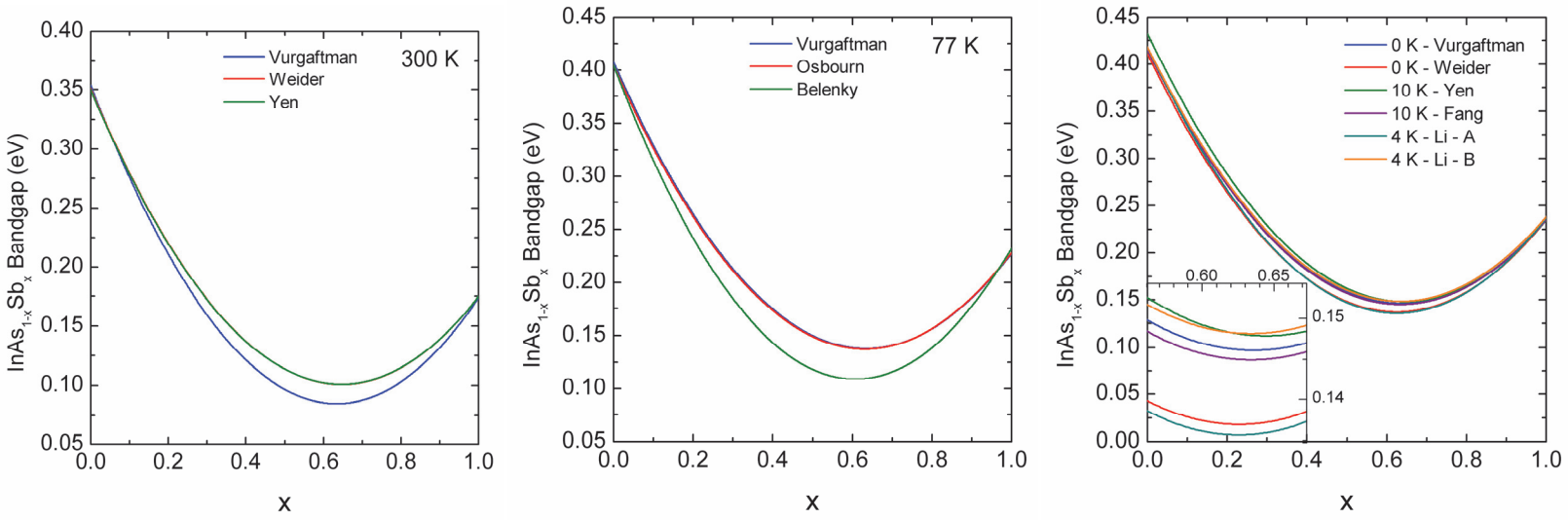

(a) (b) (c)

Figure 5. The bandgap of $InAs_{1-x}Sb_x$ versus composition at (a) 300 K, (b) 77 K, and (c) 0 – 10 K for varying expressions.

Table 5. Comparison of the $InAs_{0.6}Sb_{0.4}$ bandgap from different models.

$InAs_{0.6}Sb_{0.4}$ Bandgap [meV]								
Temp (K)	[45]	[6]	[67]	[68]	[65]	[57]A	[57]B	[38]
300	121		137		137			
77	175	173						143
10				189				
4						172	185	
0	183		173					

semiconductors, the approximation of parabolic energy bands is valid and often used to simplify the calculations. The *E-k* dispersion in this case is given as

$$E(\boldsymbol{k}) = \frac{\hbar^2 \boldsymbol{k}^2}{2m^*} \tag{31}$$

where $\hbar$ is Plank's constant divided by 2π, m^* is the electron effective mass in the semiconductor crystal, and k is the electron wave vector. The electron wave function in the periodic crystal experiencing a periodic potential,

$$V(\boldsymbol{r}) = V(\boldsymbol{r} + \boldsymbol{R}), \tag{32}$$

is written as the Bloch function, $\psi_{n\boldsymbol{k}}(\boldsymbol{r})$,

$$\psi_{n\boldsymbol{k}}(\boldsymbol{r}) = e^{i\boldsymbol{k}\cdot\boldsymbol{r}} u_{n\boldsymbol{k}}(\boldsymbol{r}), \tag{33}$$

$$u_{n\boldsymbol{k}}(\boldsymbol{r} + \boldsymbol{R}) = u_{n\boldsymbol{k}}(\boldsymbol{r}), \tag{34}$$

where $u_{n\boldsymbol{k}}(\boldsymbol{r})$ is a periodic function due to the periodic crystal lattice with lattice vector $\boldsymbol{R}$ and n is an integer denoting the band [56]. The Bloch functions are solutions to the Schrödinger equation with Hamiltonian, H, and free electron mass, m_o,

$$H\Psi(\boldsymbol{r}) = \left[-\frac{\hbar^2}{2m_o}\nabla^2 + V(\boldsymbol{r})\right]\Psi(\boldsymbol{r}) = E_n(\boldsymbol{k})\Psi(\boldsymbol{r}). \tag{35}$$

2.5.1 ***k.p*** model

The ***k.p*** model uses perturbation theory to analyze the band structure around a certain k value, typically at $k = 0$, taking into account the interaction of various bands. Putting the wave function in Eq. (33) into the Schrödinger in Eq. (35), we have for a single band [56]

$$H\psi_{n\boldsymbol{k}}(\boldsymbol{r}) = \left[\frac{p^2}{2m_o} + V(\boldsymbol{r})\right]\psi_{n\boldsymbol{k}}(\boldsymbol{r}) = E_n(\boldsymbol{k})\psi_{n\boldsymbol{k}}(\boldsymbol{r}), \quad (36)$$

which becomes

$$\left[\frac{p^2}{2m_o} + \frac{\hbar}{m_o}\boldsymbol{k}\cdot\boldsymbol{p} + V(\boldsymbol{r})\right]u_{n\boldsymbol{k}}(\boldsymbol{r}) = \left[E_n(\boldsymbol{k}) - \frac{\hbar^2k^2}{2m_o}\right]u_{n\boldsymbol{k}}(\boldsymbol{r}), \quad (37)$$

when putting it in terms of $u_{n\boldsymbol{k}}(\boldsymbol{r})$. It is evident from Eq. (37) why this method is called ***k.p***. Second-order perturbation results in energy bands versus *k* given by [56]

$$E_n(\boldsymbol{k}) = E_n(0) + \frac{\hbar^2k^2}{2m_o} + \frac{\hbar}{m_o}\boldsymbol{k}\cdot\boldsymbol{p}_{nn} + \frac{\hbar^2}{m_o^2}\sum_{n'\neq n}\frac{|\boldsymbol{k}\cdot\boldsymbol{p}_{nn'}|^2}{E_n(0) - E_{n'}(0)}, \quad (38)$$

where the last term on the right hand side of the equation accounts for the interaction between the band *n* and the other bands *n'*. For the case of $k = 0$ with α and $\beta = x, y,$ or z,

$$E_n(\boldsymbol{k}) = E_n(0) + \frac{\hbar^2}{2}\sum_{\alpha,\beta}\left(\frac{1}{m^*}\right)_{\alpha,\beta}k_\alpha k_\beta. \quad (39)$$

These equations can be expanded to matrix equations to include multiple bands that are non-degenerate or degenerate. The more bands that are included, the more accurate the band structure becomes. See Ref [56] for more detail.

2.5.2 Envelope function approximation

The envelope function approximation allows determination of the band structure of layered heterostructures, such as quantum wells and SLs, using the constituent bulk parameters and band offsets and a slowly varying over the unit cell dimension perturbation potential. The magnitude of the perturbing potential is assumed to be small such that there is no mixing between the bands. The

periodic atomic potential, $V(\boldsymbol{r})$, determines the energy bands and effective masses (effective mass approximation), and the perturbation potential only modifies the Hamiltonian,

$$[H_0 + U(\boldsymbol{r})]\psi(\boldsymbol{r}) = E\psi(\boldsymbol{r}), \tag{40}$$

resulting in the wave function being approximated with the envelope function, $F(\boldsymbol{r})$, and the periodic part of the Bloch function,

$$\psi(\boldsymbol{r}) = F(\boldsymbol{r})u_{n\boldsymbol{k_0}}(\boldsymbol{r}). \tag{41}$$

2.5.3 Three-band model

The three-band model used in this work arises from an 8 x 8 band (electron, heavy hole, light hole, and spin-orbit hole with spin degeneracy) envelope function approximation Hamiltonian considered at the center of the two-dimensional Brillouin zone [44, 70, 71]. In this case, the Hamiltonian decouples into two equal 1 x 1 Hamiltonians for the heavy hole and two equal 3 x 3 Hamiltonians for the coupled electron, light hole, and spin-orbit hole. The Schrödinger equation for the heavy hole is given by [44]

$$\left[-\frac{\hbar^2}{2}\frac{d}{dz}\frac{1}{m_{HH}(z)}\frac{d}{dz} + V_{HH}(z)\right]F_{HH}(z) = EF_{HH}(z), \tag{42}$$

where m_{HH} is the heavy hole mass, V_{HH} is the valence band edge, and F_{HH} is the envelope function. The Schrödinger equation for the coupled electron, light hole, and spin-orbit hole can be simplified to

$$\left[-\frac{\hbar^2}{2}\frac{d}{dz}\frac{1}{m_C(z)}\frac{d}{dz} + V_C(z)\right]F_C(z) = EF_C(z), \tag{43}$$

where m_C is the effective coupled mass, V_C is the conduction band edge, and F_C is the envelope function. m_C can be written as [44]

$$m_C(z) = \frac{3\left[\frac{\Delta E^2}{2} - (V_{LH}(z) - E)(V_{SO}(z) - E)\right]}{2\Pi^2[2(V_{SO}(z) - \Delta E - E) + V_{LH}(z) - E]}, \tag{44}$$

$$\Delta E = 2b(\varepsilon_\perp - \varepsilon_\parallel), \tag{45}$$

$$\Pi = \frac{-i\langle s|p_x|x\rangle}{m_o}, \tag{46}$$

with V_{LH} the light-hole band edge, V_{SO} the spin-orbit-hole band edge, b a deformation potential, and $\varepsilon_\perp$ and $\varepsilon_\parallel$ the perpendicular and parallel strains. The envelope function solutions for materials A and B of a SL are of the following form for the case of flat-band potentials

$$F^A(z) = C_1 e^{ik_A z} + C_2 e^{-ik_A z}, \tag{47}$$

$$F^B(z) = C_3 e^{ik_B z} + C_4 e^{-ik_B z}, \tag{48}$$

with wave vectors given as

$$k_{A,B} = \sqrt{\frac{2m_{HH}^{A,B}}{\hbar^2}(V_{HH}(z) - E)} \quad for\ heavy\ holes, and \tag{49}$$

$$k_{A,B} = \sqrt{\frac{2m_C^{A,B}}{\hbar^2}\left(E - V_C(z)\right)} \quad for\ the\ coupled\ electron\ and\ holes. \tag{50}$$

The continuity of the envelope functions and their derivatives at the material boundaries result in Eq. (51), with L_A and L_B being the widths of layers A and B, $d = L_A + L_B$ being the SL period, and q being the SL wave vector in the growth direction.

$$\cos(qd) = \cos(k_A L_A)\cosh(k_B L_B) - \frac{1}{2}\left(\eta + \frac{1}{\eta}\right)\sin(k_A L_A)\sinh(k_B L_B), \tag{51}$$

$$\eta = \frac{k_A M_{HH}^B}{k_B M_{HH}^A} \quad for\ heavy\ holes, and \tag{52}$$

$$\eta = \frac{k_A M_C^B}{k_B M_C^A} \quad for\ electrons\ and\ coupled\ holes. \tag{53}$$

These results have the same mathematical form as the Kronig-Penney model, but unlike the Kronig-Penney model, the three-band model includes coupling between the electron, light-hole, and spin-orbit hole.

2.5.4 Kronig-Penney model

The Kronig-Penney model for a SL uses the propagation matrix approach to solve for the energy levels and wave functions of a periodic one-dimensional potential, as shown in Figure 6. This model assumes parabolic energy bands and thus is only valid near at $k = 0$. The electron, heavy-hole, and light-hole energy levels are solved for separately with the respective potential profile. This makes the Kronig-Penney the simplest of the band structure models reviewed here since interaction between the electron and hole bands is not considered.

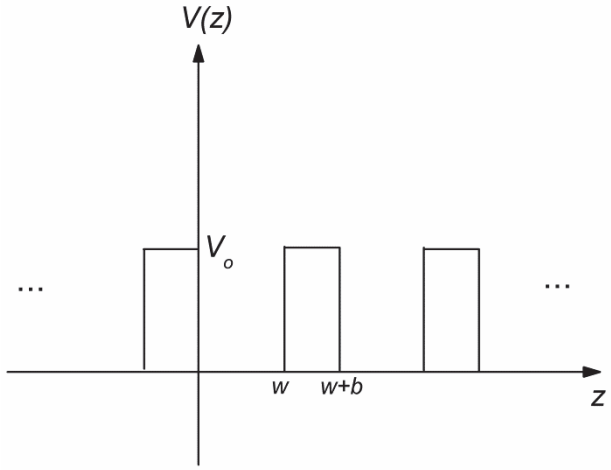

Figure 6. Schematic of the periodic potential for the Kronig-Penney model.

The wave vectors in the well and barrier regions are [56]

$$k = \sqrt{\frac{2m}{\hbar^2}E} \qquad for\ the\ well, and \tag{54}$$

$$k_b = \sqrt{\frac{2m_b}{\hbar^2}(E - V_o)} \quad for\ the\ barrier. \tag{55}$$

The wave function for one period is

$$\psi(z) = \begin{cases} Ae^{ikz} + Be^{-ikz}, & 0 \le z \le w \\ Ce^{ik_b(z-b)} + De^{-ik_b(z-b)}, & w \le z \le w + b \end{cases} \tag{56}$$

and the continuity of the wave functions and their derivatives at the well and barrier boundaries result in the following equations describing the SL energy minibands, with wave vector q in the z-direction [56]

$$f(E) = \cos(qL)\ where\ L = b + w\ and$$

$$f(E) = \begin{cases} \cos(kw)\cosh(\alpha_b b) + \frac{1}{2}\left(\eta - \frac{1}{\eta}\right)\sin(kw)\sinh(\alpha_b b)\,, 0 < E < V_o \\ \cos(kw)\cos(k_b b) - \frac{1}{2}\left(P + \frac{1}{P}\right)\sin(kw)\sin(k_b b)\,, V_o < E \end{cases} \tag{57}$$

$$\alpha_b = \sqrt{\frac{2m_b}{\hbar^2}(V_o - E)}, \tag{58}$$

$$P = \frac{mk_b}{m_b k} = i\eta. \tag{59}$$

Despite the simplicity of the Kronig-Penney model, it can be quite useful for predicting the SL bandgap at $k = 0$ when the appropriate material parameters are used to setup the model.

The SL miniband effective mass can be approximated from the dispersion relation obtained with the Kronig-Penney model as follows. The effective mass is defined as

$$m^* = \frac{\hbar^2}{\frac{d^2E}{dq^2}}, \tag{60}$$

and expanding Eq. (57) around energy level E_i using a Taylor series[72, 73],

$$F(E) = F(E_i) + \frac{dF(E)}{dE}|_{E=E_i}(E - E_i), and \tag{61}$$

$$\cos(qL) = F(E_i) + \frac{dF(E)}{dE}|_{E=E_i}(E - E_i). \tag{62}$$

Rearranging to solve for E,

$$E = E_i + \frac{cos(qL)}{\frac{dF(E)}{dE}|_{E=E_i}} - \frac{F(E_i)}{\frac{dF(E)}{dE}|_{E=E_i}}, \tag{63}$$

and defining s and t as

$$s = -\frac{F(E_i)}{\frac{dF(E)}{dE}|_{E=E_i}}, \tag{64}$$

$$t = \frac{1}{2\frac{dF(E)}{dE}|_{E=E_i}}. \tag{65}$$

allows the energy in Eq. (73) and its second derivative to be written as

$$E = E_i + s + 2t\cos(qL), \tag{66}$$

$$\frac{d^2E}{dq^2} = -2tL^2\cos(qL). \tag{67}$$

The effective mass is now approximated as [73]

$$|m^*| = \frac{\hbar^2}{2|t|L^2\,cos(qL)}, and \tag{68}$$

$$|m^*| = \frac{\hbar^2}{2|t|L^2}\ at\ q = 0. \tag{69}$$

2.6 Superlattice absorption

To compare the strength of the SL interband absorption, an electron transition from the valence band to the conduction band, between SL designs, both the SL wave function overlap and density of states must be taken into account. The absorption rate per volume, *V*, is [56]

$$R_{a\to b} = \frac{2}{V}\sum_{k_a}\sum_{k_b}\frac{2\pi}{\hbar}|H'_{ba}|^2\delta(E_a - E_b - \hbar\omega)f_a(1-f_b). \tag{70}$$

The Fermi functions, f_a and f_b, indicate the probability of the initial and final states being occupied by an electron, the delta function conserves energy between the transition and the incident photon and leads to the density of states when summed over all *k*, and H'_{ba} is the interband optical matrix element.

2.6.1 Interband optical matrix element

For bulk semiconductors H'_{ba} is [56]

$$H'_{ba} = -\frac{eA_o}{2m_o}\hat{e}\cdot\int \psi_b^*\, e^{i\boldsymbol{k}_{op}\cdot\boldsymbol{r}}\boldsymbol{p}\psi_a d^3\boldsymbol{r} \approx -\frac{eA_o}{2m_o}\hat{e}\cdot\boldsymbol{p_{cv}}\,\delta_{k_c,k_v}. \tag{71}$$

where A_o is the magnitude and $\hat{e}$ the unit vector of the optical field vector potential, $\boldsymbol{k}_{op}$ is the wave vector of the incident light, $\boldsymbol{p}$ is the momentum operator, δ_{k_c,k_v} represents the conservation of momentum, and the Bloch wave functions are

$$\psi_{a,b}(\boldsymbol{r}) = \frac{e^{i\boldsymbol{k}_{v,c}\cdot\boldsymbol{r}}}{\sqrt{V}} u_{v,c}(\boldsymbol{r}). \tag{72}$$

The interband momentum matrix element $\boldsymbol{p_{cv}}$ only depends on the periodic part of the Bloch functions,

$$p_{cv} = \int u_c^*(\boldsymbol{r}) \frac{\hbar}{i} \nabla u_v(\boldsymbol{r}) \frac{d^3\boldsymbol{r}}{\Omega}. \tag{73}$$

For quantum wells, and similarly SLs, the Bloch wave functions contain an envelope function, $\phi_{n,m}(z)$ for the valence and conduction bands, due to the potential variation in the growth direction, and the wave vector in the plane, k_t, and the area of the plane are now considered instead of the volume [56],

$$\psi_{a,b}(\boldsymbol{r}) = \phi_{n,m}(z) \frac{e^{i\boldsymbol{k_t}\cdot\boldsymbol{\rho}}}{\sqrt{A}} u_{v,c}(\boldsymbol{r}). \tag{74}$$

Putting the superlattice Bloch functions into Eq. (94), results in

$$H'_{ba} \approx -\frac{eA_o}{2m_o} \hat{e} \cdot \boldsymbol{p_{cv}}\, \delta_{k_t,k_t'} I_{hm}^{en}, \tag{75}$$

$$I_{hm}^{en} = \int_0^L \phi_m^*(z)\phi_n(z)dz, \tag{76}$$

where I_{hm}^{en} is the wave function overlap defined over the SL period [56] and $\delta_{k_t,k_t'}$ represents the conservation of momentum in the plane. Equation (75) shows that the interband optical matrix element is proportional to the wave function overlap, so comparing the wave function overlaps of various designs can give an idea of the strength of the interband optical matrix element. However, to determine the strength of the transition rate, the SL density of states must also be taken into account.

2.6.2 Superlattice density of states

The SL density of states per unit energy is usually calculated after the *E*-*k* band structure has been obtained by one of the above methods. The density of states in *k*-space in the growth direction is a constant, (*Nd*)/2π, with *N* being the total number of periods and *d* the SL period. The *E*-*k* dispersion relation, or band structure, is then used to convert the density of states per unit *k* to the density of states per unit energy. The following SL density of states is derived based on the tight-binding model. The tight-binding model considers a series of quantum wells, as shown in Figure 6, and only takes interaction with the nearest neighbor quantum wells into account. The Bloch wave function contains the i^{th} wave function of the quantum well, $\chi_{loc}^{i}(z-nd)$, centered at $z = nd$, where n is the well index, d the SL period, and N the total number of periods [74].

$$\psi_q^i(z) = \frac{1}{\sqrt{N}} \sum_n e^{iqnd} \chi_{loc}^i(z-nd) \tag{77}$$

The SL wave vector q is required by the Born-von Karman periodic boundary conditions to be discrete integer multiples of 2π/(*Nd*). The solution for the SL energy levels in the *z*-direction is given by [73, 74]

$$\mathcal{E}_i(q) = E_i + s_i - 2t_i \cos(qd), \tag{78}$$

$$s_i = \int_{-\infty}^{\infty} {\chi_{loc}^i}^*(z-d) V(z) \chi_{loc}^i(z-d) dz, \tag{79}$$

$$t_i = \int_{-\infty}^{\infty} {\chi_{loc}^i}^*(z) V(z) \chi_{loc}^i(z-d) dz, \tag{80}$$

where s_i is the shift energy of the i^{th} state and t_i is the exchange energy [75]. The width of the SL miniband is given by $4|t_i|$. The total energy including the in-plane energy is

$$\mathcal{E}_i(q, k_\perp) = E_i + s_i - 2|t_i|\cos(qd) + \frac{\hbar^2 k_\perp^2}{2m}. \tag{81}$$

The number of states per unit energy, or density of states, can be found by evaluating

$$\begin{aligned}\rho(\mathcal{E}) &= \sum_{n,q,k_\perp,\sigma_s} \delta\left(\mathcal{E} - \mathcal{E}_i(q) - \frac{\hbar^2 k_\perp^2}{2m}\right) \\ &= \sum_n \sum_q \sum_{k_\perp} \sum_{\sigma_s} \delta\left(\mathcal{E} - \mathcal{E}_i(q) - \frac{\hbar^2 k_\perp^2}{2m}\right).\end{aligned} \tag{82}$$

Summing over the spin states, converting the sum over the continuous in-plane $k_\perp$to an integral in polar coordinates [56], and converting to energy using $k_\perp^2 = \frac{2mE}{\hbar^2}$ and $k_\perp dk_\perp = \frac{m}{\hbar^2} dE$ gives [73]

$$\rho(\mathcal{E}) = \frac{L_x L_y}{\pi} \sum_n \sum_q \int k_\perp dk_\perp \, \delta\left(\mathcal{E} - \mathcal{E}_i(q) - \frac{\hbar^2 k_\perp^2}{2m}\right), \tag{83}$$

$$\rho(\mathcal{E}) = \frac{L_x L_y}{\pi} \frac{m}{\hbar^2} \sum_n \sum_q \int dE \, \delta(\mathcal{E} - \mathcal{E}_i(q) - E), and \tag{84}$$

$$\rho(\mathcal{E}) = \frac{L_x L_y}{\pi} \frac{m}{\hbar^2} \sum_n \sum_q \mathrm{H}(\mathcal{E} - \mathcal{E}_i(q)), \tag{85}$$

where H is the Heaviside step function. Now summing over q using $\Delta q = \frac{2\pi}{Nd}$ and integrating over half the Brillouin zone [73],

$$\rho(\mathcal{E}) = \frac{L_x L_y}{\pi}\frac{m}{\hbar^2}\sum_n \frac{1}{\Delta q}\int \mathrm{dq}\ \mathrm{H}(\mathcal{E} - \mathcal{E}_i(q)) \tag{86}$$

$$\rho(\mathcal{E}) = \frac{L_x L_y N d}{\pi^2}\frac{m}{\hbar^2}\sum_n \int_0^{\frac{\pi}{d}} \mathrm{dq}\ \mathrm{H}(\mathcal{E} - \mathcal{E}_i(q)) = \sum_n \rho_n(\mathcal{E}) \tag{87}$$

$$\rho_n(\mathcal{E}) = \frac{L_x L_y N d}{\pi^2}\frac{m}{\hbar^2}\int_0^{\frac{\pi}{d}} \mathrm{dq}\ \mathrm{H}(\mathcal{E} - \mathcal{E}_i(q)) \tag{88}$$

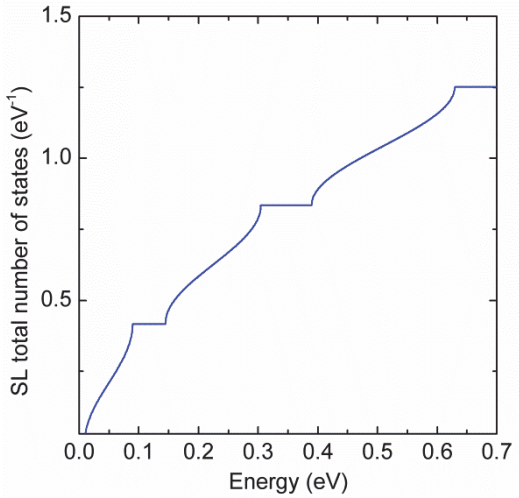

Figure 7. An example calculation of the SL total number of states per unit energy on an arbitrary scale showing the expected shape of the curve.

Evaluating Eq. (88) results in the following equation for the total number of states per energy, which has units 1/eV [72-74],

$$\rho(\mathcal{E}) = \sum_n \begin{cases} L_x L_y N \dfrac{m}{\pi\hbar^2}, & for\ \mathcal{E} - E_i - s_i > 2|t_i| \\ L_x L_y N \dfrac{m}{\pi^2\hbar^2}\cos^{-1}\left(\dfrac{E_i + s_i - \mathcal{E}}{2|t_i|}\right), & for\ |\mathcal{E} - E_i - s_i| < 2|t_i| \\ 0, & for\ for\ \mathcal{E} - E_i - s_i < -2|t_i| \end{cases}. \tag{89}$$

An example of the SL total number of states per unit energy calculated with Eq. (89) is shown in Figure 7. The total number of states per unit energy is proportional to the total number of periods, *N*. The number of states per volume,

or the density of states, however, is not proportional to N but inversely proportional to d, the SL period. Converting Eq. (89) to the density of states (number of states per unit energy per volume) by dividing by the volume, $L_x L_y N d$, gives [75]

$$\rho(\mathcal{E}) = \sum_n \begin{cases} \dfrac{m}{\pi\hbar^2 d}, & for\ \mathcal{E} - E_i - s_i > 2|t_i| \\ \dfrac{m}{\pi^2\hbar^2 d}\cos^{-1}\left(\dfrac{E_i + s_i - \mathcal{E}}{2|t_i|}\right), & for\ |\mathcal{E} - E_i - s_i| < 2|t_i| \\ 0, & for\ \mathcal{E} - E_i - s_i < -2|t_i| \end{cases}, \quad (90)$$

with units $eV^{-1}cm^{-3}$. If the density of states in Eq. (90) is multiplied by the period d, [75]

$$\rho(\mathcal{E}) = \sum_n \begin{cases} \dfrac{m}{\pi\hbar^2}, & for\ \mathcal{E} - E_i - s_i > 2|t_i| \\ \dfrac{m}{\pi^2\hbar^2}\cos^{-1}\left(\dfrac{E_i + s_i - \mathcal{E}}{2|t_i|}\right), & for\ |\mathcal{E} - E_i - s_i| < 2|t_i| \\ 0, & for\ \mathcal{E} - E_i - s_i < -2|t_i| \end{cases}, \quad (91)$$

the 2D quantum well density of states with units $eV^{-1}cm^{-2}$ (number of states per area, $\frac{m}{\pi\hbar^2}$) [56] results for $\mathcal{E} > E_i + s_i + 2|t_i|$. In Figure 7, the step-like portion of the density of states is apparent when $\mathcal{E} > E_i + s_i + 2|t_i|$.

To increase the strength of the interband optical matrix element, the previous section showed the SL wave function overlap should be increased, which is usually accomplished by decreasing the SL layer thicknesses. According to the results of this section, if the SL period is decreased, the density of states will increase under the assumption that the electron mass and the arccosine term remain unchanged. But the $|t_i|$ and s_i terms increase with decreased period, and the effective mass changes with the band structure. Without calculating the full

band structure, the changes in the effective mass and the SL minibands as the layer thicknesses are changed are difficult to predict. The best way to optimize the SL absorption is to calculate it directly starting with Eq. (70) and being aware of the approximations used.

2.7 InAs/$InAs_{1-x}Sb_x$ superlattice three-band model results

Figure 8 displays the calculated SL bandgap in microns versus the layer thicknesses for strain-balanced designs on GaSb containing four different $InAs_{1-x}Sb_x$ compositions. These calculations were done using E_{v_InAs} = -0.59 eV, E_{v_InSb} = 0 eV, C_{Eg_InAsSb} = 0.67 eV, and the InAs/$InAs_{1-x}Sb_x$ unstrained fractional valence band offset, Q_v = 1.03, as discussed in Chapter 5. Within this composition range (x = 0.30 – 0.45), the InAs/$InAs_{1-x}Sb_x$ SL designs are shown to cover the entire MWIR and LWIR ranges. For a given composition, thicker layers result in smaller bandgaps, or longer wavelengths, and the overlap between the electron and heavy-hole wave functions decreases. However, as the absorption coefficient is proportional to the square of the wave function overlap (and the density of states), as discussed in Section Superlattice absorption, larger overlaps are desirable. To optimize the wave function overlap for a particular bandgap, as shown in Figure 9, the layers should be thin with higher Sb compositions in the $InAs_{1-x}Sb_x$ layer. The wave function overlap is inherently lower for the longer wavelength designs due to the higher Sb compositions resulting in larger valence band offsets and increased heavy-hole confinement. In addition, the material growth becomes more challenging as the Sb composition increases due to the competition between arsenic and antimony for incorporation into the film.

Figure 8 reveals a limit to the short period InAs/$InAs_{1-x}Sb_x$ SL bandgap, which is almost independent of the Sb composition. This occurs for short-period SLs within the envelope function approximation model because the SL approaches an $InAs_{1-x}Sb_x$ bulk alloy with an average Sb composition.

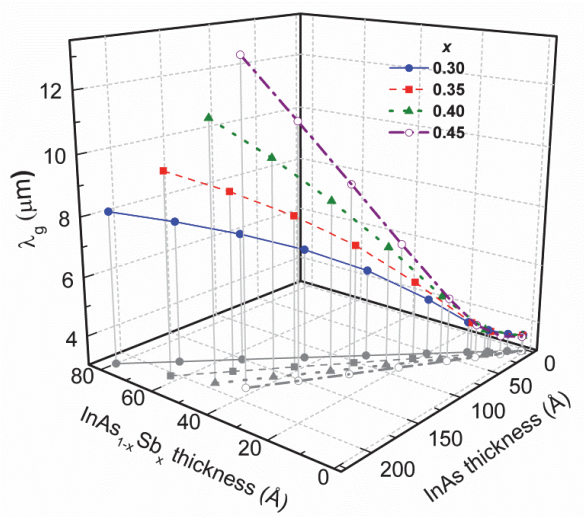

Figure 8. Calculated effective bandgaps, covering the MWIR and LWIR, for strain-balanced type-II InAs/$InAs_{1-x}Sb_x$ superlattices on GaSb substrates for four different $InAs_{1-x}Sb_x$ compositions.

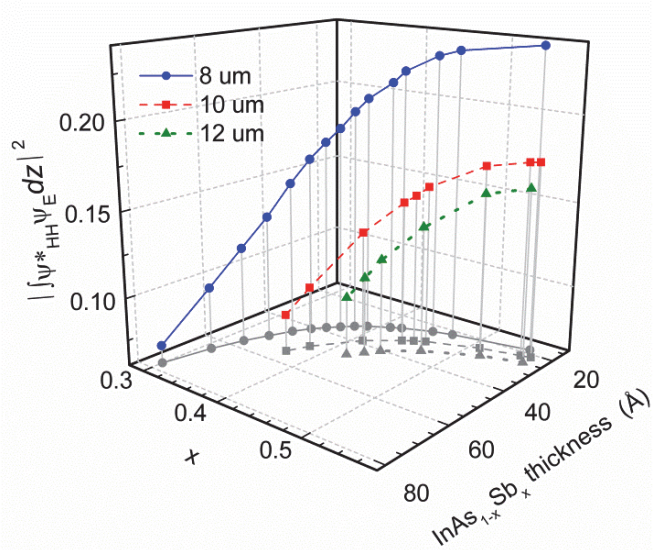

Figure 9. Calculated square of the electron-heavy hole wave function overlap for different strain-balanced type-II InAs/$InAs_{1-x}Sb_x$ superlattices designs having bandgaps equivalent to 8, 10, and 12 μm.

The average Sb composition for the SL is given by

$$\bar{x} = 1 - \frac{L_{InAs} + (1-x)L_{InAsSb}}{L_{InAs} + L_{InAsSb}}. \quad (92)$$

The shortest period designs considered here have a 1 Å thick $InAs_{1-x}Sb_x$ layer and the corresponding strain-balanced thicknesses for the InAs layer range from ~2-5 Å for the different x. The bandgap of the average $InAs_{1-x}Sb_x$ composition calculated for the short period SLs are plotted along with the SL bandgap for comparison in Figure 10a. The two bandgap values differ by less than 1 μm over

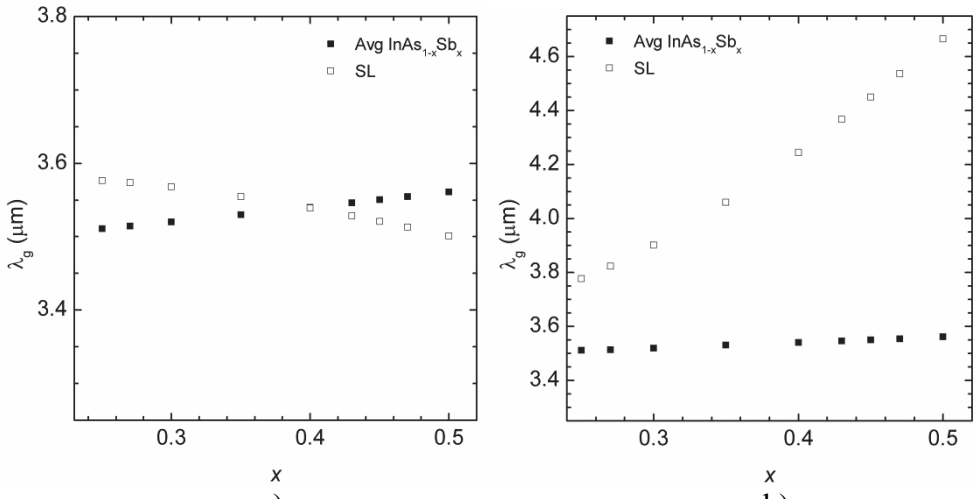

Figure 10. Comparison of strain-balanced SL bandgaps for a) 1 Å and b) 10 Å thick $InAs_{1-x}Sb_x$ layers and the corresponding $InAs_{1-x}Sb_x$ bulk material bandgap with an average composition, given by Eq (93), corresponding to the SL.

the x range shown and are approximately equal at x = 0.40. As x increases, the average SL composition $\bar{x}$ increases which results in a smaller $InAs_{1-x}Sb_x$ bandgap, or longer wavelength. The SL bandgap increases, or the wavelength becomes shorter, as x increases with the small layer widths due to the heavy-hole being potential well becoming deeper. From x = 0.25 to 0.50, the SL bandgap changes only 7 meV between the strain-balanced designs with 1 Å thick $InAs_{1-}$

$_xSb_x$ layers, and the corresponding average $InAs_{1-x}Sb_x$ bandgap changes only 5 meV. This explains why the SL bandgap appears constant in Figure 8 for the short-period limit of the three-band envelope function approximation model. The limit of the envelope function approximation is reached for such thin layers and a more sophisticated model capable of handling such thin atomic layers, such as empirical tight binding or pseudopotential calculations, would be necessary to further investigate these SLs in this regime.

Given the relatively constant SL bandgap regardless of the Sb composition for short periods, $InAs/InAs_{1-x}Sb_x$ strain-balanced SL designs should be chosen with periods greater than some limit to take advantage of the SL properties. The individual InAs and $InAs_{1-x}Sb_x$ layer thicknesses for the designs in Figure 8 are shown in Figure 11 and Figure 12, respectively. The InAs and the $InAs_{1-x}Sb_x$ layer thicknesses should be greater than 50 Å and 4 Å, respectively, to observe differences in the SL designs. Also noticeable in Figure 11 and Figure 12 is the gradual change in the SL bandgap, approaching an upper wavelength limit, above certain layer thicknesses.

The thickness where the SL bandgap begins to approach an upper limit is thinner for lower Sb compositions due to the smaller valence band offset. As the layers become thicker, the change in the quantum well energy levels becomes less per unit change in thickness resulting in the gradual change in the SL bandgap. Eventually, if the layers become thick enough, the SL effect is again lost, and only the bandgaps of the two bulk materials will be visible in the optical properties. Thus, the SL period cannot become too thick, but there is also a

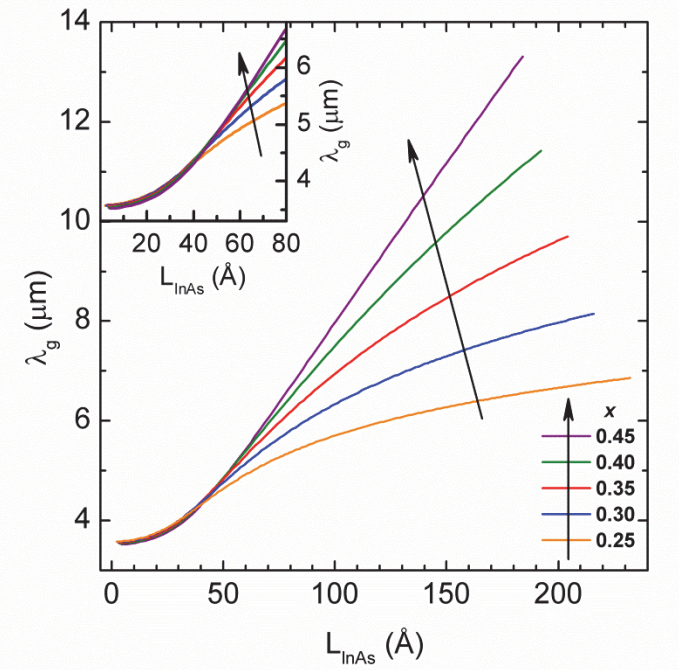

Figure 11. The SL bandgap versus the InAs layer thickness showing the bandgap limit as the period becomes shorter.

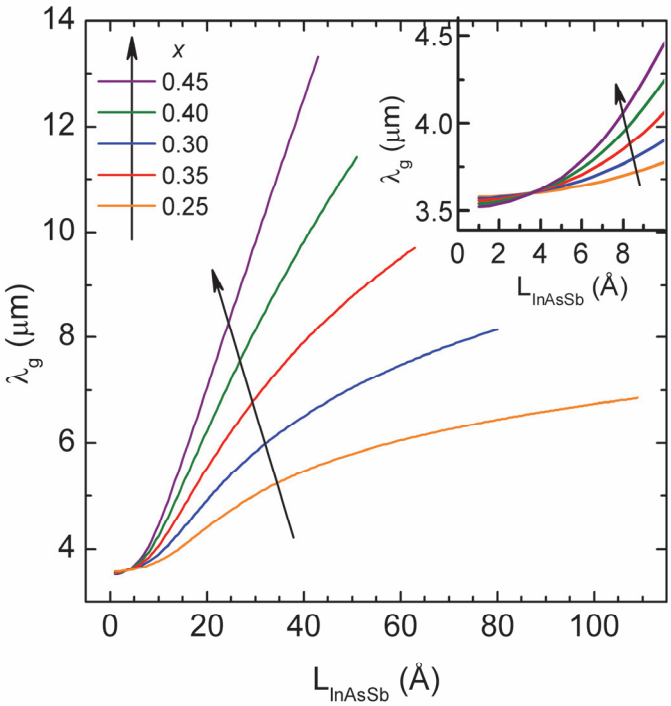

Figure 12. The SL bandgap versus the InAsSb layer thickness showing the bandgap limit as the period becomes shorter.

tradeoff between designing the SL period to be short for high wave function overlap to increase the absorption and avoiding the short-period limit where the SL behaves essentially as a bulk $InAs_{1-x}Sb_x$ material with a bandgap of ~3.5 μm.

The three-band model can calculate the band structure in the growth direction only (E-k_z or E-q) since it is valid at the center of the in-plane Brillouin zone ($k_\perp = 0$). The band structure in the first Brillouin zone in the z-direction is shown in Figure 13 for InAs 67 Å, $InAs_{1-x}Sb_x$ 18 Å, and four different x values. These designs are not all strain-balanced as they all have the same layer thicknesses.

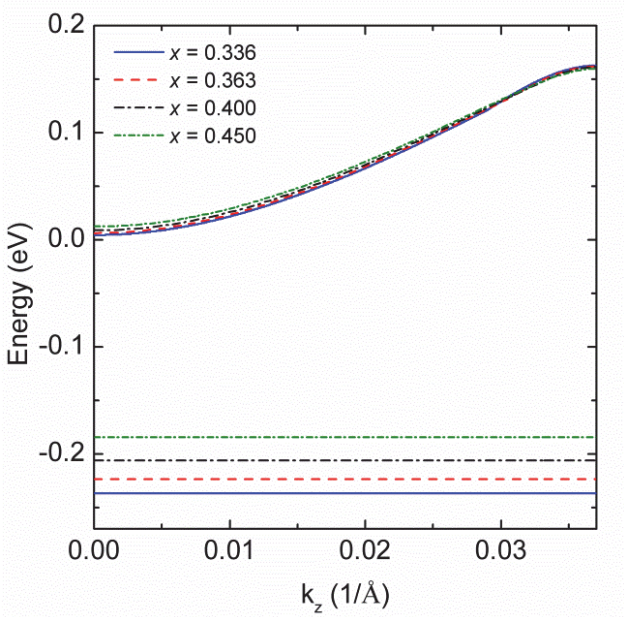

Figure 13. The InAs (67 Å)/$InAs_{1-x}Sb_x$ (18 Å) SL band structure in the growth direction calculated with the three-band model for four different Sb compositions.

The heavy-hole band is extremely flat, indicating an infinite effective mass in the z-direction, and the heavy-hole band becomes higher in energy for larger x values, resulting in smaller bandgaps. The electron energy band changes much less with x at $k = 0$ than the heavy-hole band and remains essentially unchanged at the

Brillouin zone edge. The effects of changing the strain-balanced SL period, L = 172 Å (InAs) + 72 Å ($InAs_{1-x}Sb_x$), on the band structure are shown in Figure 14 for $x = 0.284$.

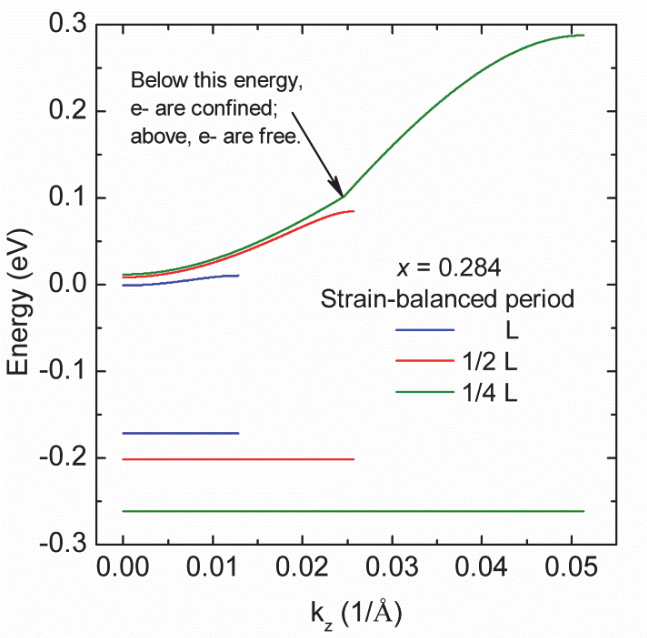

Figure 14. The $InAs/InAs_{0.716}Sb_{0.284}$ SL band structure in the growth direction calculated with the three-band model for three different strain-balanced SL periods: L, ½ L, and ¼ L.

Of course, the length of the Brillouin zone increases as the period decreases, and the width of the electron miniband increases in energy. In the case of ¼L, the period becomes small enough that the entire first electron miniband is not confined below the electron barrier height, and a kink is seen in the curve due to the confined electron equation being used when the electron is above the barrier height. Instead, Eq. (57) should be used when modified for the case of $E > V_o$ in Figure 6. The increased curvature of the electron miniband as the period decreases indicates the effective mass is becoming lighter and the density of states per energy is decreasing as the strain-balanced period decreases. Here again is a

conflict when optimizing the absorption: increasing the SL wave function overlap requires decreasing the SL period which in turn decreases the density of states. In order to calculate the full SL absorption spectrum, the in-plane band structure must also be known and the **k·p** model becomes a better model for the task.

3. MOCVD GROWTH AND CHARACTERIZATION OF $InAs/InAs_{1-x}Sb_x$ SUPERLATTICES

There are several methods to grow epitaxial semiconductor materials, but here the focus will be on just metalorganic chemical vapor deposition (MOCVD) and molecular beam epitaxy (MBE). MOCVD is a higher-yield, lower-cost production method, which is beneficial for the mass production of devices. However, currently, MOCVD-growth of group-III-Sb materials is more difficult than MBE-growth of the same materials. It is still of interest to investigate the growth of $InAs/InAs_{1-x}Sb_x$ SLs by both methods, and ideally, a comparison could be made between the same materials grown by the two methods.

3.1 Metalorganic chemical vapor deposition growth of $InAs/InAs_{1-x}Sb_x$ superlattices

Advances in SL LWIR photodetectors are determined by advances in SL material quality and background doping, which depend on the growth process. A reproducible method for low background carrier concentration (doping) is needed for metalorganic chemical vapor deposition (MOCVD) growth [76] in order to reduce the thermal generation rate, which is responsible for some of the detector dark current. As MOCVD growth and sources have matured, it was expected that lower background doping levels would become possible, and the low-cost production advantage of MOCVD could be used to grow SLs with precise control of the material composition [28]. However, in 1990, the SL background doping was found to be 10^{16} cm^{-3} from Hall measurements [28], and it is currently

10^{16} cm^{-3} for MOCVD InAs/GaSb SLs [77]. Obviously there is still room for growth improvement.

The first set of InAs/$InAs_{1-x}Sb_x$ T2SL samples in this work was grown by MOCVD on 2 in. (100) n-GaSb substrates by Professor Russell Dupuis' group at the Georgia Institute of Technology. The group-III precursors used were trimethylindium (TMIn, $In(CH_3)_3$) and triethylgallium (TEGa, $Ga(C_2H_5)_3$), and the group-V precursors were trimethylantimony (TMSb, $Sb(CH_3)_3$) and arsine (AsH_3). The n-GaSb substrate was cleaned prior to growth in HCl to remove the native surface oxide and then rinsed in isopropyl alcohol and blown dry with N_2. The growth began by depositing a nominal 100 nm GaSb buffer layer at 600 ºC. Then the growth temperature was ramped down to 500 ºC to grow the InAs/$InAs_{1-x}Sb_x$ T2SL at a growth rate of 0.1 nm/s [20].

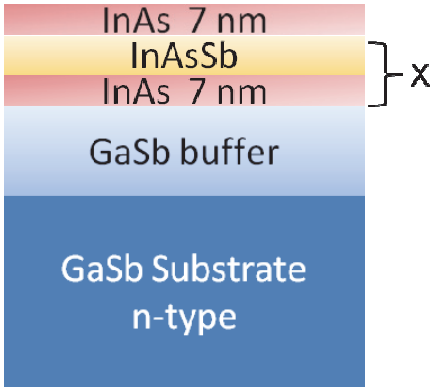

Figure 15. Schematic structure of sample set 1 grown by MOCVD.

The details of the MOCVD sample structures as determined by X-ray diffraction (XRD) measurements are shown in Figure 15 and Table 6. The InAs and $InAs_{1-x}Sb_x$ layer thicknesses are assumed to be the values from the growth calibrations because the SL periods from the XRD measurements agreed with the

designed periods, and the individual SL layer thicknesses were not available from the XRD data.

Table 6. Sample set 1 grown by MOCVD.

Sample Set 1	x ± 1 (%)	Thickness (nm)		Number of Periods X	Buffer layer thickness (nm)
		InAs	$InAs_{1-x}$ Sb_x		
A (3-2006)	22	7.0	3.3	100	100
B (3-2008)	23	7.0	2.3	50	67
C (3-2009)	37	7.0	2.0	50	85

3.2 Characterization of $InAs/InAs_{1-x}Sb_x$ superlattices grown by metalorganic chemical vapor deposition

3.2.1 X-ray diffraction

The (004) and (224) *ω-2θ* coupled high-resolution XRD patterns were recorded using a PANalytical X'Pert Pro MRD. The simulation results closely agree with the experimental data, as shown in Figure 16 for the (004) patterns.

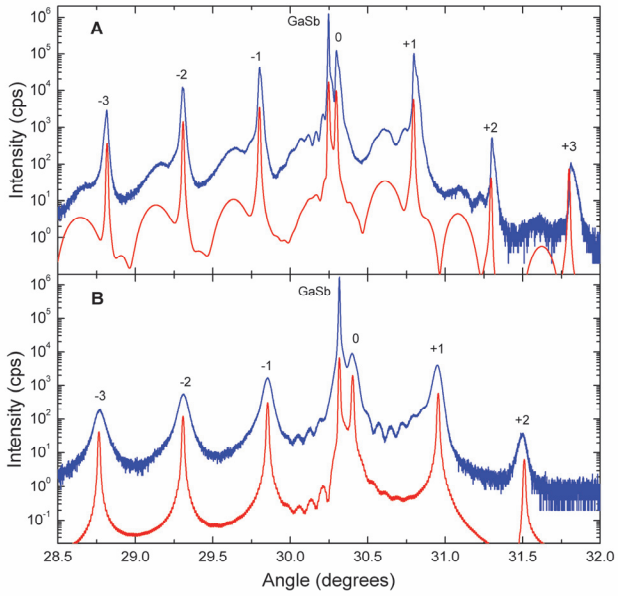

Figure 16. High-resolution (004) *ω-2θ* XRD patterns and simulations (offset below each measurement) for MOCVD samples A and B.

Sample A shows intense satellite peaks with narrow full width at half maximum (FWHMs) of less than 100 arc sec, indicating the high degree of crystallinity and

uniform periodicity of this SL structure. Some variation in the $InAs_{1-x}Sb_x$ composition, however, is evident from the peaks' shapes. The simulation used varying Sb compositions for different portions of the 100 periods. The most intense SL satellite peaks correspond to an average x = 0.22 in the $InAs_{1-x}Sb_x$ layer for the majority of the periods, while the broader, less intense, periodic shoulder peaks are simulated well with just a few periods containing x = 0.35. The average relaxation of the SL was 74%, as determined from (224) *ω-2θ* coupled scans. The satellite peaks of sample B are broader than those of sample A, and the simulated pattern of sample B in Figure 16 uses 83% relaxation and x = 0.23 derived from (224) ω-2θ coupled scans. The SL zero-order (SL0) peaks have FWHMs of 50 and 166 arc sec for samples A and B, respectively, and the SL0 peak for sample C overlaps with the substrate peak. The XRD patterns of sample C exhibited relaxation as well, shown in Figure 17.

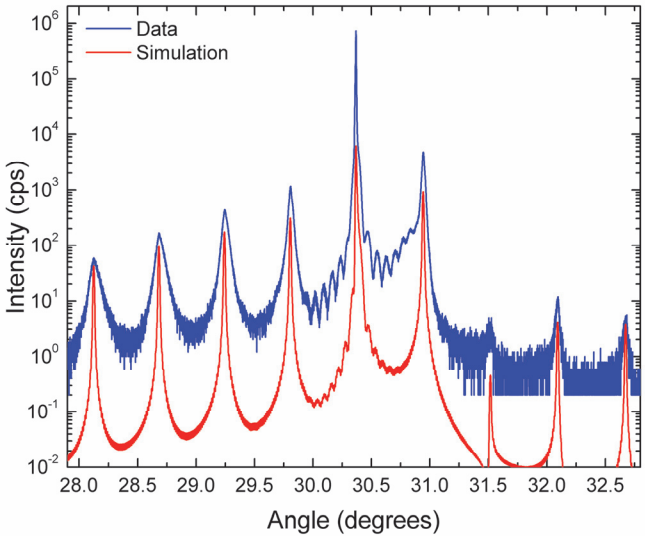

Figure 17. High-resolution (004) *ω-2θ* XRD pattern and simulation (offset below the measurement) for MOCVD sample C.

3.2.2 Atomic force microscopy

Atomic force microscopy (AFM) is used to image surfaces down to the nanometer scale regardless of the conducting properties of the material. The features of the surface are indicative of the defects in the material below the surface. An atomically smooth surface is desired (~2 Å), but strain relaxation and other effects cause defects in the material.

Figure 18 shows a 90 µm x 90 µm AFM scan of MOCVD sample A. A peak defect and some ripples are visible, consistent with the XRD result of the SL being 74 % relaxed. Four line profiles, not including the tall defect, are shown in Figure 19 for the same image in Figure 18. The average root-mean-square (RMS) height of the four line profiles is approximately 15 Å. RMS roughness on the order of 2 Å is desirable for atomic layer growth.

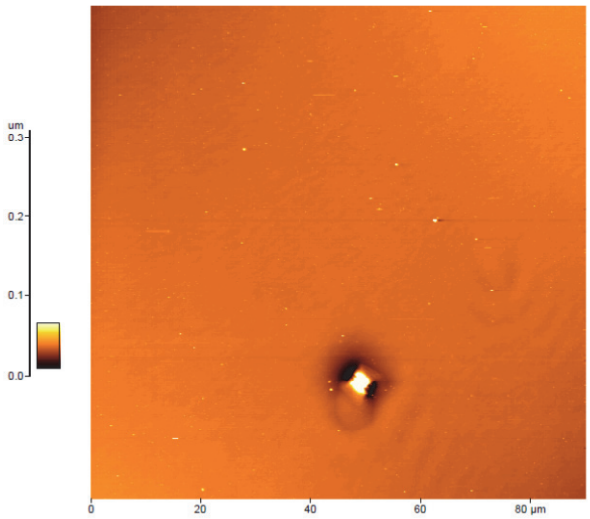

Figure 18. 90 µm x 90 µm AFM scan of MOCVD sample A showing a defect and surface ripples. **Image acquired by Lawrence Grazulis at the AFRL/RXPS.*

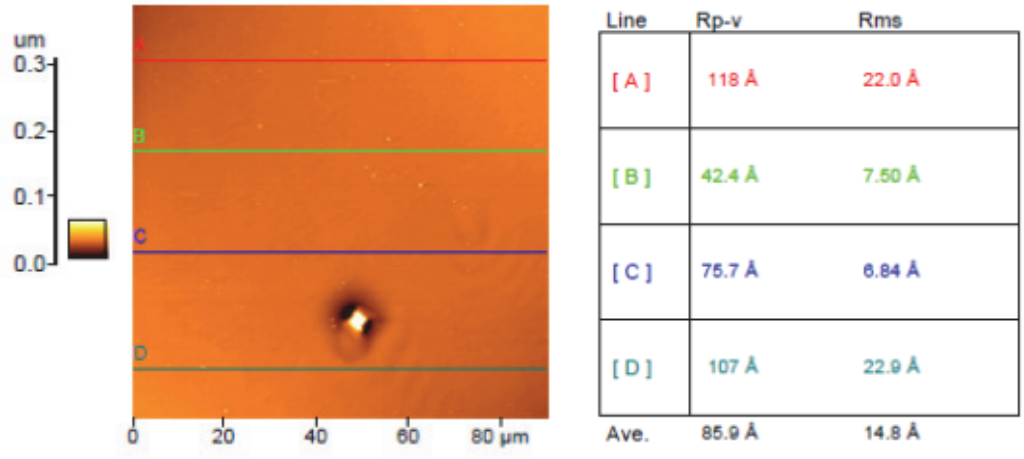

Figure 19. Four line profiles on the 90 µm x 90 µm AFM scan of MOCVD sample A. The average RMS roughness is ~15 Å. **Image acquired by Lawrence Grazulis at the AFRL/RXPS.*

The 50 µm x 50 µm AFM scan for MOCVD sample B in Figure 20 shows many mounds on the order of several microns in area. The bright white spots are most likely artifacts due to debris temporarily stuck on the AFM tip. Four line profiles for this image (Figure 21) have an average RMS roughness of approximately 17 Å, which is slightly higher than that of sample A.

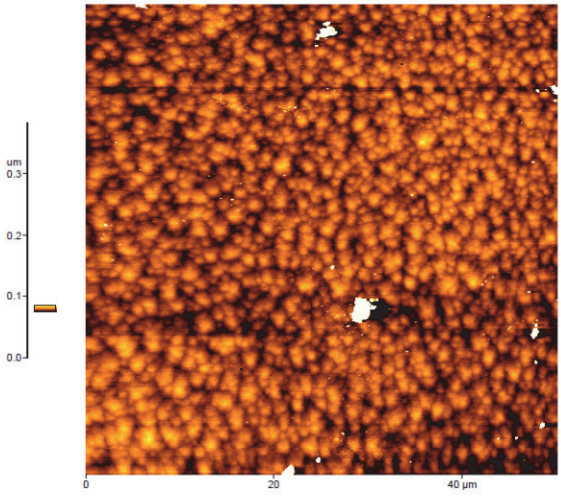

Figure 20. 50 µm x 50 µm AFM scan of MOCVD sample B showing many micron-sized mounds. **Image acquired by Lawrence Grazulis at the AFRL/RXPS.*

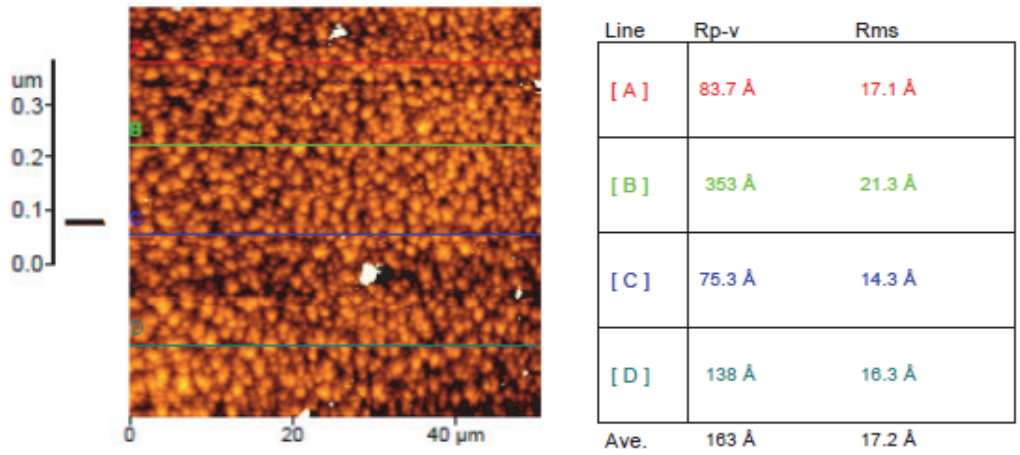

Figure 21. Four line profiles on the 50 µm x 50 µm AFM scan of MOCVD sample B. The average RMS roughness is ~17 Å. **Image acquired by Lawrence Grazulis at the AFRL/RXPS.*

The 50 µm x 50 µm AFM scan for MOCVD sample C in Figure 22 shows many tall pillars and mounds on the order of several microns in area. Four line profiles for this image (Figure 23) have an average RMS roughness of approximately 417 Å, which is an order of magnitude higher than that of sample A or B. Clearly, this sample has many defects that are detrimental to the material quality.

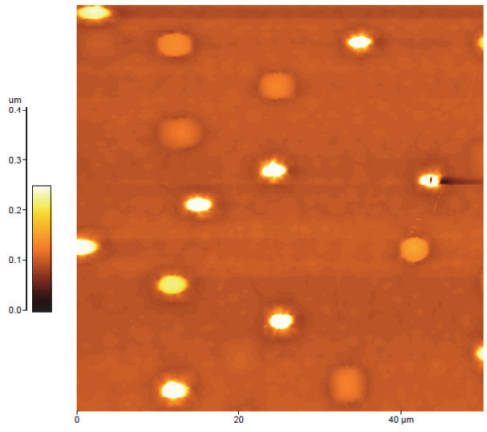

Figure 22. 50 µm x 50 µm AFM scan of MOCVD sample C showing several pillars with areas of microns. **Image acquired by Lawrence Grazulis at the AFRL/RXPS.*

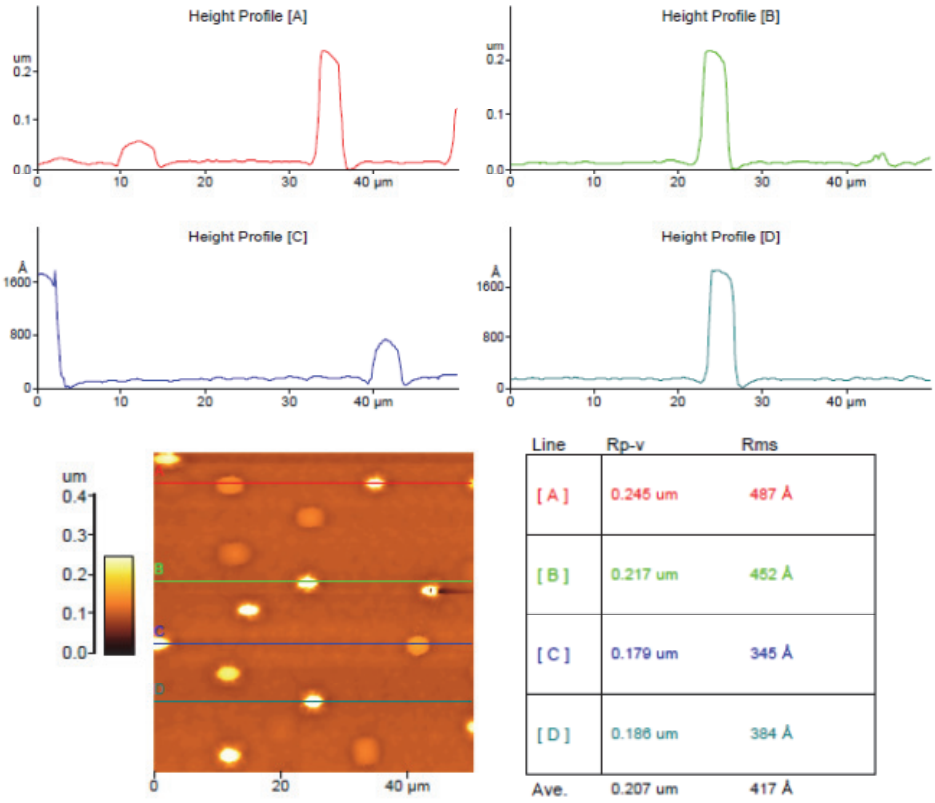

Figure 23. Four line profiles on the 50 µm x 50 µm AFM scan of MOCVD sample C showing 200 nm tall pillars and 50-80 nm tall mounds. The average RMS roughness of the four line profiles is 417 Å. **Image acquired by Lawrence Grazulis at the AFRL/RXPS.*

3.2.3 Transmission electron microscopy

Specimens for cross-sectional transmission electron microscopy (TEM) observation were prepared by standard mechanical polishing, dimpling, and argon-ion-milling at reduced energy (2 – 2.5 keV), with the sample held at liquid-nitrogen temperature (77 K) to minimize thermal and ion-beam damage. Figure 24 shows a cross-sectional TEM image of a portion of the 100 periods of MOCVD sample A, which confirms the very high crystallinity of this specimen near the substrate. In contrast, MOCVD samples B (Figure 25) and C (Figure 26) showed the presence of considerable growth defects, especially {111}-type

stacking faults, originating at either the substrate/buffer interface or the buffer/SL interface, and propagating well into the SL region. These defects contribute significantly towards broadening the FWHM of the XRD satellite peaks [34].

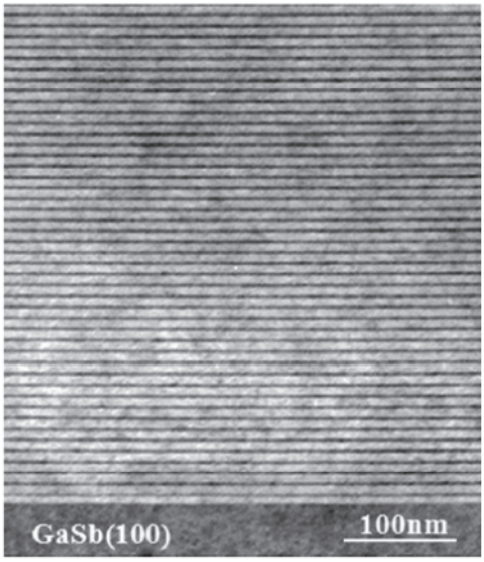

Figure 24. Cross-sectional transmission electron micrograph of MOCVD sample A demonstrating excellent crystallinity of the InAs/$InAs_{1-x}Sb_x$ T2SL. **Image acquired by Lu Ouyang and Dr. David Smith at ASU.*

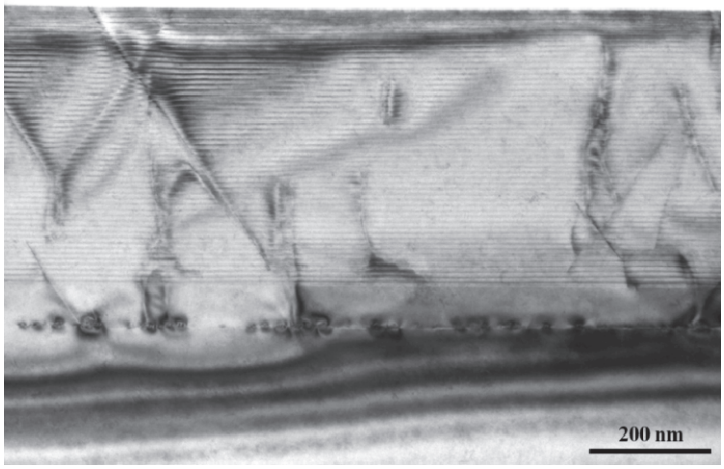

Figure 25. Cross-sectional transmission electron micrograph of MOCVD sample B showing several defects and dislocations, some originating at the substrate/buffer interface and some at the buffer/InAs/$InAs_{1-x}Sb_x$ T2SL interface. **Image acquired by Lu Ouyang and Dr. David Smith at ASU.*

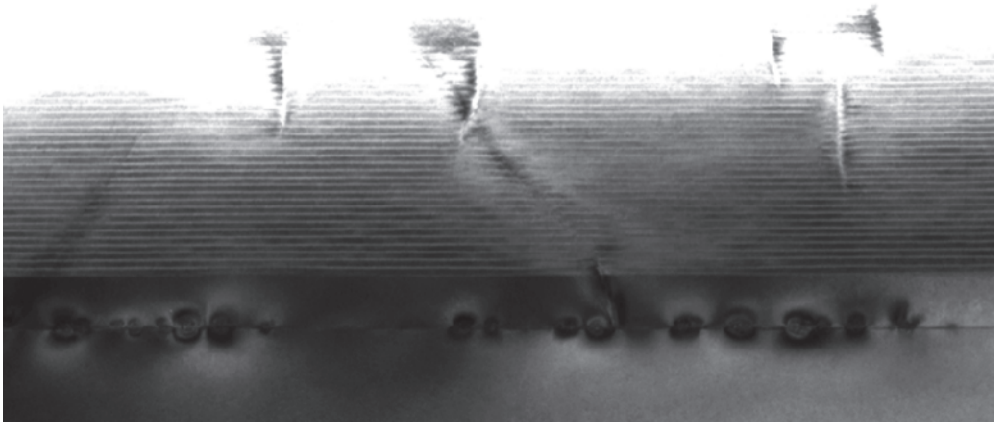

Figure 26. Cross-sectional transmission electron micrograph of MOCVD sample C showing many defects at the substrate/buffer interface and some defects in the InAs/$InAs_{1-x}Sb_x$ T2SL interface. **Image acquired by Lu Ouyang and Dr. David Smith at ASU.*

The MOCVD T2SLs' structural properties shown above reveal that there is more work to do to optimize the MOCVD growth process for these SLs. Despite the non-optimized growth conditions, these samples still had measurable optical properties, as shown in the following photoluminescence (PL) and photoconductance (PC) responses.

3.2.4 Photoluminescence

The low temperature PL spectra for samples A and B are shown in Figure 27. The data were acquired using a double-modulation technique (discussed in Section 5.1) with a Fourier transform infrared (FTIR) spectrometer to suppress the background 300 K blackbody radiation noise near 10 μm. However, the increasing background noise is still visible in the spectra near the MCT detector cutoff at 12 μm due to non-optimized measurement conditions. The 532 nm pump laser was modulated at 60 kHz.

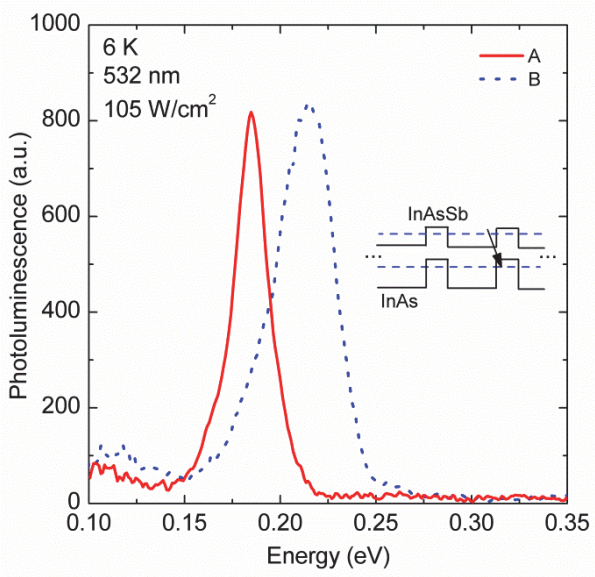

Figure 27. Photoluminescence spectra at 6 K for MOCVD samples A and B. The inset shows the type-II band alignment between InAs and InAsSb. **Data acquired at AFRL/RXPS.*

Using a Lorentzian fit to the data, the peak position, intensity, and FWHM for sample A are 185 meV, 822 a.u., and 20 meV and for sample B are 213 meV, 872 a.u., and 32 meV. The PL intensity is comparable for both samples measured under the same conditions, but the FWHM of sample B's spectrum is 60 % larger than that of sample A, due to the higher density of defects, as deduced from the TEM, and the higher degree of relaxation in sample B. PL from sample C, however, was not measurable, presumably due to defects that occurred during relaxation.

3.2.5 Photoconductance

The spectral photoconductivity of all three samples was measured using a BioRad FTIR at increasing temperatures from 10 K until the signal disappeared – up to 250 K for sample A, 77 K for sample B, and just at 10 K for sample C. A

bias current of 4 mA for sample A and C and 0.5 mA for sample B was applied at indium contacts on the top surface of the samples. The individual photoconductivity signals were corrected for the background with a reference spectrum. Figure 28 shows the temperature-dependent spectral photoresponse (PR) for sample A with a strong response up to 200 K (absorption onset at 8.6 μm) and sample B with response up to 60 K (absorption onset at 5.9 μm). To determine the onset of PR, a linear fit was made to the steep segment of the response as it approached zero, and the x-intercept of the linear function was taken as the PR onset.

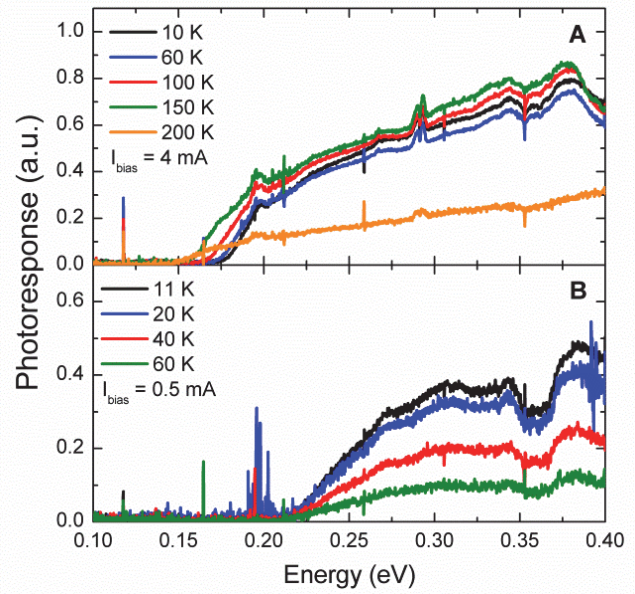

Figure 28. The temperature-dependent spectral photoresponse of MOCVD sample A, showing strong signals up to 200 K and out to 8.6 μm (145 meV), and MOCVD sample B, showing signals up to 60 K and out to 5.9 μm (210 meV). **Data acquired at AFRL/RXPS.*

Table 7 shows the comparison of the PL peak position and the PR onset, and Figure 29 displays the actual measurements. The PL peak position and the photoresponse onset differ by +8 meV and -1 meV for A and B, respectively. These shifts are mainly due to the band bending, band filling, and bandgap renormalization effects at the present PL pump intensity and the alloy and layer thickness fluctuations in the samples. For sample A, the PL peak position is higher in energy than the PR onset, due to the band filling effect caused by the relatively high pump power intensity. The broader the PL peak, as is the case for sample B versus A, the greater the Stokes shift. Taking the SL relaxation into account, the calculated values follow the same trend as the measured values, although there is discrepancy due to the measurement uncertainty of x (± 1 %), the layer thicknesses, and the relaxation.

Table 7. Calculated bandgaps, photoresponse onset, and photoluminescence peak locations for MOCVD sample set 1.

Sample Set 1	x ± 1 (%)	Thickness (nm)		Number of periods	Calculated E_g at 0 K (meV)	PR onset at 10 K (meV)	PL peak position at 6 K (meV)
		InAs	InAsSb				
A (3-2006)	22	7.0	3.3	100	224	177	185
B (3-2008)	23	7.0	2.3	50	250	214	213
C (3-2009)	37	7.0	2.0	50	171	130	–

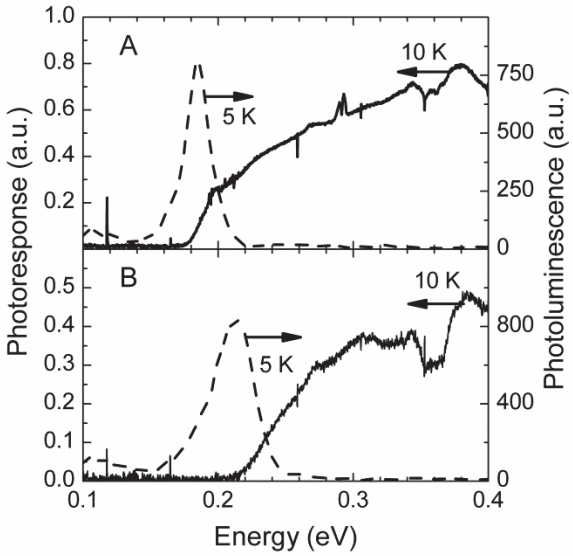

Figure 29. Photoresponse (photoconductivity) and PL spectra for samples A, B.
**Data acquired at AFRL/RXPS.*

Fitting the photoresponse onset of A to the empirical Varshni equation (see Eq. (93) below) results in fitting parameters $\alpha = 0.275 \pm 0.028$ meV/K and $\beta = 139 \pm 34$ K. α is closer to that of InAs (0.276 meV/K) than InSb (0.320 meV/K), but β is between that of InAs (93 K) and InSb (170 K) [45]. The InAs layers are thicker than the InAsSb layers, so the parameters are expected to be nearer to the InAs values.

$$E_g(T) = E_g(0) - \frac{\alpha T^2}{(\beta + T)} \tag{93}$$

The analytical Fan expression (see Eq. (94) [78]), or Bose-Einstein expression [79], is also used to fit bandgap temperature dependence and results in Fan parameter $A = 27.1 \pm 3.6$ meV and average phonon energy $\langle E_p \rangle = 10.7 \pm 1.1$ meV.

$$E_g(T) = E_g(0) - \frac{A}{\left(e^{\frac{\langle E_p \rangle}{kT}} - 1\right)} \tag{94}$$

The Varshni equation fit (solid lines) and the Fan expression fit (dotted lines) using these same parameters for both A and B are shown in Figure 30, along with the temperature dependent PL spectra in the insets.

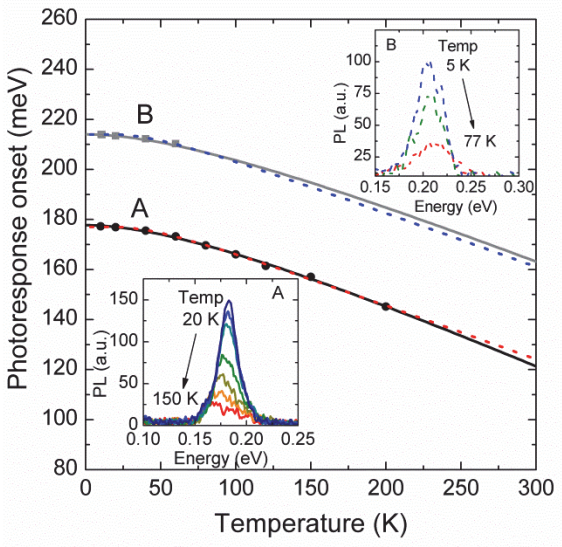

Figure 30. Varshni fit (solid lines) to the absorption onset for samples A and B using α = 0.275 meV/K and β = 139 K and Fan fit (dotted lines) using A = 27.1 meV and <*Ep*> = 10.7 meV. Insets: temperature dependent PL. **Data acquired at AFRL/RXPS.*

The reported Fan parameter (A) values for InAs are 44 meV and 20 meV and the $\langle E_p \rangle$ values are 16 meV and 13 meV [80]. The Fan parameter for InSb is 26.5 meV and 37.6 meV and $\langle E_p \rangle$ is 9.6 meV and 12.5 meV from fitting the data reported in references [66] and [45] to Eq. (94). Also reported in the literature are the Fan parameters for bulk $InAs_{0.05}Sb_{0.95}$: $A = 214 \pm 20$ meV and $\langle E_p \rangle = 40$ meV $\pm$ 4 meV [79]. The Fan results for the SL sample A here are comparable to those of InAs and InSb but smaller than those of the bulk $InAs_{0.05}Sb_{0.95}$.

The Varshni parameter β is considered to be close to the Debye temperature (Θ_D), which is calculated from the Fan average phonon energy as $\Theta_D = \langle E_p \rangle / k$. When kT is much greater than $\langle E_p \rangle$, the Varshni and Fan expressions are equivalent and related by $A/\alpha' = \langle E_p \rangle / k$, where α' is the slope of the Varshni $E_g(T)$. When kT is less than $\langle E_p \rangle$, the Fan expression generally provides a better fit to the data. For sample A in the region $T > 100$ K, $\alpha' = 0.206$ meV/K, agreeing with the Varshni equation overestimating α [80]. When comparing $\beta = 139$ K, $\Theta_D = 124$ K, and $A/\alpha' = 131$ K, the values are consistent with each other but less than the Debye temperatures for InAs (247 K) and InSb (206 K) [81]. The lower Debye temperature for the SL indicates fewer total phonon modes, which could indicate a lower probability for non-radiative recombination processes in the SL. Further temperature-dependent analysis on more InAs/$InAs_{1-x}Sb_x$ SL samples is necessary to determine the consistency of the values given here. See Section Photoluminescence for temperature-dependent PL results on several MBE-grown samples.

In summary, strong, narrow satellite peaks in the x-ray diffraction pattern and minimal defects in the transmission electron micrograph revealed the excellent structural properties of strain-balanced InAs/$InAs_{1-x}Sb_x$ T2SL sample A grown by MOCVD. In addition, intense photoluminescence spectra and photoconductivity spectral responses up to 200 K at 8.6 μm were observed. The structural properties plus the strong optical responses, despite relaxation occurring, warrant further investigation of these superlattice materials grown by MOCVD for infrared photodetector applications.

4. MBE GROWTH AND CHARACTERIZATION OF $InAs/InAs_{1-x}Sb_x$ SUPERLATTICES

Antimonide-based type-II superlattices (T2SLs) have many potential advantages over bulk HgCdTe for infrared photodetector materials [2], with the $InAs/Ga_{1-x}In_xSb$ T2SL being the most investigated. However, short minority carrier lifetimes [38, 82] in $InAs/Ga_{1-x}In_xSb$ T2SLs are detrimental to the detector dark current and quantum efficiency [83] and have recently been partially attributed to acceptor-like defects in GaSb [38] rather than the interfaces [84]. With Ga being the suspected culprit of the short minority carrier lifetime, the Ga-free $InAs/InAs_{1-x}Sb_x$ T2SL has the potential for longer lifetimes. The "stabilized Fermi level" due to intrinsic point defects in bulk InAs is expected to be above the conduction band edge [42], rendering any mid-gap defect states inactive for Shockley-Read-Hall (SRH) processes. In comparison, the stabilized Fermi level for bulk GaSb is expected to be in the bandgap near the valence band edge [42], leaving the mid-gap states available for SRH recombination. Relatively high photoluminescence (PL) efficiencies for 4 – 11 μm emission from $InAs/InAs_{1-x}Sb_x$ T2SLs grown on GaAs with highly dislocated 1 μm InAsSb buffer layers also suggest that As-rich $InAs_{1-x}Sb_x$ alloys have comparatively low SRH recombination coefficients [61]. A minority carrier lifetime of 250 ns [38] reported for bulk $InAs_{0.80}Sb_{0.20}$ having a PL peak at 5.4 μm at 77 K further supports the possibility that the $InAs/InAs_{1-x}Sb_x$ T2SLs may have longer lifetimes than those of the $InAs/Ga_{1-x}In_xSb$ T2SLs. Theoretically calculated absorption of an 11 μm $InAs/InAs_{1-x}Sb_x$ T2SL was lower, but within a factor of two, than that

of a 10 μm InAs/$Ga_{1-x}In_xSb$ T2SL [19]. The theoretical study did not include SRH recombination, leaving open the possibility that in practice, the former T2SL may have higher absorption and a longer minority carrier lifetime than the latter due to interface and growth-related variations [19].

Although not as well studied as InAs/$Ga_{1-x}In_xSb$ T2SLs, $InAs_{1-x}Sb_x$/$InAs_{1-y}Sb_y$ T2SLs have been investigated by several groups since they were first proposed [6] to possibly compete with HgCdTe by utilizing tensile strain to reach longer wavelengths than bulk $InAs_{1-x}Sb_x$. $InAs_{1-x}Sb_x$/$InAs_{1-y}Sb_y$ SLs were grown by both molecular beam epitaxy (MBE) and metalorganic chemical vapor deposition (MOCVD) with complicated strain-relieving buffer layers: i) on InSb for LWIR (8 – 12 μm) photodetectors [76, 85], ii) on InAs for MWIR lasers [18, 48, 86], iii) on GaAs for LWIR LEDs, [57, 61] and iv) on GaSb for LWIR photodetectors [20-22]. The growth of InAs/$InAs_{1-x}Sb_x$ T2SLs on GaSb by MBE has been briefly reported [33]. This chapter reports the MBE growth and characterization of strain-balanced InAs/$InAs_{1-x}Sb_x$ T2SLs on GaSb substrates for MWIR and LWIR detectors.

4.1 Molecular beam epitaxy growth of InAs/$InAs_{1-x}Sb_x$ superlattices

The first growth of an $InAs_{1-y}Sb_y$/$InAs_{1-x}Sb_x$ strained-layer superlattice was of a 1.5 μm thick InSb (50 Å)/$InAs_{0.26}Sb_{0.74}$ (100 Å) SLS on a GaAs substrate by MBE one year after the system was proposed [24]. They found the InAsSb composition to be very sensitive to the antimony (Sb) flux and the substrate temperature. The miscibility gap of $InAs_{1-x}Sb_x$ grown on GaAs with different buffer layers (GaAs, InAs, GaSb, $InAs_{0.50}Sb_{0.50}$) was investigated, and a substrate

growth temperature of 415 °C for GaAs and $InAs_{0.50}Sb_{0.50}$ buffers and 435 °C InAs and GaSb buffers was found to be the minimum temperature, T_c, to avoid phase separation [87]. By introducing annealing interruptions during the $InAs_{1-x}Sb_x$ growth, $InAs_{1-x}Sb_x$ with compositions inside the miscibility gap was grown at temperatures lower than T_c [88]. However, growth interruptions can allow impurities in the growth chamber to enter the material and degrade the material quality.

The second set of InAs/$InAs_{1-x}Sb_x$ T2SL samples in this study was grown by an MBE foundry service provided headed by Prof. Diana Huffaker's group at the California Nanosystems Institute (CNSI) at the University of California Los Angeles. Dr. Kalyan Nunna performed the actual sample growth. Several designs were grown on *n*-GaSb substrates by solid source MBE equipped with valved crackers set up to produce As_2 and Sb_2 species. Following oxide desorption at 530 °C, a GaSb buffer layer was grown at 500 °C. The substrate was then cooled to 435 °C for the growth of the ~500 nm-thick InAs/$InAs_{1-x}Sb_x$ SL, and a final 100 nm GaSb cap layer was grown at 480 °C. Four samples A, B, C, and D with 20 period SLs were grown under identical conditions with varying Sb/(As+Sb) beam equivalent pressure (BEP) flux ratios. The non-unity sticking coefficient of the group V materials, As and Sb, and their competition for incorporation makes it difficult to estimate the proper group V composition. However, by changing only the As flux and keeping all the remaining elements identical, a systematic variation in the Sb incorporation can be achieved. Thus, the $InAs_{1-x}Sb_x$ layers in samples A, B, C, and D have Sb/(As+Sb) BEP ratios of

0.32, 0.347, 0.378, and 0.412, respectively. The Sb composition versus the Sb/(As+Sb) BEP ratios is shown in Figure 31 for these conventional MBE alloys. The sample structure information for set 2 is shown in Figure 32 and Table 8 with the period and $InAs_{1-x}Sb_x$ composition determined by XRD measurements and simulations.

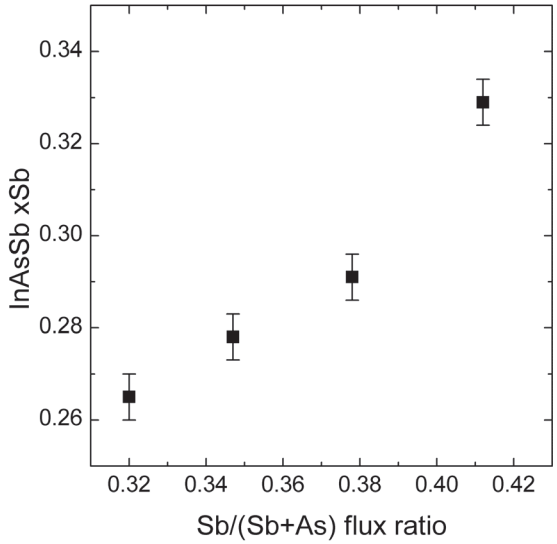

Figure 31. Sb composition in the InAsSb layer versus the Sb/(Sb + As) BEP ratio.

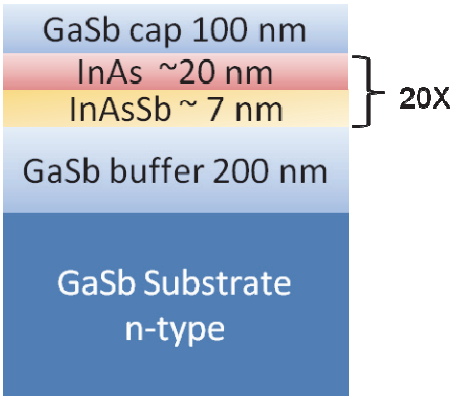

Figure 32. Schematic structure of sample set 2 grown by MBE.

Table 8. Sample set 2 grown by MBE.

Sample Set 2	x ± 0.01	Period ± 0.5 (nm)	Number of Periods	GaSb Cap layer (nm)
A (0203-1)	0.27	26.5	20	100
B (0218-1)	0.28	24.6	20	100
C (0218-2)	0.29	24.6	20	100
D (0218-3)	0.33	24.5	20	100

The third set of InAs/$InAs_{1-x}Sb_x$ T2SL samples was also grown by MBE at the CNSI but with ordered $InAs_{1-x}Sb_x$ layers grown by modulated-MBE (MMBE). The $InAs_{1-x}Sb_x$ layers were composed of a number of InAs/InSb periods grown by keeping the In shutter open while modulating the arsenic (As) and Sb shutters [58]. The As composition in the layer is then given by the As shutter duty cycle as

$$1 - x_{Sb} = x_{As} = \frac{As\_shutter\_time}{(As\_shutter\_time + Sb\_shutter\_time)}. \qquad (95)$$

MMBE was especially advantageous for controlling alloy compositions before valved crackers allowed precise control of the group-V element fluxes. Here the technique is used to see if more abrupt interfaces can be achieved between the $InAs_{1-x}Sb_x$ and InAs layers since As and Sb are known to exchange places during growth. This intermixing alters the layer compositions and thicknesses from the intended design. Using approximately 0.5 monolayer (ML) per second as the InAs and InSb growth rates, the duration of the growth for the ordered layers is shown in Table 9. The ordered alloy layer consists of periods of InAs/InSb, so there is no distinction between the InAs layer and the alloy layer in the SL. Effectively, the InAs layer is slightly thicker and the alloy layer is slightly thinner. The sample structure information for set 3 is also shown in Figure 33 and Table 9

with the period and $InAs_{1-x}Sb_x$ composition determined by XRD measurements and simulations.

Table 9. Sample set 3 grown by MBE with ordered InAsSb alloys.

Sample Set 3	x ± 0.01	Period ± 0.5 (nm)	Number of Periods	Sb Duty Cycle (%)	No. of InAs/InSb periods per $InAs_{1-x}Sb_x$ layer	InSb (s)	InAs (s)
E (0221-1)	22	24.2	20	35	6	3	5.5
F (0221-2)	23	24.1	20	47	6	4	4.5
G (0221-3)	36	24.0	20	47	4	6	6.7

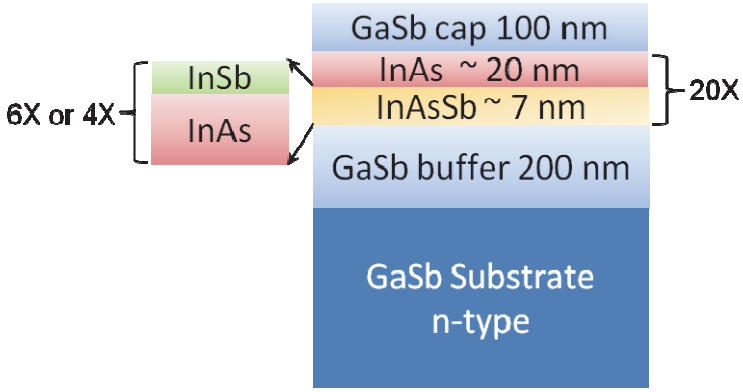

Figure 33. Schematic structure of sample set 3 grown by MBE with ordered InAsSb alloys.

The fourth set of $InAs/InAs_{1-x}Sb_x$ T2SL samples grown by MBE at the CNSI consists of one sample with a conventional $InAs_{1-x}Sb_x$ random alloy (sample H) and one with an ordered $InAs_{1-x}Sb_x$ alloy (sample I). These samples have a smaller period to increase the wave function overlap and 10 nm AlSb layers on either side of the 60-period SL intended to confine electrons to improve the PL signal intensity. They are capped with a 5 nm GaSb layer to prevent the AlSb from oxidizing. The ordered alloy in this case consists of InSb/InAs/InSb periods, where the InSb layer thicknesses are one half of the desired InSb thickness for the specified $InAs_{1-x}Sb_x$ composition, so there is a clear distinction

between the InAs layer and the ordered alloy layer in the SL. Using a slower growth rate of 0.35 ML/s, the duration of the growth for the ordered layers is shown in Figure 34 and Table 10.

Table 10. Sample set 4 grown by MBE with a smaller period and AlSb layers for confinement.

Sample Set 4	x ± 0.01	Period ± 0.5 (nm)	Number of Periods	Sb Duty Cycle (%)	No. of ½InSb/InAs/ ½InSb periods per $InAs_{1-x}Sb_x$ layer	½ InSb (s)	InAs (s)
H (0512-1)	0.30	7.4	60	N/A	N/A	N/A	N/A
I (0512-2)	0.13	7.4	60	33	2	1.5	6

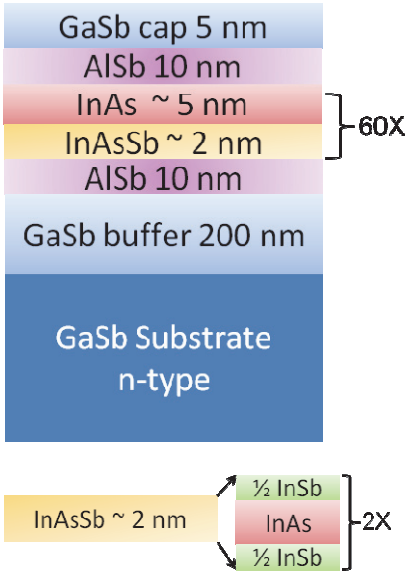

Figure 34. Schematic structure of sample set 4 grown by MBE.

The fifth and last set of InAs/$InAs_{1-x}Sb_x$ T2SL samples was grown by MBE at IQE, Inc. and consists of conventional $InAs_{1-x}Sb_x$ random alloys only. This set also has 10 nm AlSb barrier layers above and below the ~500 nm thick SL but is capped with 10 nm of *p*-InAs rather than GaSb. The sample details are shown in Figure 35 and Table 11.

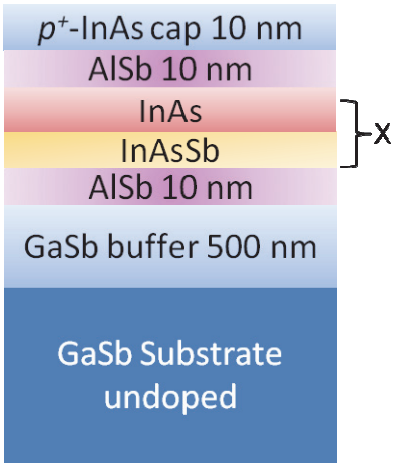

Figure 35. Schematic structure of sample set 5 grown by MBE.

Table 11. Sample set 5 grown by MBE with AlSb barrier layers.

Sample Set 5	x ± 0.01	Period ± 0.5 (nm)	Number of Periods
J (2301027)	0.34	8.48	58
K (2301029)	0.37	8.40	58
L (2301030)	0.39	8.62	58
M (2301031)	0.35	10.72	47
N (2301032)	0.35	9.49	52
O (2301033)	0.28	24.47	20
P (2301043)	0.41	7.30	69
Q (2301044)	0.30	17.95	28
R (2301060)	0.35	9.79	209

4.2 Characterization of InAs/$InAs_{1-x}Sb_x$ superlattices grown by molecular beam epitaxy

4.2.1 X-ray diffraction

The actual SL periods and $InAs_{1-x}Sb_x$ compositions were determined from the growth shutter times and the simulations of (004) ω-2θ coupled high-resolution XRD patterns recorded with a PANalytical X'Pert Pro MRD. The simulations use pseudomorphically strained layers on the GaSb substrate, which is reasonable given the results from a (224) reciprocal space map for MBE sample B: only 0.2% relaxation and x differing by only 0.004, which is within the ± 0.01

error bars, from the (004) ω-2θ scan value. The (224) reciprocal space map is shown in Figure 36, with considerable spread in the omega direction due to using the rocking curve detector with a fairly wide ½° slit. Figure 37 shows the simulation of the nominal design structure (20 nm InAs/7.7 nm $InAs_{0.71}Sb_{0.29}$ SL with a 100 nm GaSb cap layer) for MBE sample sets 2 and 3, and Figure 38 shows the measurement data and simulations for MBE sample set 2.

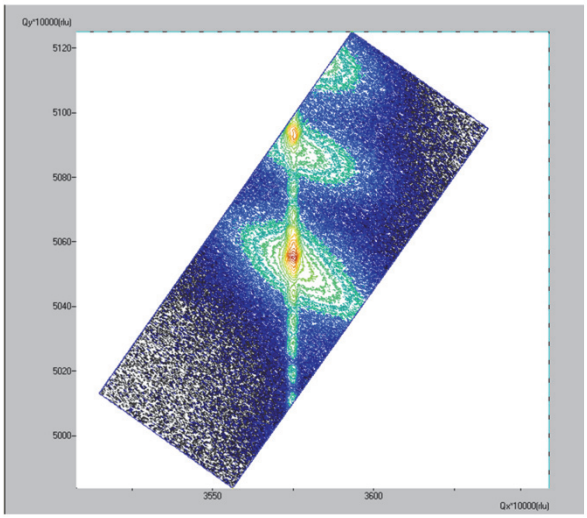

Figure 36. MBE sample B (224) reciprocal space map measured with the rocking curve detector showing psuedomorphic growth. **Data acquired at AFRL/RXPS.*

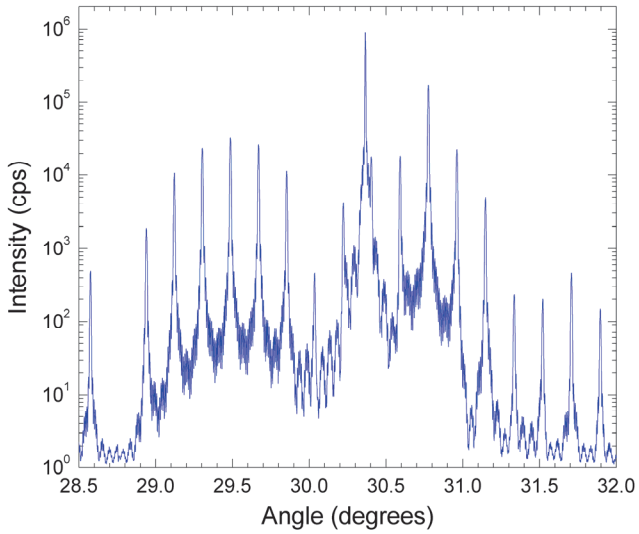

Figure 37. (004) XRD simulation of the nominal structure design for MBE sample sets 2 and 3.

MBE sample C shows more fine structural details (Pendellösung fringes) in the XRD data than the other samples, indicating its high quality and smooth interfaces. The relatively large SL period of ~25 nm causes an envelope function modulation of the SL satellite peak intensities, reflecting the strain of the individual InAs and $InAs_{1-x}Sb_x$ layers, on the right and left of the substrate peak, respectively. These modulations result in the most intense SL satellite peak no longer corresponding to the SL zero-order (SL0) peak. The SL0 peak is hidden within the GaSb substrate

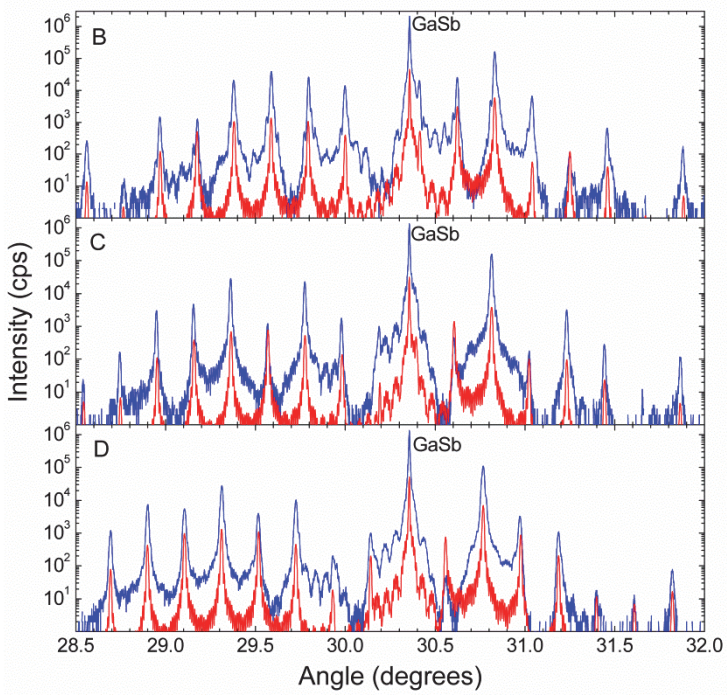

Figure 38. (004) *ω-2θ* XRD patterns and simulations (offset below the data) for MBE sample set 2 samples B, C, and D.

peak for MBE samples C and D. The envelope modulation due to the $InAs_{1-x}Sb_x$ layer moves further from the substrate peak for MBE samples B, C, and D as the Sb composition increases, as expected. The simulation for MBE sample D shown in more detail in Figure 39 displays excellent agreement with the measured data.

However, there is an additional modulation on the SL satellite peaks on the $InAs_{1-x}Sb_x$ side of the GaSb peak evidenced by every other peak having higher intensity that is not reproduced by the simulation. This modulation has a period twice that of the SL satellite peak period, indicating its origin is a periodic layer in the sample with a period half that of the SL period. Simulations of a third $InAs_{1-x}Sb_x$ interfacial layer in the SL period between the InAs and $InAs_{1-x}Sb_x$ layers reveal modulations similar to those shown in Figure 39. A possible cause of this interfacial intermixing is the substrate temperature increase from 435 °C to 480 °C for the growth of the 100 nm GaSb cap layer. A thinner cap layer of ~10 nm would require one tenth the growth time and thus minimize the effect of the 480 °C annealing on the SL structure. Another possibility is Sb segregation resulting in compositionally graded interfaces between the InAs and InAsSb layers.

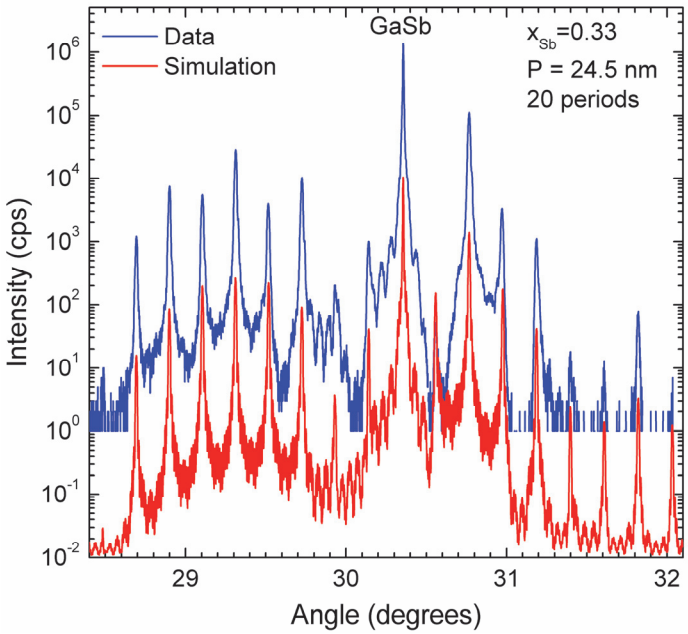

Figure 39. (004) *ω-2θ* XRD simulation results for MBE sample D.

The average SL mismatch with the substrate and the SL0 peak FWHM results are summarized in Table 12. The mismatch and FWHM for samples C and D are in italics to denote the SL0 peak position was calculated, due to its overlap with the substrate peak, based on the period and the SL satellite peak positions and that the FWHM is the mean of all the SL satellite peaks' FWHMs. The average perpendicular SL mismatch is net tensile and less than 0.2 % for all the samples, with sample D being the most closely lattice-matched to GaSb at 0.03 % mismatch.

Table 12. XRD results summary for MBE sample set 2.

Sample	x ± 0.01	Period ± 0.5 (nm)	Number of Periods	XRD SL0 mismatch (ppm)	XRD SL0 peak FWHM (arcsec)
A (0203-1)	0.27	26.5	20	-1930	55
B (0218-1)	0.28	24.6	20	-1754	35
C (0218-2)	0.29	24.6	20	*-1164*	*39*
D (0218-3)	0.33	24.5	20	*-279*	*41*

The XRD measurement results for MBE sample set 3 containing ordered alloys are shown in Figure 40. The SL satellite peaks become broader for samples E, F, and G as the intended Sb composition in the $InAs_{1-x}Sb_x$ ordered alloy increases. To increase the Sb composition, the InSb layer thickness was increased (see Table 9), which resulted in many more defects in samples F and G than in E and thus broader XRD peaks. Sample E was simulated with an InAs layer 17.5 nm thick and an $InAs_{1-x}Sb_x$ ordered alloy containing 6 periods of 8.7 Å of InAs and 2.5 Å of InSb, resulting in $x = 0.22$. The simulation is displayed below the data in Figure 41.

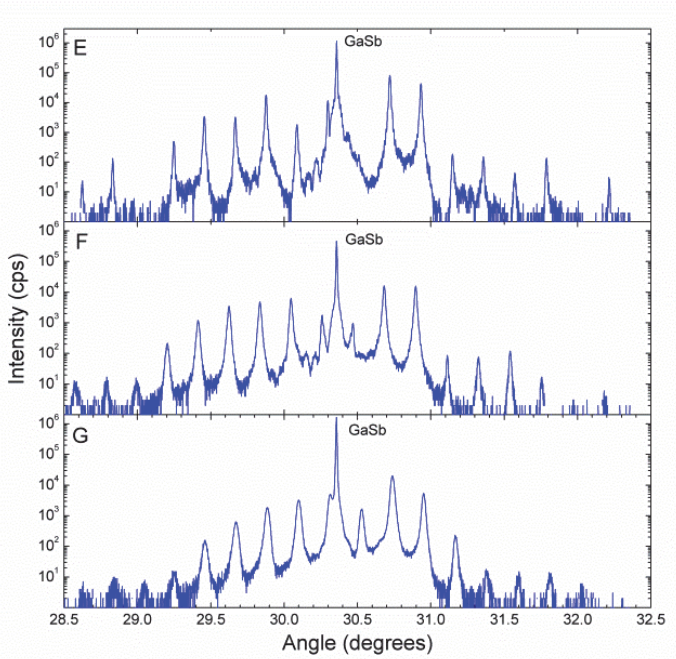

Figure 40. (004) *ω-2θ* XRD patterns for sample set 3 with ordered alloys.

Some InAs/$InAs_{1-x}Sb_x$ interfacial intermixing possibly due to annealing is evident in MBE sample E as well. Sample F was simulated well with a conventional $InAs_{1-x}Sb_x$ alloy with $x = 0.23$, as shown in Figure 42. As will be seen later in the TEM section, only the first period of sample F contained an ordered alloy while the rest of the periods appeared to contain conventional random alloys. Thus simulating the XRD pattern with a conventional alloy makes sense.

Table 13. XRD results summary for MBE sample set 3.

Sample Set 3	x ± 0.01	Period ± 0.5 (nm)	Number of Periods	Sb Duty Cycle (%)	No. of InAs/InSb periods per $InAs_{1-x}Sb_x$ layer	InSb (s)	InAs (s)
E (0221-1)	22	24.2	20	35	6	3	5.5
F (0221-2)	23	24.1	20	47	6	4	4.5
G (0221-3)	36	24.0	20	47	4	6	6.7

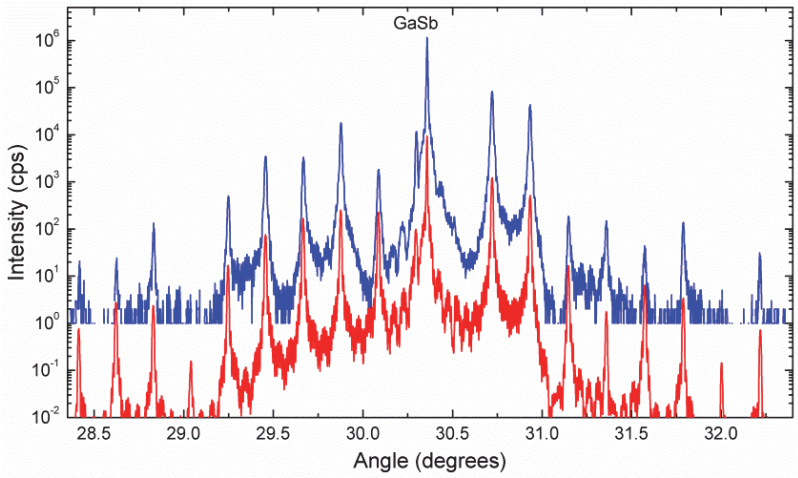

Figure 41. (004) ω-2θ XRD data and simulation (below the data) for MBE sample E. The simulation used an ordered $InAs_{1-x}Sb_x$ alloy.

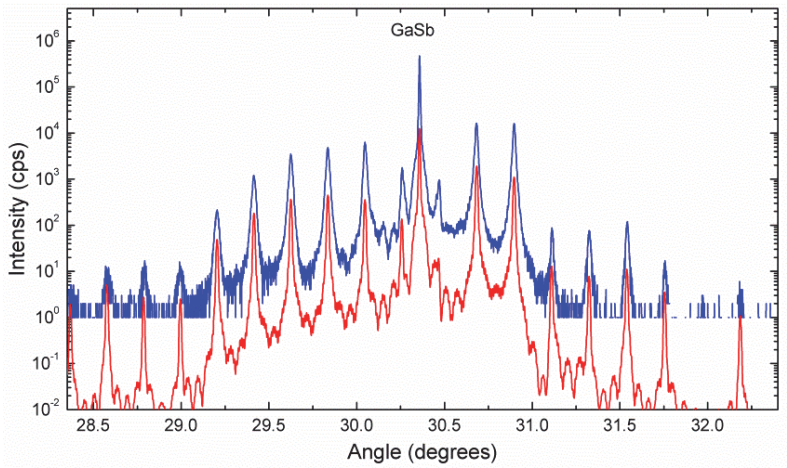

Figure 42. (004) ω-2θ XRD data and simulation (below the data) for MBE sample F. The simulation used a conventional $InAs_{1-x}Sb_x$ alloy.

The smaller SL period in MBE sample set 4 is evident from the greater SL satellite peak spacing in Figure 43. The primary satellite peak intensity modulation near the substrate peak is due to the AlSb barrier layers rather than the individual SL layers, which was the case for the larger period samples. Sample H (conventional alloy) had a grid pattern of cloudy spots on the epi-side of the wafer, possibly due to storing the wafer for months before growing on it, which most likely contributes to the SL satellite peaks having a FWHM (see Table 14)

twice that of sample I (ordered alloy) without a pattern on the epi surface. Either the Sb source was running low during the growth of MBE sample I or the ordered alloy experienced As-Sb intermixing, resulting in the Sb composition being less than one half of its intended value and the average SL mismatch being three times that of sample H.

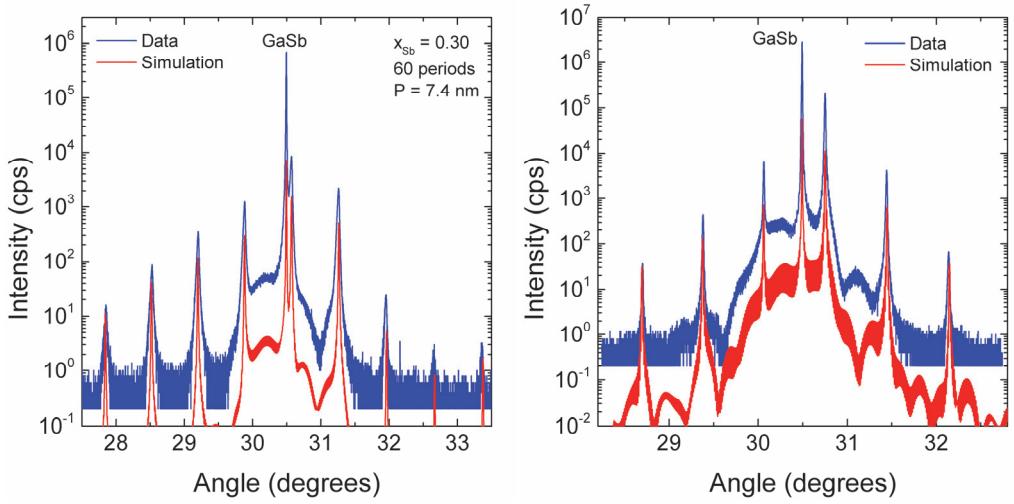

(a) (b)

Figure 43. (004) *ω-2θ* XRD profiles for MBE sample set 4 samples (a) H and (b) I. **Data acquired at AFRL/RXPS.*

Table 14. XRD results summary for MBE sample set 4.

Sample	x ± 0.01	Period ± 0.5 (nm)	Number of Periods	XRD SL0 mismatch (ppm)	XRD SL0 peak FWHM (arcsec)
H (0512-1)	0.30	7.4	60	-2231	92
I (0512-2)	0.13	7.4	60	-7581	45

The SL0 peak mismatch with the GaSb substrate and the SL0 peak FWHM are shown in Table 15 for MBE sample set 5. The majority of the samples in MBE set 5 have smaller SL0 mismatches and SL0 peak FWHMs than the previous sample sets, indicating they are more strain-balanced to the GaSb substrate and have fewer defects. Figure 44 shows the (004) *ω-2θ* XRD pattern

for MBE sample K as an example of the set. Its small period results in wider spacing between the SL satellite peaks, and the influence of the AlSb barrier layers and InAs cap layer is visible between the SL peaks. The closer view of the substrate, SL0, and SL1 peaks in Figure 44b shows the detailed Pendellösung fringes, attesting to the abrupt interfaces and high quality of the sample.

Table 15. XRD results summary for MBE sample set 5.

Sample Set 5	x ± 0.01	Period ± 0.5 (nm)	Number of Periods	XRD SL0 mismatch (ppm)	XRD SL0 peak FWHM (arcsec)
J (2301027)	0.34	8.48	58	-1471	36
K (2301029)	0.37	8.40	58	-997	36
L (2301030)	0.39	8.62	58	-670	40
M (2301031)	0.35	10.72	47	-610	36
N (2301032)	0.35	9.49	52	-759	36
O (2301033)	0.28	24.47	20	-447	40
P (2301043)	0.41	7.30	69	-506	35
Q (2301044)	0.30	17.95	28	-536	30
R (2301060)	0.35	9.79	209	-907	23

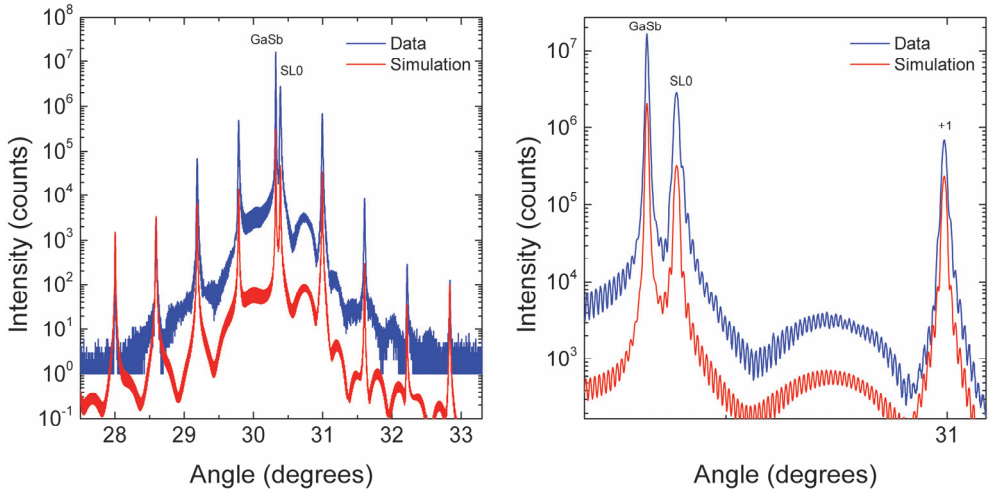

Figure 44. (a) (004) ω-2θ XRD pattern of MBE sample K and (b) a closer view around the substrate and two SL satellite peaks showing many Pendellösung fringes. **Data acquired at AFRL/RXPS.*

Figure 45 displays the (224) reciprocal space map measured using the triple axis detector for the 2μm-thick SL sample R. The spread in the omega

direction is much less than shown in Figure 36 because the triple axis detector was used instead of the rocking curve detector. Use of the triple axis detector also enables streak from the incident hybrid monochromator to be observed. It is seen that this 2μm-thick SL sample was grown pseudomorphically on GaSb without relaxation.

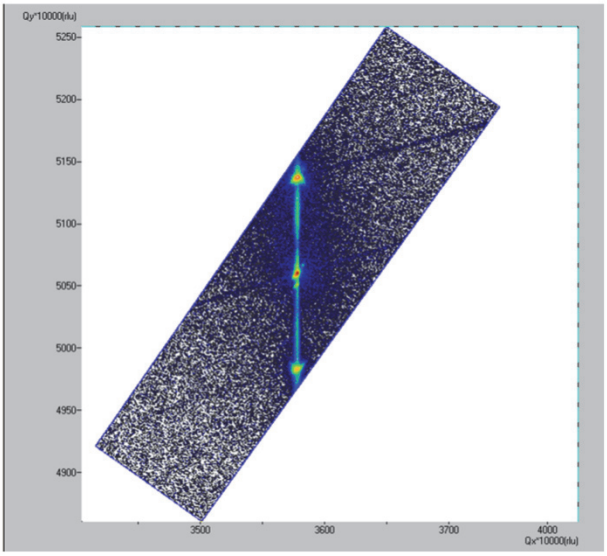

Figure 45. (224) Reciprocal space map of MBE sample R measured with the triple axis detector showing pseudomorphic growth on GaSb for the 2 μm-thick SL. **Data acquired at AFRL/RXPS.*

4.2.2 Atomic Force Microscopy

Figure 46 shows AFM scans of MBE samples B and C. A twin defect and some mounds are visible in Figure 46a for MBE sample B. Figure 46b shows more mounds for MBE sample C than B. The area average RMS roughness of sample C, 6.0 Å, is also higher than that of B, 4.6 Å. Sample D had the smallest average area RMS roughness of 3.1 Å for a 20 μm x 20 μm scan. RMS roughness on the order of 2 Å is desirable for atomic layer growth. AFM scans on MBE sample A were not performed, so the data is not included in Table 16.

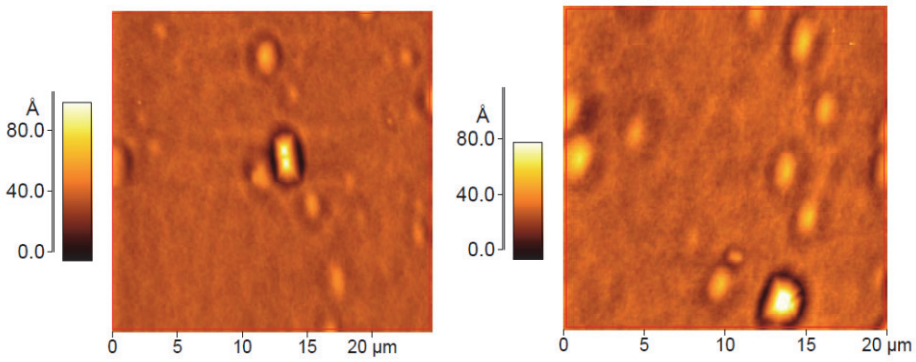

(a) (b)

Figure 46. (a) 25 um x 25 um area AFM image for MBE sample B. (b) 20 um x 20 um area AFM image for MBE sample C. **Image acquired by Lawrence Grazulis at the AFRL/RXPS.*

Table 16. AFM area RMS roughness results for MBE sample set 2.

Sample Set 2	x ± 0.01	Period ± 0.5 (nm)	Number of Periods	Area RMS roughness (Å)	AFM scan area (µm x µm)
A (0203-1)	0.27	26.5	20	Not available	
B (0218-1)	0.28	24.6	20	4.6	25 x 25
C (0218-2)	0.29	24.6	20	6.0	20 x 20
D (0218-3)	0.33	24.5	20	3.1	20 x 20

Only MBE sample E from sample set 3 with ordered alloys was examined with AFM. The 20 µm x 20 µm AFM scan in Figure 47 shows one large defect, but the overall area RMS roughness is quite good at 2.7 Å. MBE samples F and G are expected to have higher area roughness values given the broader XRD SL satellite peaks indicating a higher density of defects than sample E.

The AFM scans for MBE sample set 4 are shown in Figure 48. MBE sample H exhibits many small pits on the surface with a few larger pits microns in area and hundreds of nanometers deep. A clear cross-hatch pattern indicating many dislocations is visible in the 30 µm x 30 µm AFM scan for MBE sample I in

Figure 48b. Sample I has a SL0-substrate mismatch that is three times that of sample H, but sample H has a SL0 FWHM twice that of sample I.

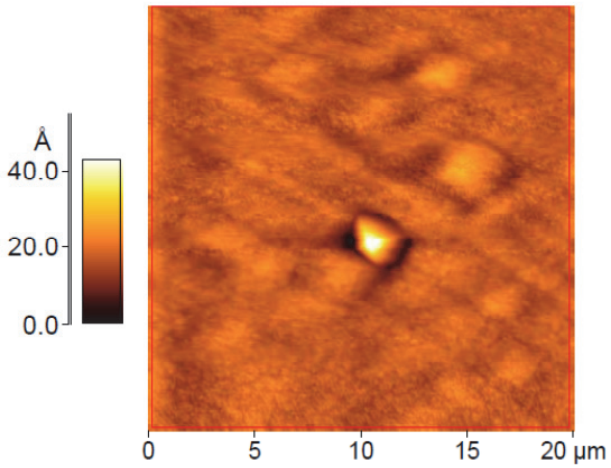

Figure 47. 20 µm x 20 µm AFM scan for MBE sample E. The area RMS roughness is 2.7 Å. **Image acquired by Lawrence Grazulis at the AFRL/RXPS.*

The AFM scans for MBE sample set 5 were measured at IQE, Inc., and the results are shown in Table 17, indicating atomically flat surfaces for MBE samples J – Q, while sample R is significantly rougher due to the ~2µm thick SL.

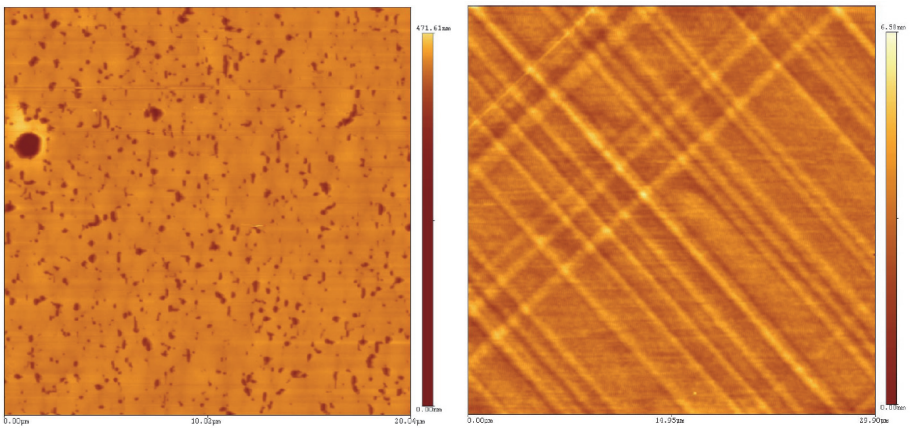

(a) (b)

Figure 48. AFM scans for MBE sample set 4. (a) 20 um x 20 um scan of MBE sample H. The height scale bar is 0 - 471 nm. (b) 30 um x 30 um scan of MBE sample I. The height scale bar is 0 - 7 nm. **Images acquired by Lawrence Grazulis at the AFEL/RXPS.*

Table 17. AFM scan results for MBE sample set 5.

Sample Set 5	x ± 0.01	Period ± 0.5 (nm)	Number of Periods	Area RMS roughness 5 μm x 5 μm (Å)	Area RMS roughness 20 μm x 20 μm (Å)
J (2301027)	0.34	8.48	58	2.0	2.1
K (2301029)	0.37	8.40	58	1.7	1.9
L (2301030)	0.39	8.62	58	1.6	1.5
M (2301031)	0.35	10.72	47	1.8	1.6
N (2301032)	0.35	9.49	52	1.2	1.5
O (2301033)	0.28	24.47	20	2.3	2.7
P (2301043)	0.41	7.30	69	1.5	1.8
Q (2301044)	0.30	17.95	28	1.4	1.6
R (2301060)	0.35	9.79	209	34.5	43.5

4.2.3 Transmission Electron Microscopy

Out of MBE sample set 2, TEM images are only available for MBE samples B and C. The images for MBE sample B show dislocations originating at the substrate/buffer interface, within the buffer layer, and within the SL layers. The TEM image of MBE sample C, shown in Figure 49, is free of dislocations, so

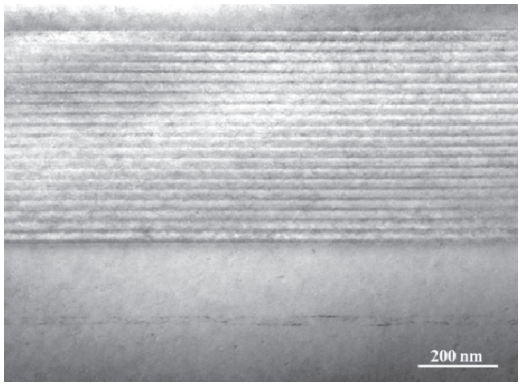

Figure 49. TEM image of MBE sample C. The GaSb substrate is at the bottom, and the GaSb cap layer is shown at the top of the image. **Image acquired by Lu Ouyang and Dr. David Smith at ASU.*

the defect density is much smaller in this sample than in sample B. This corresponds with the XRD result of sample C having lower mismatch than sample B. The high-resolution lattice image of sample C revealed the InAsSb-on-InAs

interface is more abrupt than the InAs-on-InAsSb interface [89], most likely due to Sb segregation during growth [33, 90]. The gradual interfacial grading could also be responsible for the half-the-SL-period modulation of the SL satellite peaks in the XRD patterns as discussed earlier in Section X-ray diffraction.

The TEM image of the ordered-alloy MBE sample E in Figure 50 clearly shows the modulated InAs/InSb layers in the $InAs_{1-x}Sb_x$ layer. A few defects are visible in other TEM images of this same sample. Figure 51 shows defects similar to vertically-stacked quantum dots throughout the entire SL for MBE

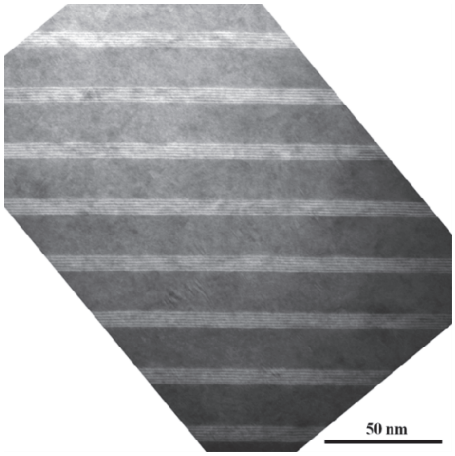

Figure 50. TEM image of MBE sample E clearly showing the six InAs/InSb periods comprising the ordered alloy. **Image acquired by Lu Ouyang and Dr. David Smith at ASU.*

sample F. As the InSb thickness in the modulated alloy was increased to try to increase the Sb composition in the $InAs_{1-x}Sb_x$ layer, the strain built up in the InSb layer until it was released by forming "InSb quantum dots," which then propagated throughout the rest of the SL periods. The InAs/InSb ordered layers were visible for just the first SL period in another TEM image, but the $InAs_{1-x}Sb_x$ layer looked like a conventional alloy in the rest of the SL periods. (111) stacking

faults were also observed in MBE sample F. The presence of these defects explains the broadened XRD SL satellite peaks.

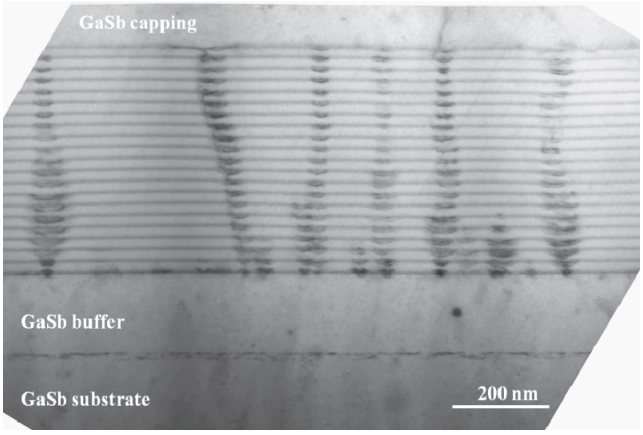

Figure 51. TEM image of MBE sample F showing stacked defects throughout the 20-period SL. **Image acquired by Lu Ouyang and Dr. David Smith at ASU.*

A representative TEM image from sample set 5 of MBE sample J is shown in Figure 52. The image revealed excellent sample qualities with no dislocations visible in the low-magnification image. The 8.3 nm period determined from the TEM agrees well with the 8.5 nm period determined by XRD.

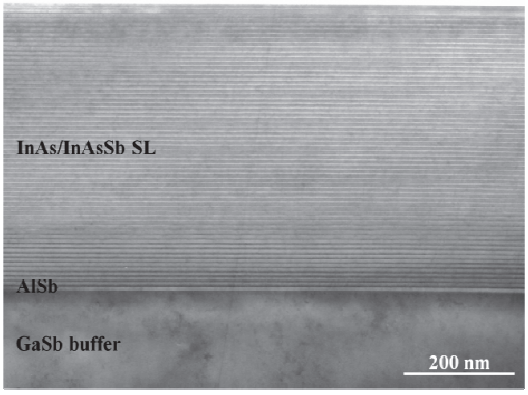

Figure 52. TEM image of MBE sample J showing the entire structure without dislocations. **Image acquired by Lu Ouyang and Dr. David Smith at ASU.*

MBE sample set 5 had the best structural properties out of sets 2-5. MBE sample set 2 had improving mismatches, but the AFM RMS roughness was twice

that of most samples in set 5. Set 3 had ordered $InAs_{1-x}Sb_x$ alloys with increasing InSb layer thicknesses resulting in broad XRD SL satellite peaks and vertically-stacked defects shown in the TEM for the second sample in the set. The fourth MBE sample set had significantly larger mismatches than the other sets, and the AFM revealed pits and cross-hatch for the two samples. MBE sample set 5 is the most promising set for high quality material.

4.2.4 Photoluminescence

PL measurements for MBE sample sets 2-4 were done at 5 K using a double-modulation technique (discussed in Section 5.1) with a Fourier transform infrared spectrometer and a 532 nm laser at 105 W/cm^2 modulated at 60 kHz. Due to the 100 nm GaSb cap layer on MBE sample sets 2 and 3 being approximately five penetration depths of the 532 nm laser wavelength in GaSb, the GaSb cap layer was etched off with 319 photoresist developer prior to the PL measurements. PL results for MBE samples A, B, C, and H are shown in Figure 53 with the symbols representing the data and the solid lines an 8-point adjacent-average smoothing of the data. Gaussian fits were applied, and the peak positions and FWHMs are shown in Table 18. PL from sample D was not measurable. LWIR samples A, B, and C having similar periods confirm the expected trend of longer wavelength transitions for increasing Sb compositions in the SL. Sample H, with a significantly shorter period, results in MWIR emission that is more intense than the LWIR samples' emission due to the much higher wave function overlap and the AlSb electron barriers. The agreement between the calculated SL bandgap and the PL peaks is quite remarkable given the uncertainty in the measured Sb

compositions and periods. The 14-18 meV FWHMs for samples A, B, and C correspond well with the 15-20 meV calculated bandgap shift results for a ± 0.01

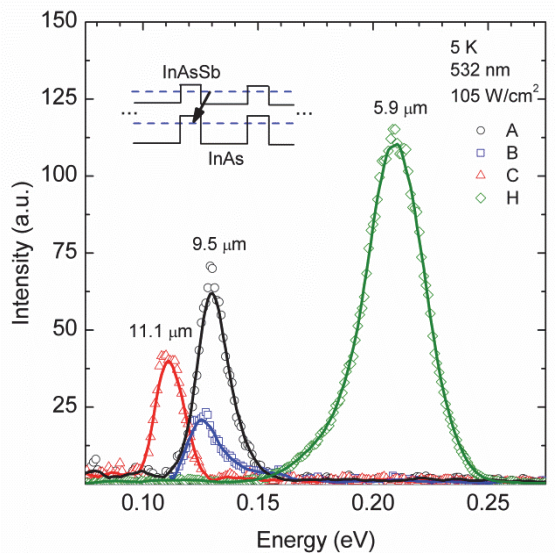

Figure 53. Low temperature PL for MBE samples A, B, C, and H. **Data acquired at AFRL/RXPS.*

change in *x*, whereas the layer thickness fluctuation barely affects the calculated bandgap due to the large SL period. Sample H, however, with a much smaller period and a 33 meV FWHM, experiences a ~30 meV bandgap shift for a ± 1

Table 18. Summary of PL results for MBE sample set 1 and MBE sample H.

Sample	x ± 0.01	Period ± 0.5 (nm)	Number of Periods	Calculated $\left\|\int \Psi_{hh}^{*}\Psi_{e}dz\right\|^{2}$ (%)	Calculated bandgap at 0 K (meV, μm)	PL peak at 5 K (meV, μm)	PL peak FWHM (meV)
A (0203-1)	0.27	26.5	20	6.1	128, 9.7	130, 9.5	18
B (0218-1)	0.28	24.6	20	7.0	120, 10.4	125, 9.9	17
C (0218-2)	0.29	24.6	20	6.6	107, 11.6	112, 11.1	14
D (0218-3)	0.33	24.5	20	5.6	72, 17.1	-	-
H (0512-1)	0.30	7.4	60	45.2	218, 5.7	209, 5.9	33

monolayer $InAs_{1-x}Sb_x$ thickness change but only ~15 meV for ± 0.01 change in *x*. The PL peak FWHMs also follow the same tendency as the XRD average SL mismatch, a wider FWHM for a larger mismatch, demonstrating the correlation between strain-balancing and the SL material quality. Thus, strain-balancing is extremely important to avoid dislocations and achieve device quality SL materials.

PL signals from MBE sample set 3 were not measurable. MBE sample I in set 4 demonstrated multiple features on what appeared to be a larger PL peak, as shown in Figure 54a, before being corrected for the transmission of the diamond cryostat window in the AFRL/RXPS PL setup. The diamond window

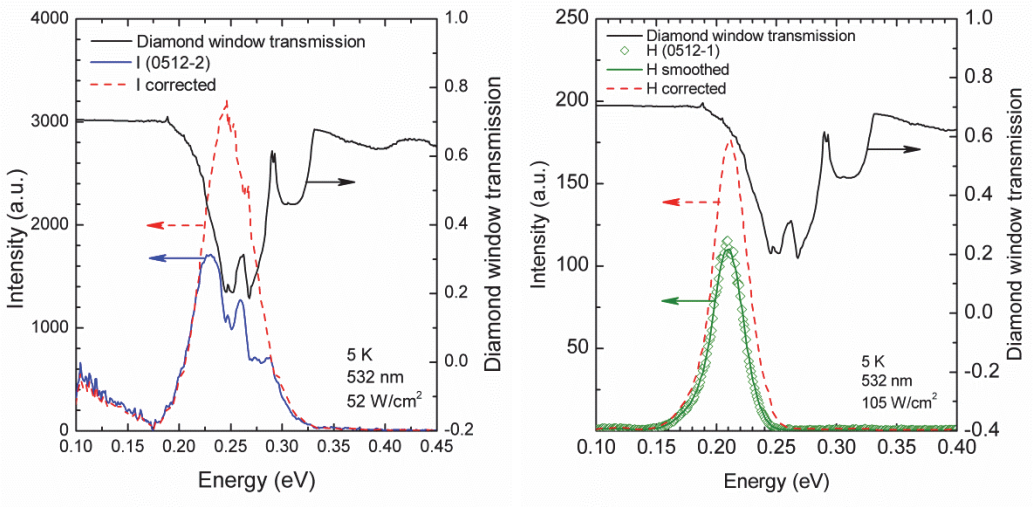

(a) (b)

Figure 54. PL measurements for MBE sample set 4 corrected for the AFRL/RXPS cryostat diamond window transmission: a) sample I (lock-in time constant τ = 1 ms) and b) sample H (lock-in time constant τ = 100 μs). **Data acquired at AFRL/RXPS.*

transmission was measured in the same FTIR used for photoconductance measurements using an CsI beam splitter, and the transmission is very flat at 70% from 7 μm to 25 μm, but from 2.5 μm to 6.5 μm there are several features as

shown in Figure 54. The PL peak position for sample I is at 5 μm, where its shape and intensity are greatly affected by the diamond window transmission spectrum, but the PL peak for sample H at 5.9 μm only has its intensity minimally affected, as shown in Figure 54b. The increasing signal in Figure 54a from 0.17 eV to 0.10 eV is an artifact due to the lock-in amplifier time constant being too long (1 ms) [91]. Using the same parameters used for the calculated results shown in Table 18 for MBE sample set 1, the calculated SL bandgap for sample I is 332 meV (3.7 μm), and the measured PL peak is at 247 meV (5.0 μm) with a FWHM of 50 meV. The FWHM is considerably larger than any of the samples listed in Table 18. Relaxation, as demonstrated by the cross-hatch pattern in the AFM scan, and uncertainty in the layer thicknesses are the reasons for the discrepancy between the calculation and the experimental values.

Table 19. PL peak location results for MBE sample set 5.
* *Measured by Dr. Oray Orkun Cellek at ASU.*

Sample Set 5	x ± 0.01	Period ± 0.5 (nm)	Number of Periods	PL peak location (μm)
J (2301027)	0.34	8.48	58	5.07
K (2301029)	0.37	8.40	58	5.37
L (2301030)	0.39	8.62	58	5.67
M (2301031)	0.35	10.72	47	6.20
N (2301032)	0.35	9.49	52	5.78
O (2301033)	0.28	24.47	20	7.72
P (2301043)	0.41	7.30	69	5.22
Q (2301044)	0.30	17.95	28	7.23
R (2301060)	0.35	9.79	209	5.89

The samples in MBE sample set 5 were designed to have 10 μm bandgaps using the same calculation parameters as above for the results in Table 18, but initial PL measurements performed at ASU by Dr. Orkun Cellek on the samples at 12 K using a 780 nm laser diode modulated at 50 kHz revealed the bandgaps are

in the MWIR from 5 μm to 8 μm. The PL results are listed in Table 19 for MBE sample set 5. The discrepancy between the design and the PL results are discussed in Chapter 5.

MBE samples K and O were also measured at AFRL/RXPS with the 532 nm laser. Figure 55 shows the intensity-dependent 4 K PL results for MBE sample K after the diamond window transmission correction was applied.

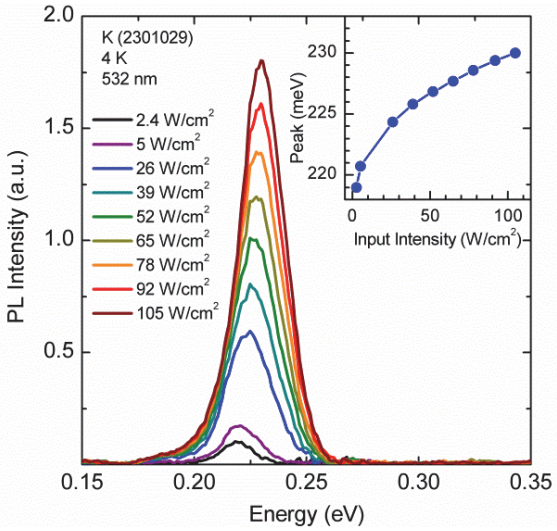

Figure 55. Intensity-dependent PL for MBE sample K. **Data acquired at AFRL/RXPS.*

The measurement resolution is 8 cm^{-1} or ~1 meV. The lowest intensity peak is at 219 meV and the highest intensity peak is at 230 meV, an 11 meV change in the given intensity range (~2 decades). The PL peak position versus incident intensity, illustrating the SL miniband filling, is shown in the inset of Figure 55. The low energy side of the peaks remaining fixed while the high energy side increases in energy with the pumping intensity. The opposite is seen for an increase in temperature: the high energy side of the PL peak is fixed while the low energy side decreases in energy with increasing temperature (See Figure

56). This is due to the temperature changing the SL bandgap and thus the absorption edge.

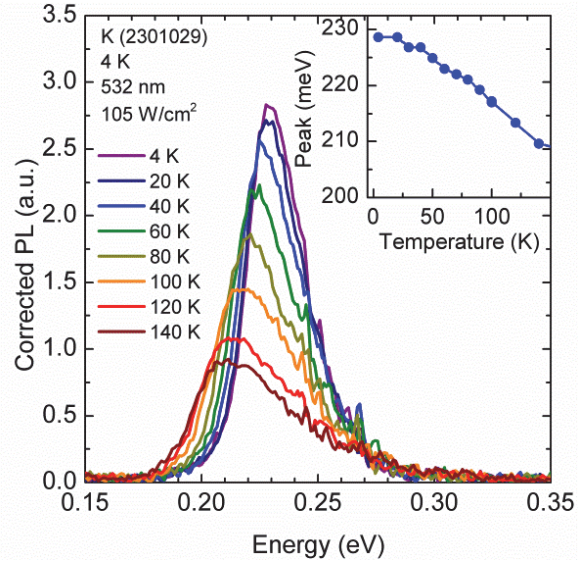

Figure 56. Temperature-dependent PL for MBE sample K. **Data acquired at AFRL/RXPS.*

The temperature-dependent PL results for sample O are shown in Figure 57 along with the Varshni and Fan fits. The Fan fit is excellent at low temperatures, while the Varshni fit is not as good.

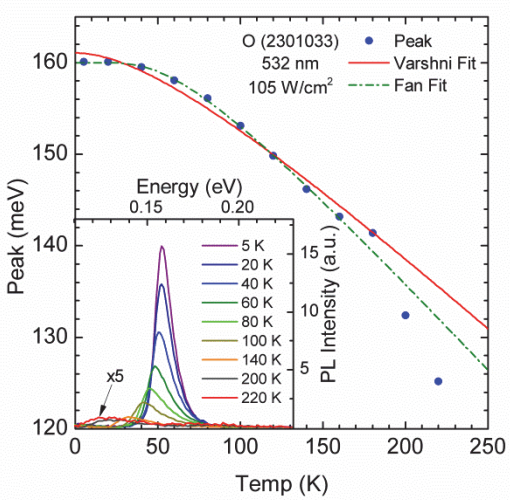

Figure 57. Temperature-dependent PL for MBE sample O. **Data acquired at AFRL/RXPS.*

Temperature-dependent PL results available for certain samples in MBE set 5 are summarized in Table 20, Table 21, and Table 22. See Section Photoconductance for definitions of the following parameters. The Varshni α parameter for the SLs is less than the corresponding parameter for InAs and InSb,

Table 20. Results for the Varshni equation fit to the temperature-dependent PL.

Varshni Fit Results				
Sample	$E_g(0)$ meV	α eV/K	β (K)	Temp. range (K)
InAs		2.76×10^{-4}	93	
InSb		3.20×10^{-4}	170	
MOCVD A	177	$2.75 \pm 0.28 \times 10^{-4}$	139 ± 34	10 – 200
MBE K	229	$2.42 \pm 0.3 \times 10^{-4}$	106 ± 31	5 – 150
MBE O	161	$1.67 \pm 0.06 \times 10^{-4}$	95.8 ± 8.2	5 – 140

indicating the SL bandgaps are less sensitive to changes in temperature than the bulk materials. The Varshni β parameter is between that of InAs and InSb and increases with the SL bandgap for these two samples. The Fan parameters in Table 21 are very similar between the SLs except that the average phonon energy of sample K is half that of sample O and closer to that of InSb than InAs. Sample K has 37% Sb in the $InAs_{1-x}Sb_x$ layer as opposed to 28% for sample O. The Debye temperatures of the SLs are less than those of InAs and InSb, agreeing with the SL bandgap being less sensitive to temperature than the bulk materials.

Table 21. Results for the Fan equation fit to the temperature-dependent PL.

Fan Fit			
Sample	$E_g(0)$ meV	A meV	$\langle E_p \rangle$ meV
InAs		44, 20	16, 13
InSb [66]		26.5, 37.6	9.6, 12.5
MOCVD A	177	27.1 ± 3.6	10.7 ± 1.1
MBE K	228.5 ± 0.3	16.3 ± 3.1	7.6 ± 1.1
MBE O	160.0 ± 0.1	35.7 ± 2.8	15.6 ± 0.7

Table 22. Summary of the relationships between the Debye temperature, Varsnhi, and Fan parameters for one MOCVD and two MBE samples.

Sample	$\Theta_D = \langle E_p \rangle / k$ (K)	α' (eV/K)	A/α' (K)	β (K)
InAs	247			93
InSb	206			170
MOCVD A	124	2.1×10^{-4}	131	139 ± 34
MBE K	88	1.9×10^{-4}	86	106 ± 31
MBE O	181	2.2×10^{-4}	162	95.8 ± 8.2

In summary, the PL results for MBE sample set 2 agree very well with the designed bandgaps for the SL structures. MBE sample set 3 did not give measureable PL signals, and MBE sample set 4 PL results were different from the calculated values. The MWIR PL results for MBE sample set 5 are far from the designed 10 μm bandgaps. This discrepancy is explained next in Chapter 5.

Overall, the MBE SL samples were better quality than the MOCVD samples, with variations in the MBE sample sets due to growth in different MBE machines. The highest quality set of samples was MBE sample set 5 grown by IQE with bandgaps covering 5 – 8 μm. Therefore, this set of samples is used in the following two chapters for studies of the InAs/$InAs_{1-x}Sb_x$ valence band offsets (Chapter 5) and the InAs/$InAs_{1-x}Sb_x$ SL minority carrier lifetimes (Chapter 6).

5. DETERMINATION OF THE InAs/$InAs_{1-x}Sb_x$ VALENCE BAND OFFSET

InAs/$InAs_{1-x}Sb_x$ strain-balanced SLs on GaSb are a viable alternative to the well-studied InAs/$Ga_{1-x}In_xSb$ SLs for mid- and long-wavelength infrared (MWIR and LWIR) laser and photodetector applications, but the InAs/$InAs_{1-x}Sb_x$ SLs are not as thoroughly investigated. Therefore, the valence band offset between InAs and $InAs_{1-x}Sb_x$, a critical parameter necessary to predict the SL bandgap, must be further examined to produce InAs/$InAs_{1-x}Sb_x$ SLs for devices operational at MWIR and LWIR wavelengths. The effective bandgap energies of InAs/$InAs_{1-x}Sb_x$ SLs with x = 0.28 – 0.40 were designed using the three-band envelope function approximation model described in Section Three-band model with E_{v_InAs} = -0.59 eV, E_{v_InSb} = 0, C_{Eg_InAsSb} = 0.67 eV, and C_{Ev_InAsSb} = 65%·C_{Eg_InAsSb} based on the literature search. Multiple ~0.5 μm-thick SL samples were grown by molecular beam epitaxy on GaSb substrates, as described in Chapter 4 for MBE sample set 5. Structural characterization using x-ray diffraction and atomic force microscopy revealed excellent crystalline properties with SL zero-order peak full-width-half-maximums between 30 and 40 arcsec and 20 x 20 μm^2 area root-mean-square roughness of 1.6 - 2.7 Å as discussed in Sections 4.2.1 and 4.2.2. Photoluminescence (PL) spectra of these samples cover 5 to 8 μm as noted in Table 19, and the band offset between InAs and $InAs_{1-x}Sb_x$ was obtained by fitting the calculated values to the experimental PL peaks.

5.1 Infrared photoluminescence experiment

Three methods for measuring IR PL have been compared: conventional PL, frame-to-frame subtraction, and double-modulation [92]. The term double-modulation comes from the input pump laser being chopped in addition to the slowly varying FTIR modulation of the PL signal, and the frame-to-frame subtraction method subtracted the background spectra taken while the mirror traveled back to its zero path difference position from the signal spectra taken while the mirror traveled away from the zero path difference position. The double-modulation technique had a higher signal-to-noise ratio than the frame-to-frame subtraction method, and the PL signal was difficult to discern amongst the background when using the conventional PL method. The double-modulation technique was recommended [92]; however, the data acquisition time is the longest of all the techniques due to it using the slowest mirror speed. The slower mirror velocity allows the noise bandwidth to be decreased due to the availability of larger time constants for the lock-in output low pass filter [92].

The PL spectra for this study were taken using the double-modulation technique with a Fourier transform infrared (FTIR) spectrometer to suppress the background signal from room temperature (~300 K) blackbody radiation. Figure 58 shows the calculated 300 K blackbody radiation (W/cm^2) curve given by [93]

$$S(\lambda) = \frac{2\pi hc^2}{\lambda^5} \frac{1}{e^{\frac{hc}{\lambda kT}} - 1}, \tag{96}$$

which peaks at approximately 10 μm and adds significant background to PL signals above 5 μm until the 12 μm HgCdTe detector cutoff. Also shown in Figure 58 are the background signal and the PL signal from MBE sample A when

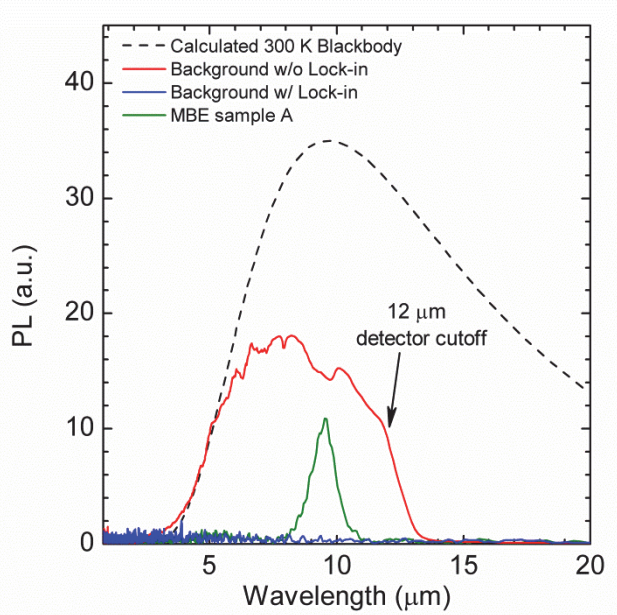

Figure 58. The photoluminescence setup background signal with and without using a lock-in amplifier, a 300 K blackbody curve, and an actual PL signal for MBE sample A. **Data acquired at AFRL/RXPS.*

a lock-in amplifier has been added to the setup and the pumping laser has been chopped at 60 kHz. Clearly, the background signal has been suppressed. Such a large background signal disguises the actual sample PL signal and makes the measurement interpretation much more difficult, as demonstrated in Figure 59.

The FTIR is based on a two-beam Michelson interferometer with one moving, or scanning, mirror. A schematic of the interferometer is shown in Figure 60 [94]. The incident beam is split into two coherent beams at the beam splitter with one beam traveling a fixed path length while the other travels a varying path length based on the mirror speed. When the beams recombine at the beam splitter and travel to the detector, they interfere according to the phase

change introduced by the optical path length difference. Since different wavelength light interferes constructively at different optical path length differences, the spectral information in a light beam can be extracted from the detector signal versus the mirror position [94].

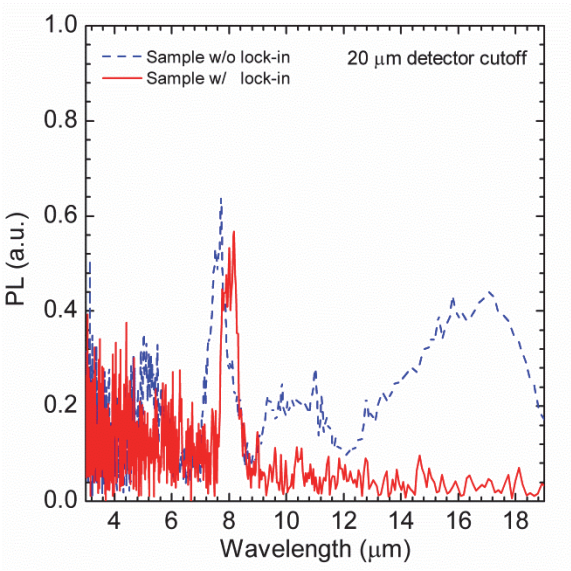

Figure 59. Photoluminescence of an 8 μm SL sample with and without the lock-in amplifier showing the signal distortion due to the background 300 K blackbody radiation. **Data acquired at AFRL/RXPS.*

The optical path length difference, δ, is also called the retardation and for constructive interference is given by

$$\delta = n\pi, \tag{97}$$

where n is an integer. The detector signal can be written for a single frequency as [94]

$$S(\delta) = \frac{1}{2} I_o(k_o)[1 + \cos(2\pi\delta k_o)], \tag{98}$$

were I_o is the incident beam intensity with wavelength λ_o and $k_o = 1/\lambda_o$ is the wave number with units cm^{-1}. The modulated part of the signal [94],

$$S_{ac}(\delta) = B(k_o)\cos(2\pi\delta k_o), \tag{99}$$

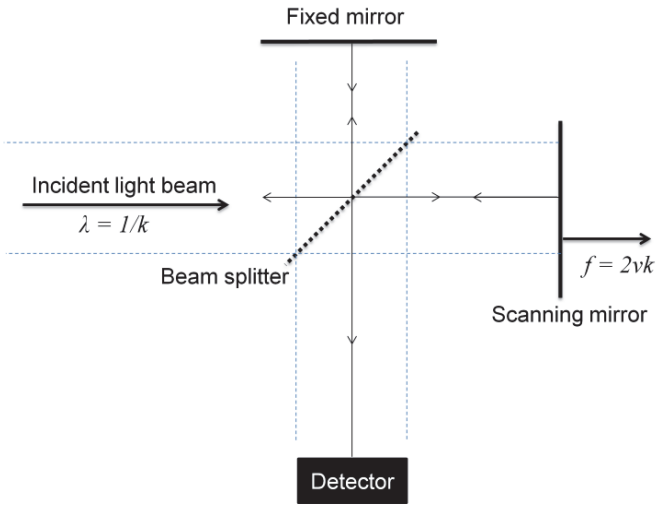

Figure 60. Schematic diagram of the Michelson interferometer used in the FTIR spectrometer [94].

is called the interferogram. Equation (99) gives $S_{ac}(\delta)$ as the mathematical form of the Fourier cosine transform, which is the real part of the Fourier transform, of $B(k_o)$ [94]. Therefore, by taking the inverse Fourier transform of the measured $S_{ac}(\delta)$, the spectral information in the incident beam can be recovered. A block diagram of the FTIR PL measurement is shown in Figure 61.

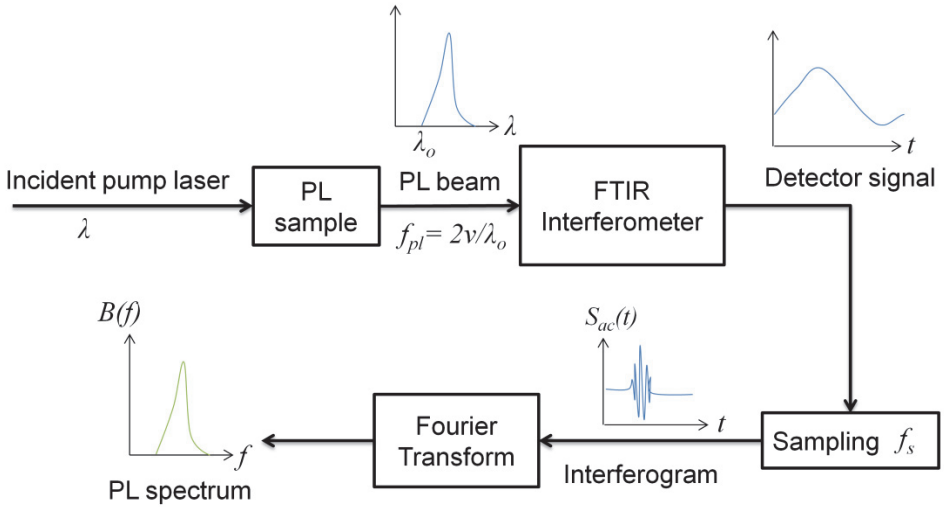

Figure 61. Block diagram of the FTIR PL measurement.

The interferogram is actually measured with respect to time rather than retardation, so the optical path length difference must be converted to time using the constant mirror velocity, v, [94]

$$\delta = 2vt, \tag{100}$$

$$S_{ac}(t) = B(k_o)\cos(2\pi k_o 2vt) \rightarrow B(f)\cos(2\pi ft), \tag{101}$$

$$f = 2vk_o = \frac{2v}{\lambda_o}. \tag{102}$$

The first modulation of the λ_o PL signal has a frequency given by Eq. (102), and to add the second modulation needed to reduce the background, the sampling frequencies must be considered. Nyquist's sampling theorem says the sampling frequency must be at least twice (although ten times is more practical) the highest frequency in the signal in order to avoid distorting the signal [94]. The FTIR triggers sampling of the detector signal to create the interferogram at either a positive or negative going zero crossing of a HeNe laser reference signal, resulting in the FTIR sampling frequency

$$f_s = \frac{2v}{0.6328 \cdot 10^{-4} cm}. \tag{103}$$

For a mirror speed of 0.10 cm/s, the sampling frequency is 3.16 kHz, and incident beams with wavelengths longer than 1.27 μm can be sampled without distortion. Increasing the mirror speed decreases the wavelengths that can be sampled properly, and correspondingly, decreasing the mirror speed increases the wavelength limit. A PL beam with expected wavelengths longer than 5 μm measured with an FTIR mirror velocity of 0.05 cm/s contains FTIR modulated frequencies less than 200 Hz. The sampling frequency at this mirror speed is

eight times the frequency of the shortest wavelength in the PL beam. The highest FTIR modulated frequency in the PL beam is given by the shortest wavelength as

$$f_{pl} = \frac{2v}{\lambda_o}, \tag{104}$$

and ideally the sampling frequency should be ten times greater than the modulated PL frequency

$$f_s \geq 10 f_{pl}. \tag{105}$$

To successfully add the double modulation to the FTIR PL measurement, the addition of chopping the pump laser beam and the lock-in amplifier must be seamless to the FTIR sampling and Fourier transform electronics. This requires the chopping frequency to be

$$f_{ch} \geq 10 f_s, \tag{106}$$

and the lock-in amplifier low pass filter 3dB frequency and time constant

$$f_s \leq f_{3dB} \geq 10 f_{pl}, \tag{107}$$

$$\tau = \frac{1}{2\pi f_{3dB}}, \tag{108}$$

in order to reproduce the PL signal before the inverse Fourier transform is performed. Increasing the lock-in time constant can result in the low pass filter removing some shorter wavelength components of the PL spectrum, thus distorting the actual spectrum, despite higher time constants resulting in smoother signals. Increasing the number of FTIR scans that are coadded is a better way to reduce the noise since to the signal to noise ratio is also proportional to the square root of the number of scans. Combining all the frequency requirements together gives [91]

$$0.1f_{ch} \geq \frac{1}{2\pi\tau} \geq 10f_{pl}, and \tag{109}$$

$$0.1f_{ch} \geq f_s \leq f_{3dB} \tag{110}$$

The example above for the PL spectrum with wavelengths greater than 5 μm results in f_s = 1567 Hz and requires $\tau \leq$ 80 μs and f_{ch} > 20 kHz. The block diagram of the double-modulation technique is shown in Figure 62.

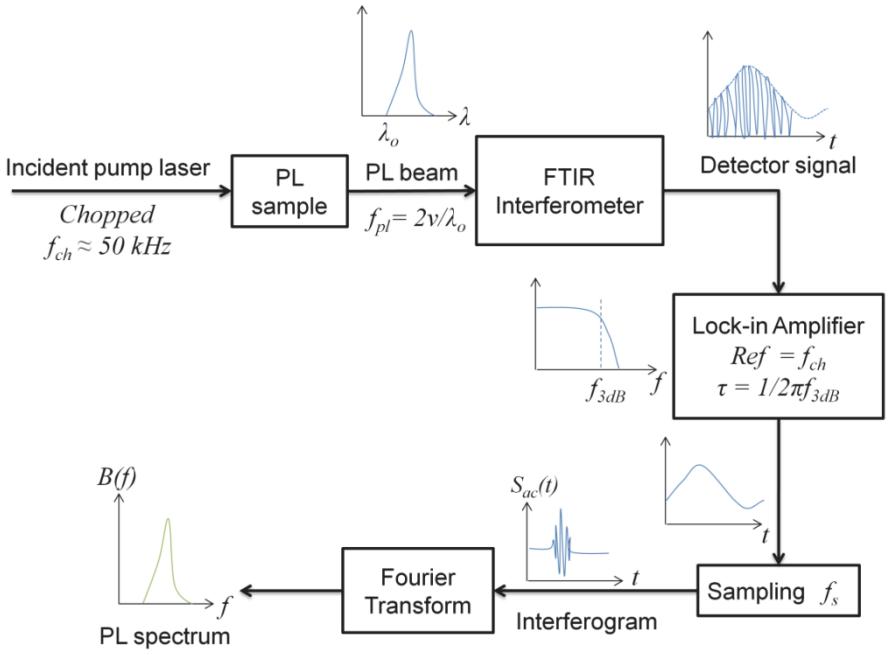

Figure 62. Block diagram of the double-modulation technique for the FTIR PL measurement.

The measured spectrum is actually the result of the convolution of the Fourier transform of the real spectrum and the Fourier transform of an instrumental line shape function, which is nominally a sinc function from the Fourier transform of a rectangular (or boxcar) function arising from the limited mirror path length and thus limited range of the interferogram [94]. This sinc function causes unwanted side lobes to appear in the transformed spectrum. Suppression of the side lobes is defined as apodization and is accomplished with

apodization functions [94]. The apodization function is unity at the zero path difference and decays to zero in some manner at the maximum path difference. The choice of apodization function affects narrow spectral signals more significantly due to greater signal content at larger path length differences or retardations. A signal with broad spectral content produces an interferogram that decays quickly as the path length difference increases, making it less sensitive to the apodization function [94]. The PL setup at AFRL/RXPS used the Bartlett apodization function, which is a triangle function, and only results in side lobes on the higher wave number side of a peak since the Fourier transform of the triangle function is a sinc^2 function.

The double-modulation FTIR PL setup used at AFRL\RXPS consisted of a Bomem DA3 FTIR spectrometer, a closed-cycle helium cryostat capable of reaching 4 K with a diamond window, a 532 nm continuous-wave laser with a maximum output of 2.2 W, an electro-optical modulator tuned to 532 nm for chopping the laser beam at 60 kHz, and liquid-nitrogen cooled HgCdTe detectors with cutoff wavelengths of either 12 μm or 20 μm.

For this band offset study, the samples were measured at ASU and were kept at 12 K in a closed-cycle helium cryostat with a ZnSe window and were optically excited with a 780 nm laser diode modulated at 50 kHz with an average power density on the order of ~10 W/cm^2. The FTIR scan speed was 0.15 cm/s, and the time constant was 30 μs, giving: f_{pl} = 600 Hz, f_s = 4740 Hz ($8f_{pl}$), f_{3dB} = 5305 Hz ($8.8f_{pl}$), f_{ch}= $10.5f_s$, f_{ch} = 9.4 f_{3dB}, $f_{3dB} > f_s$, which meet all of the requirements given above.

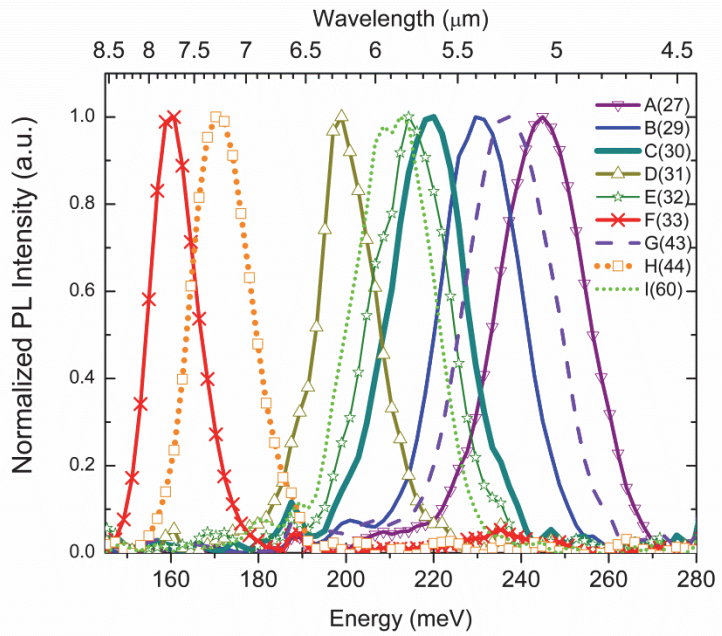

Figure 63. Normalized 12 K photoluminescence spectra of the MBE sample set 5: InAs/InAs$_{1-x}$Sb$_x$ SL samples with x = 0.28 – 0.40. **Data acquired by Dr. Oray Orkun Cellek at ASU.*

The PL signal was collected with gold-coated parabolic mirrors and analyzed with an FTIR system equipped with a 15 μm cut-off HgCdTe photodetector. The normalized PL spectra of the samples are shown in Figure 63 and the peak wavelengths range from 5.1 μm to 7.7 μm.

5.2 Modeling the superlattice photoluminescence results

The three-band model was used to determine the band offsets by calculating the SL bandgap that agreed with the experimental PL peak energies. The difference between the model's bandgap and the PL peak was minimized using the Matlab function fmincon [95]. The model allowed for the possibility of both type-II alignments and type-I by adjusting the material parameters of the quantum wells and barriers accordingly. If the layers were too thin to have a quantum confined electron energy level, the top of the higher conduction band

was used as the electron level which results in smaller errors than if the free electron levels were used. In fact, only samples O and Q with the largest periods have confined electron levels when the type-IIa alignment is used. The parameter C_{Ev_InAsSb} in Eq. (29) was fit for a selection of InAs/InSb valence band offsets listed in Appendix B (E_{v_InSb} = 0 eV; E_{v_InAs} = -0.43, -0.50, -0.59, -0.61 eV) and two $InAs_{1-x}Sb_x$ bandgap bowing constants (C_{Eg_InAsSb} = 0.67 eV [45], 0.80 eV [38]). Assuming C_{Ev_InAsSb} is constant over the Sb composition range of the present samples, the calculated C_{Ev_InAsSb} parameter for the entire set of samples and the error defined as $\sqrt{[\Sigma(E_{g\_Calc} - E_{PL})^2/N]}$ are shown in Table 23.

Table 23. Results for C_{Ev_InAsSb} from fitting the experimental photoluminescence data for the InAs/$InAs_{1-x}Sb_x$ SL MBE sample set 5.

InAs/InSb valence band offset (eV)	$C_{Eg\ InAsSb}$ = 0.67 eV		$C_{Eg\ InAsSb}$ = 0.8 eV	
	C_{Ev_InAsSb} (eV)	Error (eV)	C_{Ev_InAsSb} (eV)	Error (eV)
0.43	-0.320	0.008	-0.286	0.009
0.50	-0.214	0.009	-0.181	0.010
0.59	-0.076	0.010	-0.042	0.011
0.61	-0.045	0.010	-0.012	0.011

The negative values for C_{Ev_InAsSb} indicate a type-IIb alignment between InAs and $InAs_{1-x}Sb_x$ rather than a type-IIa alignment, and the magnitude of C_{Ev_InAsSb} decreases while the error for the fit to the sample set increases slightly as the InAs/InSb valence band offset increases. The same trends are followed for both C_{Eg_InAsSb} values. If an InAs/InSb valence band offset of 0.61 eV is used with an $InAs_{1-x}Sb_x$ bandgap bowing parameter of 0.8 eV, a linear interpolation of the $InAs_{1-x}Sb_x$ valence band edge between the InAs and InSb valence band edges is a good fit since the results show only 1.2% of the $InAs_{1-x}Sb_x$ bandgap bowing in the valence band. However, if an InAs/InSb valence band offset of 0.50 eV is used

with an $InAs_{1-x}Sb_x$ bandgap bowing parameter of 0.67 eV, the results show 21.4% of the $InAs_{1-x}Sb_x$ bandgap bowing should be attributed to the valence band. Therefore, the initial assumed InAs/InSb valence band offset in the model greatly affects the amount of bandgap bowing attributed to the $InAs_{1-x}Sb_x$ valence band edge for this sample set.

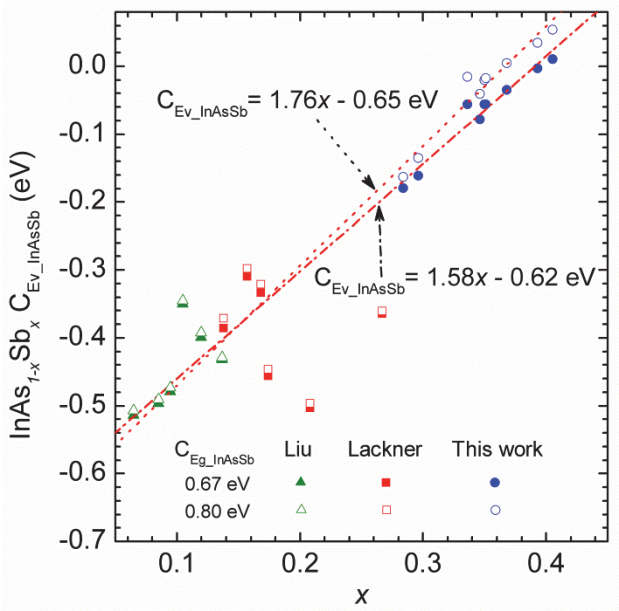

Figure 64. The calculated $InAs_{1-x}Sb_x$ bandgap bowing attributed to the valence band for C_{Eg_InAsSb} = 0.67 eV (solid symbols) and for C_{Eg_InAsSb} = 0.80 eV (open symbols) for the samples studied here and two sets of samples from Refs [50] and [22]. The model used E_{v_InAs} = -0.59 eV and E_{v_InSb} = 0 eV.

Over the range of x values studied here, C_{Ev_InAsSb} varies linearly with x, when fitting the PL peak of each sample individually, as shown in Figure 64 for both C_{Eg_InAsSb} = 0.67 eV (solid symbols) and 0.80 eV (open symbols). The magnitude of C_{Ev_InAsSb} decreases as x increases. The C_{Ev_InAsSb} values fit using C_{Eg_InAsSb} = 0.80 eV (open symbols) are slightly larger than those fit using C_{Eg_InAsSb} = 0.67 eV (solid symbols) with the discrepancy increasing as x increases. The linear fits to C_{Ev_InAsSb} for the sample set studied here are shown

extended to x = 0.05 in Figure 64 for C_{Eg_InAsSb} = 0.67 eV (C_{Ev_InAsSb} = 1.58x - 0.62 eV as a dash-dot line) and for C_{Eg_InAsSb} = 0.80 eV (C_{Ev_bowing} = 1.76x - 0.65 eV as a dotted line). Also plotted are the calculated C_{Ev_InAsSb} values for two sets of sample structures from the literature: MBE-grown structures on InAs substrates from Liu, *et al.* [50] and MOCVD-grown structures on GaSb substrates from Lackner, *et al.* [22]. Although there is more spread in the Liu and Lackner data, the C_{Ev_InAsSb} values lie reasonably along the line calculated for the data from MBE sample set 5.

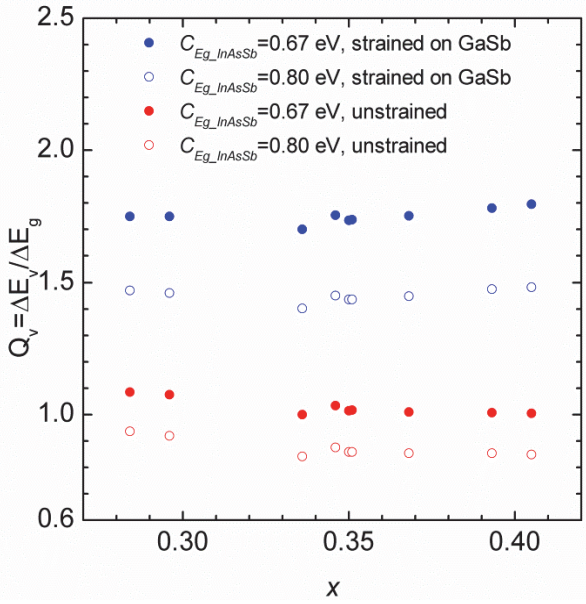

Figure 65. The InAs/InAs$_{1-x}$Sb$_x$ fractional valence band offset, Q_v, versus x for C_{Eg_InAsSb} = 0.67 eV (solid symbols) and for C_{Eg_InAsSb} = 0.80 eV (open symbols) for MBE sample set 5.

The fractional valence band offset, Q_v in Eq. (26), between InAs and InAs$_{1-x}$Sb$_x$ unstrained and strained on GaSb resulting from the calculated C_{Ev_InAsSb} values, is shown versus x in Figure 65 for MBE sample set 5 for the cases of C_{Eg_InAsSb} = 0.67 eV (solid symbols) and C_{Eg_InAsSb} = 0.80 eV (open symbols) when E_{v_InAs} = -0.59 eV and E_{v_InSb} = 0 eV. Figure 65 shows Q_v is fairly

constant over the given Sb composition range. The Q_v values for the unstrained case are lower than the strained case due to the shifting of the band edges causing ΔE_v to increase.

Also plotted in Figure 66 are the calculated strained Q_v results for Liu [50] and Lackner's [22] samples. Together, all three sets of samples cover the $InAs_{1-x}Sb_x$ composition range from x = 0.07 to 0.41. The best fitting Q_v values for the three sets are shown in Table 24.

Table 24. Summary of the $InAs/InAs_{1-x}Sb_x$ fractional valence band offset Q_v for three sets of superlattice structures.

Sample Set	Strained Q_v ($\Delta E_v/\Delta E_g$)	
	C_{Eg_InAsSb} = 0.67 eV	C_{Eg_InAsSb} = 0.80 eV
Liu [50]	1.82 ± 0.07	1.54 ± 0.06
Lackner [22]	1.86 ± 0.14	1.57 ± 0.12
This work	1.75 ± 0.03	1.45 ± 0.02

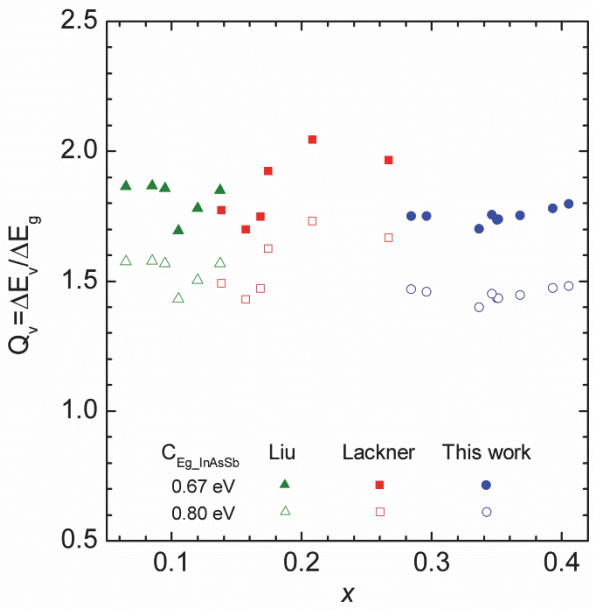

Figure 66. The $InAs/InAs_{1-x}Sb_x$ strained fractional valence band offset, Q_v, vs. x for C_{Eg_InAsSb} = 0.67 eV (solid symbols) and for C_{Eg_InAsSb} = 0.80 eV (open symbols) for the samples studied here and two sets of samples from Refs [50] and [22]. The model used E_{v_InAs} = -0.59 eV and E_{v_InSb} = 0 eV.

The results agree with each other within the error, with the set from this work covering x = 0.28 to 0.41 giving the lowest value and the least variance. The Q_v values for C_{Eg_InAsSb} = 0.80 eV (open symbols) are ~0.30 less than those for C_{Eg_InAsSb} = 0.67 eV (solid symbols). However, the calculated fractional valence band offset is observed to be fairly constant versus x for both values of $InAs_{1-x}Sb_x$ bandgap bowing using the current model for the range of samples studied. Therefore, designing InAs/$InAs_{1-x}Sb_x$ SLs using the Q_v parameter is simpler than using the C_{Ev_InAsSb} parameter. The calculated bowing in the $InAs_{1-x}Sb_x$ valence band and the fractional valence band offset parameter may depend on the growth conditions, causing the variation in the data shown in Figure 64 and in Figure 66 for the samples grown by three different groups.

It should be noted that the model used here assumes abrupt interfaces between the two superlattice layers. In reality, As and Sb segregation and intermixing occur during the SL growth, resulting in compositional grading at the interfaces between the $InAs_{1-x}Sb_x$ and InAs layers. The present calculations do not take any interface grading or layers into account.

5.3 Summary

In summary, PL peak positions for InAs/$InAs_{1-x}Sb_x$ strain-balanced SLs with x = 0.28 – 0.40 grown by MBE on GaSb substrates were used to fit the bowing in the $InAs_{1-x}Sb_x$ valence band and the type-IIb fractional valence band offset, $Q_v = \Delta E_v/\Delta E_g$, using a three-band envelope function approximation model. The bowing in the valence band was found to depend on the initial InAs/InSb valence band offset and varied linearly with x as C_{Ev_InAsSb} = 1.58x - 0.62 eV for

an $InAs_{1-x}Sb_x$ bandgap bowing parameter of 0.67 eV. A fractional valence band offset, $Q_v = \Delta E_v/\Delta E_g$, of 1.75 ± 0.03 was determined when InAs/$InAs_{1-x}Sb_x$ is strained on GaSb and agrees reasonably with other published data for InAs/$InAs_{1-x}Sb_x$ samples with $x = 0.07 – 0.27$. For the samples studied here, $Q_v = 1.03 \pm 0.03$ when unstrained. It is recommended to design InAs/$InAs_{1-x}Sb_x$ superlattice structures using the fractional valence band offset Q_v rather than a fraction of the bandgap bowing in the valence band, C_{Ev_InAsSb}, which is dependent on x.

6. MINORITY CARRIER LIFETIME OF $InAs/InAs_{1-x}Sb_x$ SUPERLATTICES

6.1 Introduction

Time-resolved photoluminescence measurements revealed a minority carrier lifetime of > 412 ns at 77 K under low excitation for a long-wavelength infrared $InAs/InAs_{0.72}Sb_{0.28}$ type-II superlattice (T2SL). This lifetime represents an order-of-magnitude increase in the minority carrier lifetime over previously reported lifetimes in long-wavelength infrared $InAs/Ga_{1-x}In_xSb$ T2SLs. The considerably longer lifetime is attributed to a reduction of non-radiative recombination centers with the removal of Ga from the superlattice structure. This lifetime improvement may enable background limited T2SL long-wavelength infrared photodetectors at higher operating temperatures.

The $InAs/Ga_{1-x}In_xSb$ type-II superlattice (T2SL) is so far the most investigated III-V T2SL material for mid- and long-wavelength infrared (MWIR and LWIR) photodetectors. T2SLs are predicted to have a number of advantages over the currently used bulk HgCdTe, including a decreased dependence of the bandgap on compositional non-uniformity, the ability to leverage III-V manufacturing capabilities, the lower cost of substrates, a higher electron effective mass leading to smaller tunneling currents, and lower Auger recombination rates due to band-engineering and thus lower dark currents [2]. However, reported minority carrier lifetimes at 77 K are 50 – 80 ns for MWIR $InAs/Ga_{1-x}In_xSb$ T2SLs [38, 96] and 10 – 40 ns for LWIR $InAs/Ga_{1-x}In_xSb$ T2SLs [38, 82, 97] as compared to 1 μs for $Hg_{0.78}Cd_{0.22}Te$ (~10 μm bandgap [38]). The short minority

carrier lifetime has been attributed to Shockley-Read-Hall (SRH) recombination and is detrimental to the device dark current and quantum efficiency [83]. Calculations show that a 350-ns lifetime should be reached in order for a LWIR T2SL *pn* homojunction photodiode to achieve background limited operation (BLIP) at 80 K with F/6.5 optics in a 300 K background [97].

Campaigns to improve the minority carrier lifetime have led to investigations of the InAs/$Ga_{1-x}In_xSb$ T2SL interface type [98] and density [84, 99], as well as doping concentration [38, 100], but have thus far resulted in minor or no improvements in the carrier lifetime. It is hypothesized that a native defect associated with InAs or GaSb limits the carrier lifetime [99]. The measured lifetimes of bulk InAs (~325 ns at 77 K) [99], bulk $InAs_{0.80}Sb_{0.20}$ (250 ns at 77 K) [38], and $InAs_{0.875}Sb_{0.125}$ on GaSb (200 ns at 300 K) [101] are longer than that of bulk GaSb (~100 ns) [99], suggesting that defects associated with GaSb and other Ga-related bonds limit the lifetime of InAs/$Ga_{1-x}In_xSb$ T2SLs and that InAs/$InAs_{1-x}Sb_x$ T2SLs should have a longer minority carrier lifetime than InAs/$Ga_{1-x}In_xSb$ T2SLs. Furthermore, InAs/$InAs_{1-x}Sb_x$ T2SLs have been successfully demonstrated for MWIR lasers and proposed for LWIR photodetectors [18, 33]. A theoretical comparison between LWIR InAs/$InAs_{1-x}Sb_x$ and InAs/$Ga_{1-x}In_xSb$ T2SLs, which excludes SRH recombination, found that the ideal detectivities of the two types of T2SL devices are comparable and are both greater than that of HgCdTe devices [19]. This chapter reports an order-of-magnitude improvement of the minority carrier lifetime for LWIR InAs/$InAs_{1-x}Sb_x$ T2SLs over that of LWIR InAs/$Ga_{1-x}In_xSb$ T2SLs. A carrier lifetime of > 412 ns at 77 K under low

excitation was observed for a LWIR InAs/$InAs_{0.72}Sb_{0.28}$ T2SL as determined by time-resolved photoluminescence (TRPL) measurements. This improvement in minority carrier lifetime could enable LWIR T2SL BLIPs to have lower dark current and operate at higher operating temperatures.

6.2 Lifetime theory

Several recombination mechanisms contribute to the minority carrier lifetime in semiconductor devices. The most commonly addressed processes are radiative recombination and non-radiative recombination including Shockley-Read-Hall (SRH) and Auger. Radiative recombination results in photon emission, SRH recombination results in phonon-emission after the electron and hole recombine involving a mid-gap state caused by an impurity or other defect, and Auger recombination also results in phonon-emission from a third carrier that is excited from either the conduction or the valence band edge to a higher energy state in the corresponding band by the energy released from the electron-hole recombination. Each recombination process has a corresponding recombination lifetime, τ, defined in terms of the net recombination rate, R, and excess carrier density, δn,

$$\tau = \frac{\delta n}{R}. \tag{111}$$

The total lifetime is

$$\frac{1}{\tau} = \frac{1}{\tau_{SRH}} + \frac{1}{\tau_{Rad}} + \frac{1}{\tau_{Auger}}. \tag{112}$$

The following analyses assume the semiconductor is non-degenerate, which may not be the case at all temperatures for the SL samples analyzed below.

The net radiative recombination rate in thermal equilibrium without external electrical or optical excitation is

$$R_{rad} = B(np - n_o p_o), \tag{113}$$

where n_o, p_o are the equilibrium carrier concentrations, $n_o p_o = n_i^2$, and B is the radiative or bimolecular recombination coefficient [56]. Under external excitation in steady-state, the carrier concentrations become

$$n = n_o + \delta n, \tag{114}$$

$$p = p_o + \delta p, \tag{115}$$

with δn, δp the excess carrier densities and $\delta n = \delta p$ for band-to-band transitions [56]. The radiative recombination rate with external excitation is then

$$R_{Rad} = B(n_o + p_o + \delta n)\delta n. \tag{116}$$

In the low-level injection case, when Δn, $\Delta p \ll (n_0 + p_o)$, the radiative lifetime is

$$\tau_{Rad} \cong \frac{1}{B(n_o + p_o)}, \tag{117}$$

and in the high-level injection regime, when δn, $\delta p \gg (n_0 + p_o)$, the radiative recombination rate and lifetime are

$$R_{Rad} \cong B(\delta n)^2, \tag{118}$$

$$\tau_{Rad} \cong \frac{1}{B\delta n}. \tag{119}$$

Infrared detectors typically operate under low incident intensity, so the low-injection case is more relevant, while lasers operate under high-injection.

SRH non-radiative recombination can involve four processes between the carriers, phonons, and trap states: i) electron capture, ii) electron emission, iii) hole capture, and iv) hole emission [56]. The trap concentration is N_t, the capture

coefficients are c_n and c_p for electrons and holes, σ_p, σ_n are the capture cross sections, v_{th} is the three-dimensional mean carrier velocity, E_T is the trap state energy and only one trap energy level is considered here, f_{to} is the probability that the trap state is occupied by an electron at thermal equilibrium, n_1 and p_1 are the ratios of the trap emission and capture coefficients for the electrons and holes and $n_1 p_1 = n_i^2$, and τ_n and τ_p are electron and hole lifetimes as defined below. The net SRH recombination rate under thermal equilibrium is [56]

$$R_{SRH} = \frac{np - n_i^2}{\tau_p(n + n_1) + \tau_n(p + p_1)}, \tag{120}$$

$$\tau_n = \frac{1}{c_n N_t} = \frac{1}{\sigma_n v_{th} N_t}, \tag{121}$$

$$\tau_p = \frac{1}{c_p N_t} = \frac{1}{\sigma_p v_{th} N_t}, \tag{122}$$

$$v_{th} = \sqrt{\frac{8kT}{\pi m^*}}, \tag{123}$$

$$n_1 = \frac{e_n}{c_n} = n_o \frac{(1 - f_{to})}{f_{to}}, \tag{124}$$

$$p_1 = \frac{e_p}{c_p} = p_o \frac{f_{to}}{(1 - f_{to})}. \tag{125}$$

Assuming the trap energy state degeneracy equals one, n_1 and p_1 can also be written as [102]

$$n_1 = n_o e^{\frac{E_T - E_F}{kT}} = n_i e^{\frac{E_T - E_i}{kT}}, \tag{126}$$

$$p_1 = p_o e^{\frac{-(E_T - E_F)}{kT}} = n_i e^{-\frac{E_T - E_i}{kT}}. \tag{127}$$

The emission and capture coefficients, e_n and c_n, are assumed to remain equal to their equilibrium values under external excitation [102]. In the low-level injection case,

$$R_{SRH} \cong \frac{(n_o + p_o)}{\tau_p(n_o + n_1) + \tau_n(p_o + p_1)}\delta n, \tag{128}$$

$$\tau_{SRH} \cong \frac{\tau_p(n_o + n_1) + \tau_n(p_o + p_1)}{n_o + p_o}, \tag{129}$$

and under high-level injection assuming $\delta n = \delta p$ and $\Delta n, \Delta p \gg n_1, p_1$,

$$R_{SRH} \cong \frac{\delta n}{\tau_p + \tau_n}, \tag{130}$$

$$\tau_{SRH} \cong \tau_p + \tau_n. \tag{131}$$

In thermal equilibrium, the total net Auger recombination rate can be written in terms of the electron and hole Auger coefficients, C_n and C_p, as [56]

$$R_{Auger} = \big(C_n n + C_p p\big)(np - n_i^2). \tag{132}$$

When an external excitation is applied, the recombination rate under the assumption of $\delta n = \delta p$ becomes

$$\begin{aligned} R_{Auger} = {} & C_n \Delta n[(n_o + \delta n)(n_o + p_o + \delta n)] \\ & + C_p \Delta n[(p_o + \delta n)(n_o + p_o + \delta n)]. \end{aligned} \tag{133}$$

Under low-level injection, $\Delta n \ll (n_0 + p_o)$,

$$R_{Auger} = \delta n(n_o + p_o)\big(C_n n_o + C_p p_o\big), \tag{134}$$

and under high-level injection, $\Delta n \gg (n_0 + p_o)$,

$$R_{Auger} = (\delta n)^3\big(C_n + C_p\big). \tag{135}$$

The Auger lifetime is then defined using Eq. (111).

The temperature dependence of the different recombination lifetimes is useful for identifying which process is dominating in a semiconductor in certain temperature ranges. Since the samples studied with time-resolved PL were *n*-type SLs, the focus of the following is on *n*-type semiconductors. For an *n*-type semiconductor with a trap energy level between the intrinsic and conduction band energies ($E_i < E_t < E_c$), the SRH temperature-dependence can be divided into three regions as follows [103]

1. $E_t < E_F < E_c$, $n_o > p_o$, n_1, p_1,

$$\tau_{SRH} \approx \tau_{po} = \frac{1}{\sigma_p v_{th} N_t}, \tag{136}$$

which has a $T^{-1/2}$ dependence due to v_{th} having a temperature dependence of $T^{1/2}$.

2. $E_i < E_F < E_t$, $n_o > p_o$, $n_o < n_1$, $n_1 > p_1$, and $p_o > p_1$,

$$\tau_{SRH} \approx \tau_{po} \frac{n_1}{n_o} = \frac{N_v e^{\frac{-E_t}{kT}}}{\sigma_p v_{th} N_t n_o}, \tag{137}$$

with the exponential dominating the temperature behavior, resulting in the lifetime increasing with increasing temperatures.

3. High temperature intrinsic region, $E_F = E_i$, $n_o = p_o = n_i$, $n_1 > n_i$, and $p_1 < n_i$,

$$\tau_{SRH} \approx \frac{N_c e^{\left(\frac{E_g}{2kT} - \frac{E_t}{kT}\right)}}{2\sigma_p v_{th} N_t \sqrt{N_c N_v}} + \frac{1}{2\sigma_n v_{th} N_T}, \tag{138}$$

where again the exponential dominates, but now the lifetime decreases with increasing temperature [103]. An example using the material parameters from MBE sample O is shown in Figure 67. The transitions between regions 1 and 2

and regions 2 and 3 occur at $n_o = n_1$ and $n_o = n_i$, respectively. Changing the trap density or the capture cross sections shift the curves up or down.

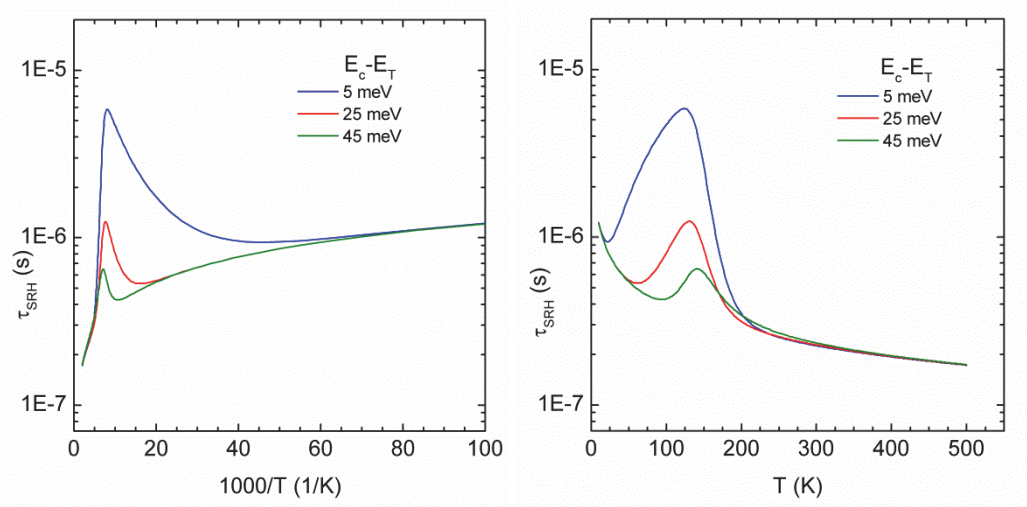

Figure 67. Calculated temperature-dependent SRH lifetime versus a) 1000/T and b) T for three different trap energy levels. The transition temperature between regions 1 and 2 depends on the trap energy level, and the transition between regions 2 and 3 occurs at ~142 K for the given $n_o = 5\text{x}10^{14}$ cm^{-3}.

The temperature dependence of the radiative lifetime can be discerned from the following equations. Writing the radiative lifetime as

$$\tau_{rad} = \frac{1}{B(p_o + n_o + \delta n)} = \frac{n_i^2}{G_r(n_o + p_o + \delta n)}. \tag{139}$$

where G_r is the radiative generation rate given by

$$G_r = \int_{E_g}^{\infty} \frac{cq(f)\alpha(f)}{n_r(f)} df, \tag{140}$$

$$q(f) = \frac{8\pi f^2 n_r^2}{c^3(e^{hf/kT} - 1)}. \tag{141}$$

with the blackbody photon density distribution $q(f)$, index of refraction n_r, absorption coefficient $\alpha(f)$, and speed of light c [104]. The intrinsic carrier concentration is

$$n_i = \sqrt{N_c N_v} e^{-E_g/2kT}. \tag{142}$$

The largest possible radiative lifetime occurs for an intrinsic semiconductor (see Eq. (117)) and under low excitation is [104]

$$\tau_{rad,max} = \frac{n_i}{2G_r}. \tag{143}$$

When the semiconductor is doped, the radiative lifetime is [104]

$$\tau_{rad} = \frac{n_i^2}{G_r(n_o + p_o)}, \tag{144}$$

or in terms of the compensated dopant density, $N_r = n_o - p_o$, [104]

$$\tau_{rad,doped} = \frac{n_i^2}{G_r\left(\sqrt{4n_i^2 + N_r^2}\right)}, \tag{145}$$

and at low temperatures when n_i is extremely small, [104]

$$\tau_{rad,LowTemp} \cong \frac{n_i^2}{G_r N_r}. \tag{146}$$

Both n_i and G_r have temperature dependence, but G_r has a stronger dependence on temperature than n_i in some temperature ranges [104]. Blakemore states at higher temperatures, i.e. above 180 K, n_i^2 and G_r have about the same temperature dependence, so the lifetime is essentially temperature independent [104]. For higher temperatures, the bandgap decreases which increases n_i^2, and the number of blackbody photons above the bandgap increases, so G_r also increases. Blakemore assumes G_r varies as $e^{-\frac{Eg+\delta}{kT}}$ with δ being small compared to E_g. Then for lower temperatures the radiative lifetime is proportional to $T^{3/2}$ as shown by

$$\tau_{rad} = \frac{n_i^2}{G_r N_r} = \frac{1}{G_r N_r} N_c N_v e^{-\frac{E_g}{kT}} \propto T^{\frac{3}{2}} \frac{e^{-\frac{E_g}{kT}}}{e^{-\frac{E_g+\delta}{kT}}} \sim T^{\frac{3}{2}}. \quad (147)$$

If the temperature dependence of the bandgap is ignored, as is reasonable below 60 K for these SL samples, or perhaps for much larger bandgap materials with δ small compared to E_g, the radiative lifetime is again proportional to $T^{3/2}$. The radiative lifetime in intrinsic material should vary as $e^{-E_g/2kT}$ due to the exponential term dominating the other temperature dependences [103]. As shown in Figure 68 below, where each term is scaled to the same order of magnitude for comparison, this is the case at high temperatures where the material is intrinsic.

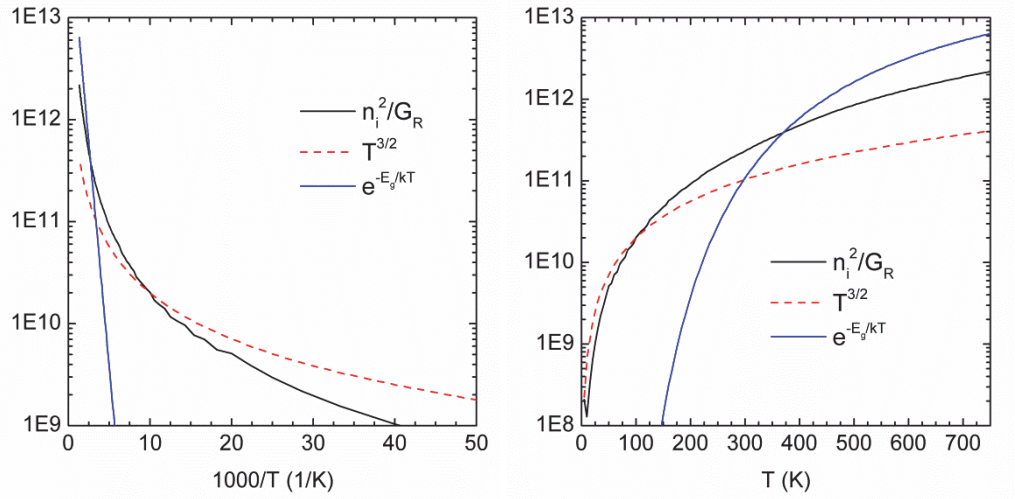

(a) (b)

Figure 68. Calculated temperature dependence of the terms in the radiative lifetime equation. Each term is scaled to the same order of magnitude for comparison.

For *n*-type narrow bandgap semiconductors, the Auger CHCC process, or A1, dominates and the net Auger recombination rate is [103]

$$R_{Auger} = C_{n,A1} n(np - n_i^2), \quad (148)$$

$$C_{n,A1} = \frac{8(2\pi)^{\frac{5}{2}} q^4 m_o}{h^3 (4\pi\varepsilon_o\varepsilon_s)^2} \left(\frac{\left(\frac{m_e^*}{m_o}\right) |F_1 F_2|^2}{(1+\mu)^{\frac{1}{2}}(1+2\mu)} \right) \frac{1}{n_i^2} \left(\frac{kT}{E_g}\right)^{\frac{3}{2}} e^{-\left(\frac{1+2\mu}{1+\mu}\right)\frac{E_g}{kT}}, \quad (149)$$

$$\mu = \frac{m_e^*}{m_{hh}^*}. \quad (150)$$

The relative static dielectric constant is ε_s, and the overlap integrals are F_1 and F_2. The value of $|F_1 F_2|$ is usually between 0.1 and 0.3, which can change the lifetime by an order of magnitude [103]. Assuming the bands are parabolic and the semiconductor is non-degenerate, $\mu \ll 1$. Then the Auger lifetime for intrinsic material is [103]

$$\tau_{A1}^i = \frac{3.8x10^{-18}\varepsilon_s^2 (1+\mu)^{\frac{1}{2}}(1+2\mu)}{\left(\frac{m_e^*}{m_o}\right)|F_1 F_2|^2 \left(\frac{kT}{E_g}\right)^{\frac{3}{2}}} e^{\left(\frac{1+2\mu}{1+\mu}\right)\frac{E_g}{kT}}, \quad (151)$$

and for extrinsic materials is [103]

$$\tau_{A1} = \frac{2\tau_{A1}^i}{\left(\frac{n_o^2}{n_i^2} + 1\right)}. \quad (152)$$

To observe the Auger lifetime temperature dependence, the above equations are calculated using the parameters of MBE sample O and graphed below in Figure 69 for three values of the electron effective mass. At high temperatures in the intrinsic region, the Auger lifetime decreases with increasing temperature, and at very low temperatures in the extrinsic region, the lifetime also decreases with increasing temperature. Between these two regions, the temperature behavior of the Auger lifetime depends on the electron effective mass but is comparatively constant.

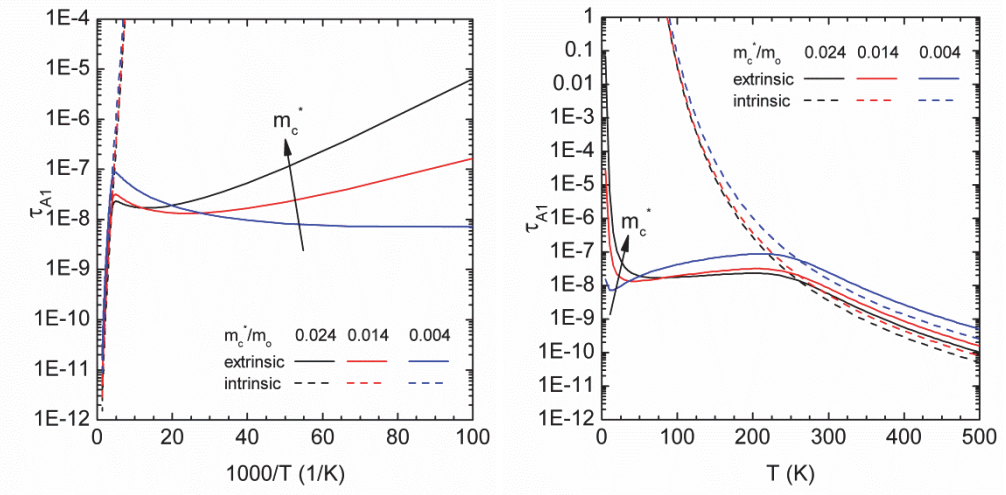

(a) (b)

Figure 69. Calculated Auger lifetime temperature dependence for three values of electron effective mass.

6.3 Time-resolved photoluminescence experiment

The InAs/$InAs_{1-x}Sb_x$ T2SLs were designed with AlSb barriers for TRPL measurements. The AlSb barriers ensure that the measured PL decay time is due to carrier recombination in the T2SL and the influence of carrier transport, surface recombination, or any junction fields within the sample is minimized. Studies of a T2SL homojunction have shown that the restoring current in a narrow-bandgap junction results in an ostensibly long PL lifetime [98]. The samples were grown by molecular beam epitaxy on undoped 2-inch GaSb substrates with a 500-nm GaSb buffer layer. The T2SLs consist of varying number of periods of InAs and $InAs_{1-x}Sb_x$ totaling 500 nm-thick. The T2SLs were unintentionally doped *n*-type (~$3x10^{16}$ cm^{-3} at 10 K) as determined by Hall measurements. AlSb barrier layers (100 Å), above and below the T2SLs, are used to confine the electrons to the superlattice as well as to provide an adequate heavy hole barrier of over 100 meV.

The entire structure is capped with 100 Å of p^+ InAs. Photoluminescence (PL) measurements show peak emission from 5 –8.2 μm (150 meV) at 77 K.

TRPL measurements were performed on the T2SL samples at 11, 40, 77, 110, 150, 200, and 250 K. An ultrafast laser with ~100 fs pulses at a 250 kHz repetition rate with 2 μm (0.62 eV) emission wavelength (energy) was used to excite carriers in only the T2SL region to excess carrier densities between 10^{15} and 10^{17} cm^{-3}. The carrier concentrations were calculated using an absorption coefficient of 10^4 cm^{-1} from published *n*-type InAs room-temperature absorption data at 0.62 eV [105]. This is a reasonable absorption coefficient value given that the laser pump energy is well above the SL band edge energy. The PL was detected with an HgCdTe detector operating at 200 K with a 3 ns temporal resolution and a 1 x 1 mm^2 detector area. A 3.6 μm long pass filter isolated the PL signal from the pump laser scattering. Further details of the experimental technique can be found in Ref. [82].

6.4 Lifetime results and discussion

The TRPL signal for MBE sample O at 77 K is shown in Figure 70 for a sampling of initial excess carrier densities, $\delta p_{t=0}$, between 4.0×10^{15} and 1.0×10^{17} cm^{-3}. For the highest $\delta p_{t=0}$, 1.0×10^{17} cm^{-3}, a fast initial decay was observed in the PL signal, and the instantaneous PL lifetime increased significantly as the signal decayed. For the lowest initial excess carrier density of 4.0×10^{15} cm^{-3}, the PL signal approached a single exponential decay, indicating excitation levels were much lower than the background doping density (at least an order of magnitude lower) and the low-excitation regime is approached.

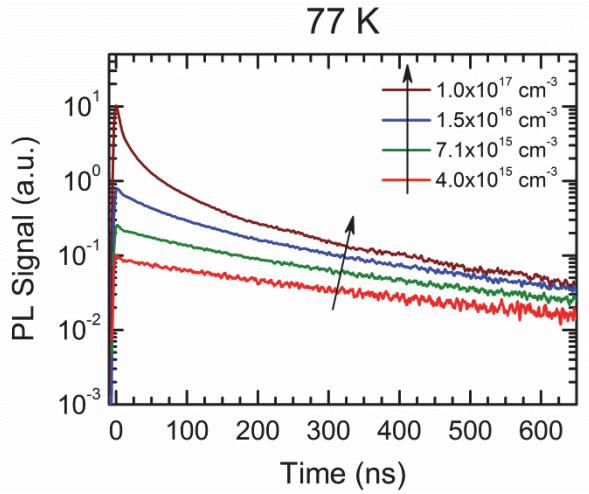

Figure 70. Time-resolved photoluminescence measurements on MBE T2SL sample O ($InAs/InAs_{0.72}Sb_{0.28}$) at 77 K for initial excess carrier densities ranging from $4.0x10^{15}$ to $1.0x10^{17}$ cm^{-3}. **Data acquired at ARL with Dr. Blair Connelly.*

As described in Ref. [82], at a given temperature the PL intensity is only a function of the excess carrier density, δp. Therefore, the PL data taken at lower $\delta p_{t=0}$ can be shifted in time to overlap with the data taken at higher $\delta p_{t=0}$. This shifting process provided a combined PL decay signal with an improved signal-to-noise ratio. Figure 71 shows combined curves for temperatures from 11 – 250 K with initial excess carrier densities of $1.0x10^{17}$ cm^{-3}.

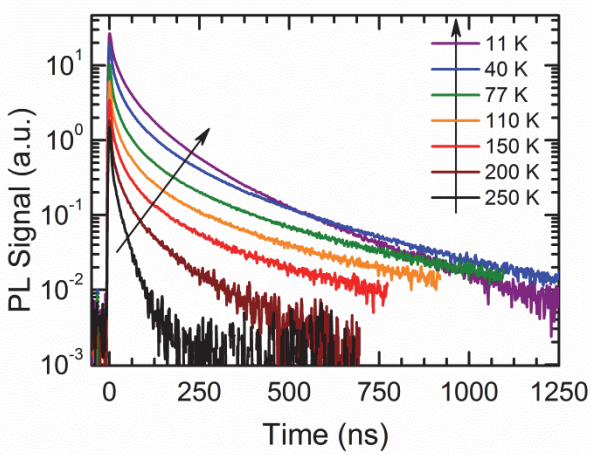

Figure 71. Combined temperature-dependent time-resolved photoluminescence decay measurements on MBE T2SL sample O ($InAs/InAs_{0.72}Sb_{0.28}$). **Data acquired at ARL with Dr. Blair Connelly.*

At each temperature, the decay rate of the PL signal showed a strong dependence on δp, evolving from a faster decay in the first 100 ns, which corresponded to excess carrier densities > $5x10^{16}$ cm^{-3}, to a slower, almost single exponential decay at the tail end of the decay, which corresponded to excess carrier densities < $5x10^{15}$ cm^{-3}. This strong dependence of the carrier lifetime on the excess carrier density cannot be explained by SRH recombination alone. Contributions from radiative or Auger recombination, which vary strongly with excess carrier density, must also be considered.

Under typical detector operating conditions, only very small excess carrier densities on the order of 10^{12} cm^{-3} are expected [106], so it is important to determine the carrier lifetime in the low-excitation regime where the lifetime is independent of the excess carrier density to predict device performance. Therefore, the tail of the TRPL data, where the excitation level is low (~10^{15} cm^{-3}) compared to the background doping density (~10^{16} cm^{-3}), was fit with a single exponential decay to obtain the lifetime, τ, at each temperature. The resulting PL lifetimes from the fit are plotted in Figure 72 (points) as a function of inverse temperature. When the PL decay rate reaches a single exponential decay in the low-excitation regime, the PL lifetime is equivalent to the minority carrier lifetime. At higher excitation levels, however, the PL lifetime is shorter than the minority carrier lifetime. Since the lowest excitation levels used in this study are just approaching the low-excitation regime, the measured PL lifetime represents a lower limit of the minority carrier lifetime.

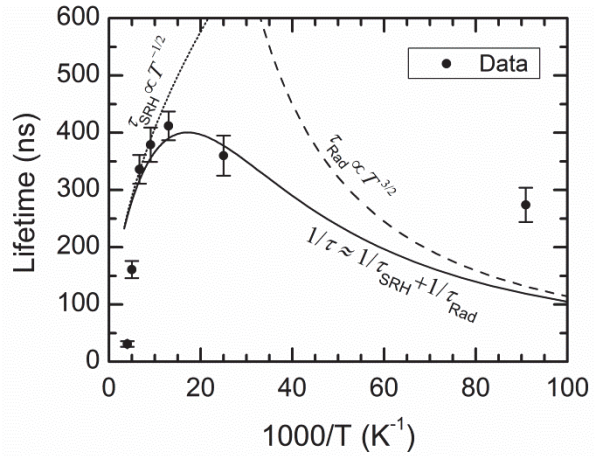

Figure 72. Carrier lifetimes extracted from the fits in Figure 71 of the PL decay are shown as points as a function of 1000/T. Also plotted is the temperature dependence of the SRH lifetime ($\tau_{SRH} \propto T^{-1/2}$, dotted line), radiative lifetime ($\tau_{Rad} \propto T^{3/2}$, dashed line), and a combination of both SRH and radiative lifetimes (solid line). **Data acquired at ARL with Dr. Blair Connelly.*

The PL lifetime is observed to increase from low temperature (11 K) to a maximum of 412 ns at 77 K. This lifetime is an order-of-magnitude longer than the SRH-limited lifetime of ~30 ns that was previously observed in LWIR InAs/$Ga_{1-x}In_xSb$ T2SL absorber layers at 77 K [38, 82, 97]. The temperature dependence of the lifetime can be attributed to a combination of both SRH and radiative recombination. For illustration, the temperature dependence of the SRH lifetime ($\tau_{SRH} \propto T^{1/2}$, dotted line), radiative lifetime ($\tau_{Rad} \propto T^{3/2}$, dashed line), and a combination of SRH and radiative lifetimes (solid line) are plotted along with the data in Figure 72 [107]. At temperatures below 77 K, the PL lifetime increases with increasing temperature, indicating that the lifetime is dominated by radiative recombination and that the radiative lifetime is shorter than the non-radiative (SRH) lifetime. At temperatures above 77 K, the PL lifetime decreases with increasing temperature, signifying that the PL lifetime is dominated by SRH recombination and the radiative lifetime is longer than the SRH lifetime. Around

77 K, both radiative and SRH recombination contribute significantly to the lifetime.

Using the absorption and index of refraction data measured with ellipsometry at room temperature, the bandgap variation with temperature from PL measurements, and the measured carrier concentration at 10 K (~10^{16} cm^{-3}), the data in Figure 72 for MBE sample O can be fit with Eq.'s (136)-(138), (145), and (152) using the parameters shown in Table 25. The simulated lifetimes versus temperature and the measured lifetime data are shown in Figure 73 for MBE sample O.

Table 25. Parameters for simulations of Radiative, SRH, and Auger lifetimes.

Sample	n_o (x10^{16} cm^{-3})	$E_g(0)$ (meV)	m_c^*/m_o	m_h^*/m_o	E_t (meV)	N_t (x10^{12} cm^{-3})	$\sigma_p = \sigma_n$ (cm^2)
K (2301029)	2	231	0.030	0.41	5	1	1x10^{-14}
O (2301033)	0.05	160	0.024	0.41	43	1.5	5x10^{-14}

At high temperatures, the lifetime follows the intrinsic Auger lifetime due to the large number of thermally-generated carriers. In the mid-temperature range from 50 – 150 K, SRH processes are shown to dominate, while at very low temperatures, radiative recombination becomes important and balances the effect of SRH to keep the lifetime fairly constant at low temperatures. As can be seen in Figure 73b, the Auger temperature dependence is also fairly constant in the 50 – 150 K range. To distinguish between the SRH and Auger mechanisms in the mid-temperature range, the integrated PL versus temperature was analyzed.

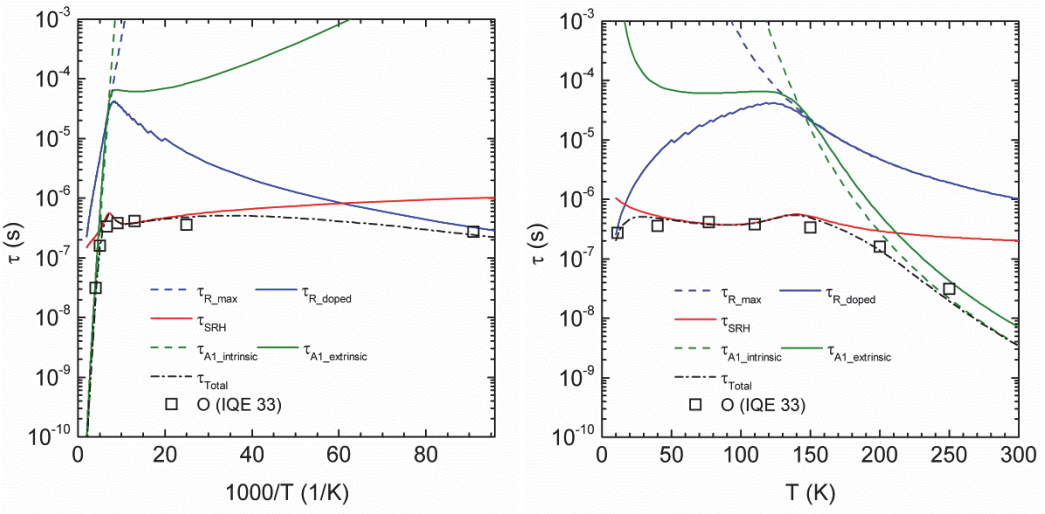

(a) (b)

Figure 73. Lifetime data and simulation versus temperature for MBE sample O.

The normalized integrated PL intensity is plotted versus temperature for MBE sample O in Figure 74. Also shown is the calculated curve given by $2500/T^2 - 0.04$, which agrees with the data very well above 80 K. The $1/T^2$ dependence is indicative of SRH recombination [108], so the simulated lifetimes in Figure 73 are appropriate fits to the data.

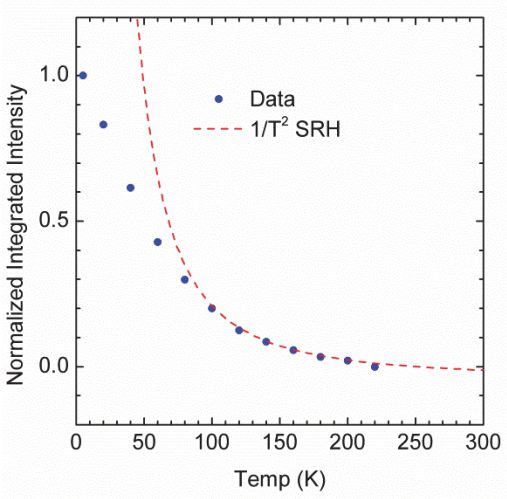

Figure 74. The temperature-dependent normalized integrated intensity of MBE sample O showing the SRH and radiative. **Data acquired at AFRL/RXPS.*

The lifetimes of several other samples in MBE set 5 were measured at the ARL under varying intensities and temperatures as well. These data were analyzed similarly to sample O as described above. One of the samples, MBE sample Q, displayed temperature-dependent lifetime behavior very analogous to that of sample O, as shown in Figure 75 below. These two samples have the largest periods of 245 Å and 180 Å and the smallest calculated wave function overlaps of 0.26 and 0.37 for O and Q, respectively, of MBE sample set 5.

MBE samples K, L, M, N, and P have very different lifetime temperature dependences from samples O and Q, as shown in Figure 76. Above 200 K, in the intrinsic region, this group of samples also exhibited Auger lifetime temperature dependence. However, the lifetimes drop significantly from 150 – 50 K where samples O and Q had fairly constant lifetimes. The calculated wave function

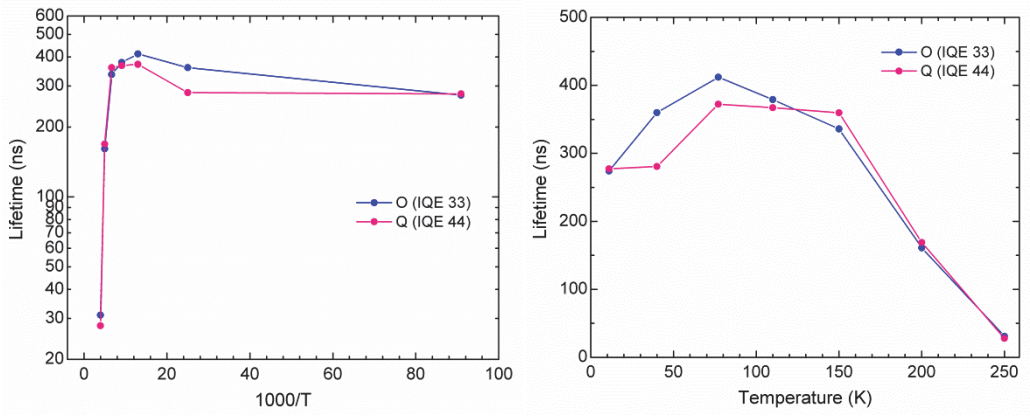

(a) (b)

Figure 75. Temperature-dependent lifetime data for MBE samples O and Q.
**Data acquired at ARL with Dr. Blair Connelly.*

overlaps of these samples range from 0.51 to 0.63, twice that of sample O, and the SL periods are considerably smaller in the range of 73 Å to 107 Å, half that of

sample O. These facts point to radiative recombination causing the difference in the lifetime temperature dependent behavior.

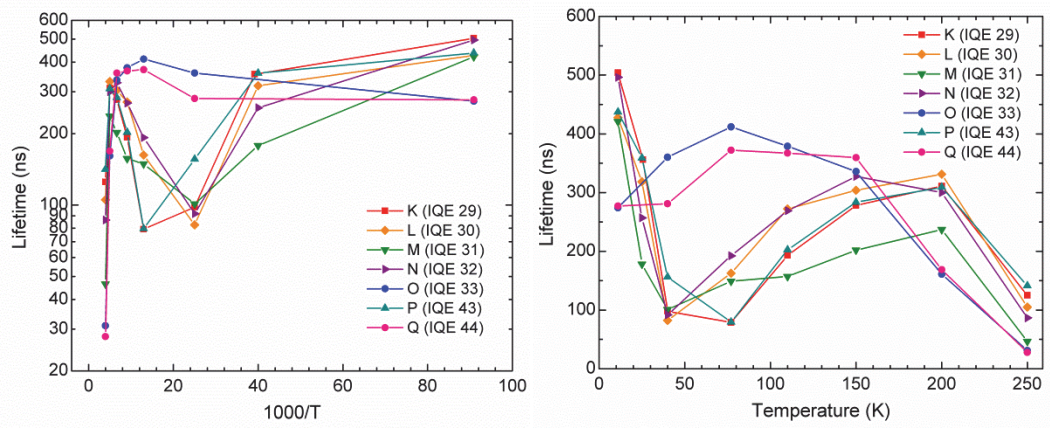

(a) (b)

Figure 76. Temperature-dependent lifetime data for MBE samples K, L, M, N, O, P, and Q. **Data acquired at ARL with Dr. Blair Connelly.*

To investigate the effects of the radiative lifetime on these short period SL samples, simulations of the data for sample K were carried out using Eq.'s (136)-(138), (145), and (152) and the parameters are shown in Table 25. The simulation results are shown in Figure 77. Indeed, radiative recombination describes the lifetime behavior from 50 – 150 K very well using a background carrier concentration that agrees with the Hall data (~10^{16} cm^{-3}), but the radiative model cannot fit the low temperature behavior below 50 K. Again, the integrated PL intensity for sample K was examined to gain insight into the recombination mechanisms' variation with temperature. The results are shown in Figure 78 and have the same form as those of an InAs/$Al_{0.48}In_{0.52}As$ multiple quantum well structure [109].

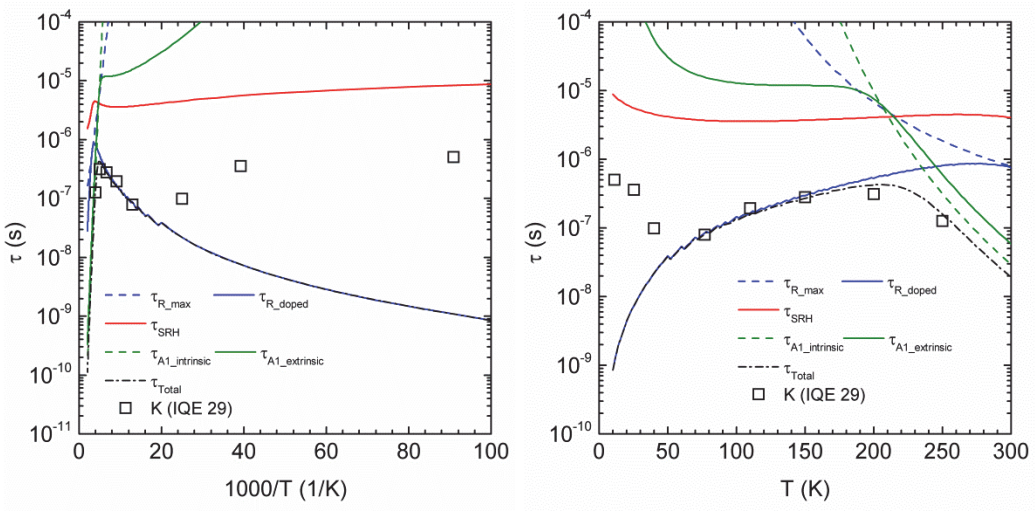

(a) (b)

Figure 77. Lifetime data and simulations versus temperature for MBE sample K.

The normalized integrated intensity versus temperature cannot be described by the $1/T^2$ (red dashed curve) form that was apparent for sample O. Instead, the intensity is quite constant below 50 K and drops almost linearly above 50 K. The integrated PL intensity should be almost independent of temperature when radiative recombination dominates [108], suggesting the lifetime below 50 K is also due to radiative recombination despite the fact that the current model cannot reproduce trend of the data in that region. The temperature dependence was fit well in the entire temperature range with the following equation [110]

$$\frac{I(T)}{I_o} = \frac{1}{1 + Ce^{-\frac{E_a}{kT} + \frac{T}{T_H}}}, \tag{153}$$

which includes a thermal activation energy, E_a, necessary to dissociate the excitons before they can recombine radiatively and a temperature characteristic of tunneling between quantum domains, or a hopping mechanism, T_H. The hopping temperature leads to an average distance, l, between domains through the relation

$$kT_H = \frac{\hbar^2}{2\pi^2 l^2 m_e^*}. \tag{154}$$

The green dashed fit of Eq. (153) in Figure 78 used $C = 0.31$, $E_a = 8.1$ meV, and $T_H = 85$ K which gives $l = 4.2$ nm.

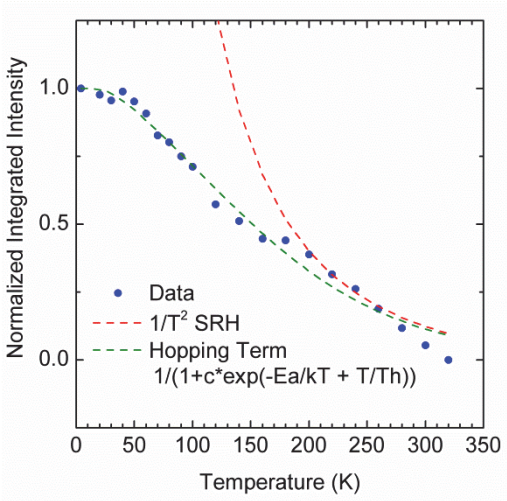

Figure 78. The temperature-dependent normalized integrated PL intensity of MBE sample K showing fits to the data. **Data acquired at AFRL/RXPS.*

The hopping process could occur laterally in the SL between localized band tail states that form due to in-plane compositional and layer thickness non-uniformity [111, 112]. The relative lateral variations in layer thickness and composition would be more pronounced for thinner layers than thick layers, indicating why samples O and Q do not show the same temperature-dependent lifetime behavior. Similar differences in the time-resolved PL lifetime temperature dependence were seen for 2 monolayer quantum well and 5 monolayer multiple quantum well samples comprised of InAs/InAlAs [109]. The localization potential for the excitons has been shown to be greater for thinner well widths and the exciton binding energy to increase due to this potential [113].

Thus, the SLs with smaller layer thicknesses will maintain longer lifetimes to higher temperatures as shown in Figure 79 and further summarized in Table 26.

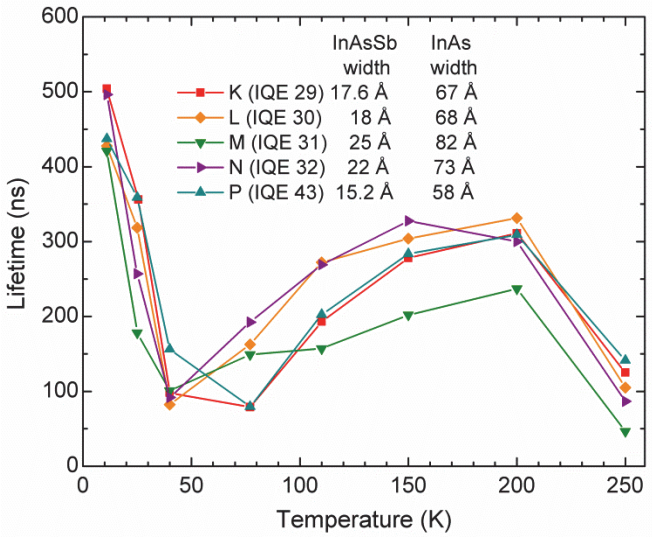

Figure 79. Lifetime temperature dependence of the short period SL samples.

The decrease in the lifetime from 11 K to 25 K is largest for the larger layer width samples in this shorter-period set. Fitting the lifetime with a decreasing exponential, $\tau_o - ce^{-\frac{E_a}{kT}}$, from 11 – 77 K results in the activation energies (listed in Table 26) necessary to overcome the lateral localization potentials. These activation energies increase as the layer thicknesses decrease. The result for sample K (5.8 meV) agrees reasonably well with activation energy (8.1 meV) found from Eq. (153).

Table 26. Summary of short-period SL characteristics.

Sample Set 5	Δτ (11-25 K)	x ± 0.01	t_{InAs} (Å)	t_{InAsSb} (Å)	Wave function overlap	E_a (meV)
M (2301031)	243	0.35	82.0	25.3	0.51	0.2
N (2301032)	239	0.35	73.2	21.8	0.55	2.2
K (2301029)	148	0.37	66.6	17.6	0.59	5.8
L (2301030)	110	0.39	68.1	18.0	0.57	6.1
P (2301043)	78	0.41	57.8	15.2	0.63	7.2

The temperature dependence of the integrated PL intensity has been related to the lifetime temperature dependence by the following equation [109, 114]

$$I_{PL}(T) = I_o \frac{\tau_{PL}(T)}{\tau_R(T)}, \tag{155}$$

where $\tau_{PL}(T)$ is the measured lifetime from the PL decay and $\tau_R(T)$ is the radiative lifetime. I_o is the integrated PL intensity at the lowest measured temperature, is assumed to depend only on the carrier concentration, and is attributed only to radiative recombination at 10 K.

The measured lifetime can be written as [109, 114]

$$\frac{1}{\tau_{PL}(T)} = \frac{1}{\tau_R(T)} + \frac{1}{\tau_{NR}(T)}, \tag{156}$$

and when combined with Eq. (155) allows the radiative and non-radiative lifetimes to be written in terms of the measured PL lifetime as

$$\tau_R(T) = \frac{I_o}{I_{PL}(T)} \tau_{PL}(T), and \tag{157}$$

$$\tau_{NR}(T) = \frac{I_o}{I_o - I_{PL}(T)} \tau_{PL}(T). \tag{158}$$

The results of combining the TRPL lifetime data and the integrated PL intensity data are shown in Figure 80 for samples O and K. For sample O, the measured PL lifetime is due to radiative recombination up to 77 K, and above 77 K non-radiative recombination dominates, confirming the results obtained above. Sample K has radiative recombination dominating the PL lifetime all the way up to 200 K when non-radiative recombination dominates. The lifetime behavior below 50 K is still attributed to radiative recombination since the non-radiative

lifetimes are an order of magnitude greater than the top of the scale shown in the figure. The effects of exciton localization explain the lifetime behavior below 50 K for sample K.

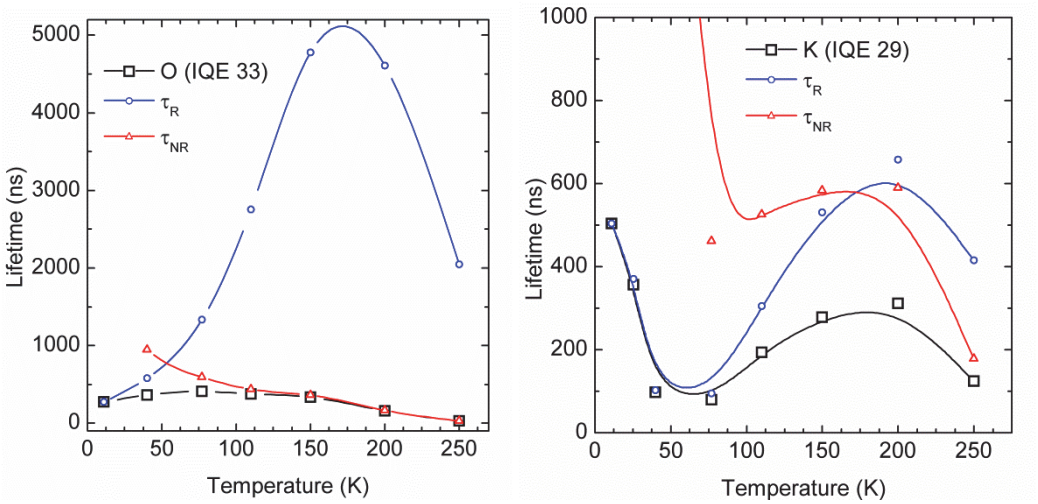

(a) (b)

Figure 80. Measured lifetime data and calculated radiative and non-radiative lifetimes for MBE samples (a) O and (b) K versus temperature.

The improved lifetimes observed in these InAs/$InAs_{1-x}Sb_x$ T2SL samples offer evidence that the constituent InAs and InAsSb layers have excellent crystalline properties and the samples possesses a low density of non-radiative recombination centers at the interfaces and in the layers. The InAs/$InAs_{0.72}Sb_{0.28}$ T2SL (sample O) has a longer lifetime than even bulk InAs at 77 K due to the decreased radiative transition probability of a type-II structure compared to that of a direct bandgap bulk material. These results also shine some light on the origin of the relatively short carrier lifetime (~30 ns) in LWIR InAs/$Ga_{1-x}In_xSb$ T2SLs, which could be due to the non-radiative recombination centers associated with Ga atoms. Furthermore, the "stabilized Fermi level" due to intrinsic point defects in bulk GaSb and GaAs are near the valence band edge or the midgap, respectively

[42], leaving mid-gap trap states available for SRH recombination. In comparison, in bulk InAs, the stabilized Fermi level is above the conduction band edge [42], rendering any mid-gap defect states inactive for SRH processes, as demonstrated by relatively high photoluminescence efficiencies in As-rich InAs/InAsSb T2SLs [115].

6.5 Summary

In summary, an order-of-magnitude longer minority carrier lifetime (> 412 ns at 77 K) was observed in the LWIR InAs/$InAs_{0.72}Sb_{0.28}$ T2SL sample O studied compared to that observed in LWIR InAs/$Ga_{1-x}In_xSb$ T2SLs. In addition, the observed carrier lifetime in InAs/$InAs_{0.72}Sb_{0.28}$ is longer across all temperatures than that previously reported in InAs/$Ga_{1-x}In_xSb$ T2SLs. Measurements on several other InAs/$InAs_{1-x}Sb_x$ T2SLs also show substantially longer minority carrier lifetimes (100's of ns). The longer period T2SLs have both SRH and radiative recombination mechanisms apparent, with comparable contributions from both near 77 K. The shorter period T2SLs have much higher wave function overlaps and therefore radiative recombination is seen to dominate all the way until the high temperature intrinsic region is reached. At very low temperatures, below 50 K, exciton localization causes the radiative lifetime to increase.

This minority carrier lifetime improvement may now enable background limited T2SL LWIR *pn* photodetectors at higher operating temperatures. It should be noted that the InAs/$InAs_{1-x}Sb_x$ T2SL sample growth and material properties have not been optimized yet, suggesting that there is still room for improvement in the InAs/$InAs_{1-x}Sb_x$ T2SL minority carrier lifetime. Since the

non-radiative recombination rate has now been significantly reduced, future studies can examine the tradeoff between radiative and non-radiative recombination, and sample designs can be optimized to balance lowering the wave function overlap to decrease the radiative recombination rate with increasing the wave function overlap to increase the absorption coefficient.

7. CONCLUSIONS AND RECOMMENDATIONS FOR FUTURE RESEARCH

Strain-balanced InAs/$InAs_{1-x}Sb_x$ T2SLs have been carefully studied and shown to be promising materials for infrared photodetectors. Properly designing an InAs/$InAs_{1-x}Sb_x$ superlattice for an infrared photodetector requires using the right theoretical models and the choice of accurate material parameters. The critical thickness model, zero-stress strain-balancing model, bandgap equation for $InAs_{1-x}Sb_x$, valence band offset between InAs and $InAs_{1-x}Sb_x$, and the three-band envelope approximation band structure model were used to design the T2SL structures studied in this work.

The InAs/$InAs_{1-x}Sb_x$ T2SL bandgap determined by the experimental PL measurements allowed the valence band offsets between InAs and $InAs_{1-x}Sb_x$ to be determined by fitting the above mentioned model parameters to the measured SL bandgaps. The valence band offset between InAs and $InAs_{1-x}Sb_x$ with $x = 0.28 - 0.41$ strained on GaSb was best described by the fractional valence band offset, $Q_v = \Delta E_v/\Delta E_g$, of 1.75 ± 0.03. The valence band offsets were also seen to depend on the growth conditions for different sample sets due to varying degrees of As/Sb intermixing at the SL interfaces. The model used to calculate the SL bandgap assumed abrupt interfaces between the SL layers, which is not the exact case in reality.

Time-resolved PL measurements on InAs/$InAs_{1-x}Sb_x$ SL samples grown by MBE gave information about the minority carrier lifetime. The recombination in the samples with larger periods, lower wave function overlaps, and smaller

bandgaps was dominated by radiative recombination below 77 K and SRH recombination above 77 K until the intrinsic region was reached and intrinsic Auger recombination dominated. The T2SL samples with shorter periods, higher wave function overlaps, and larger bandgaps had lifetimes dominated by radiative recombination below 200 K. Shorter SL periods resulted in greater effects of lateral compositional and relative layer thickness variations, larger exciton localization potentials, and longer lifetimes at low temperatures. A tradeoff must be reached between thin layers for increased absorption and long lifetimes at desired temperatures for particular designs. As expected, the lifetimes of the two larger period samples with bandgaps of ~8 μm had lifetimes significantly longer than those of LWIR InAs/$Ga_{1-x}In_xSb$ SLs at 77 K. The order of magnitude increase in the lifetime confirms that SRH recombination is indeed less effective, although still present, in InAs/$InAs_{1-x}Sb_x$ SLs than in InAs/$Ga_{1-x}In_xSb$ SLs.

These updated valence band offset results will enable better design of InAs/$InAs_{1-x}Sb_x$ SLs for MWIR and LWIR photodetectors, and the minority carrier lifetime improvement supports these SLs being capable of lower detector dark currents and higher quantum efficiencies than InAs/$Ga_{1-x}In_xSb$ SLs if processed into devices.

There is still much to be investigated regarding these InAs/$InAs_{1-x}Sb_x$ SLs. Designs with large enough SL periods will allow further study of the carrier lifetimes and recombination mechanisms, such as the effects of growth temperatures and interfaces, to improve the SL material quality for devices. Understanding the As/Sb intermixing at the interfaces using TEM and XRD will

further the understanding of the effects of the growth processes on the structural and optical properties of the SL, and including the interface intermixing into the model for the SL bandgap will enable more accurate predictions of the SL bandgaps and valence band offsets. An extension to the valence band offset study would be to use SL designs with larger periods to ensure the possibility of confined electron levels for both type-II alignments. A comparison between the same T2SL material grown by MBE and by MOCVD would be very interesting, although it may be very difficult to achieve the same design with both methods. Although the InAs/$InAs_{1-x}Sb_x$ was demonstrated to cover both the MWIR and LWIR ranges, it may offer the best advantages in the LWIR, or beyond, where the lifetime is significantly greater than that of InAs/$Ga_{1-x}In_xSb$ SL.

I look forward to seeing what the future will hold for the InAs/$InAs_{1-x}Sb_x$ superlattice material in infrared devices.

REFERENCES

[1] M. A. Kinch. *Fundamentals of Infrared Detector Materials, (Tutorial Texts in Optical Engineering),* vol. *TT76, 2007.*

[2] D. R. Rhiger, "Performance Comparison of Long-wavelength Infrared Type II Superlattice Devices with HgCdTe," *J Electron Mater,* vol. 40, pp. 1815-22, Aug 2011.

[3] L. Esaki and R. Tsu, "Superlattice and negative differential conductivity in semiconductors," *IBM Journal of Research and Development,* vol. 14, pp. 61-5, Jan 1970.

[4] G. Sai-Halasz, R. Tsu and L. Esaki, "A new semiconductor superlattice," *Appl. Phys. Lett.,* vol. 30, pp. 651-3, June 1977.

[5] H. Sakaki, L. L. Chang, G. Sai-Halsz, C. A. Chang and L. Esaki, "Two-dimensional electronic structure in InAs-GaSb superlattices," *Solid State Commun.,* vol. 26, pp. 589-92, June 1978.

[6] G. C. Osbourn, "InAsSb strained-layer superlattices for long wavelength detector applications," *J. Vac. Sci. Technol. B,* vol. 2 (2), pp. 176-178, Feb 1984.

[7] J. N. Schulman and T. C. McGill, "The CdTe/HgTe superlattice: proposal for a new infrared material," *Appl. Phys. Lett.,* vol. 34, pp. 663-5, May 1979.

[8] G. C. Osbourn, L. R. Dawson, R. M. Biefeld, T. E. Zipperian, I. J. Fritz and B. L. Doyle, "III-V strained layer superlattices for long-wavelength detector applications: Recent progress," *J. Vac. Sci. Technol. A,* vol. 5 (5), pp. 3150-3152, Sept/Oct 1987.

[9] J. Bajaj, G. Sullivan, D. Lee, E. Aifer and M. Razeghi, "Comparison of type-II superlattice and HgCdTe infrared detector technologies," *Proc. SPIE 6542,* pp. 65420B (8 pp.), 2007.

[10] D. L. Smith, T. C. McGill and J. N. Schulman, "Advantages of the HgTe-CdTe superlattice as an infrared detector material," *Appl. Phys. Lett.,* vol. 43, pp. 180-2, April 1983.

[11] D. H. Chow, R. H. Miles, J. N. Schulman, D. A. Collins and T. C. McGill, "Type II superlattices for infrared detectors and devices," *Semicond. Sci. Technol.*, vol. 6, pp. C47-C51, 1991.

[12] S. D. Gunapala, D. Z. Ting, C. J. Hill, J. Nguyen, A. Soibel, S. B. Rafol, S. A. Keo, J. M. Mumolo, M. C. Lee, J. K. Liu and A. Liao, "Demonstration of megapixel LWIR superlattice focal plane array," in *2010 23rd Annual Meeting of the IEEE Photonics Society (Formerly LEOS Annual Meeting)*, pp. 637-8, 2010.

[13] M. Sundaram, A. Reisinger, R. Dennis, K. Patnaude, D. Burrows, J. Bundas, K. Beech and R. Faska, "SLS technology: The FPA perspective," *Proc. SPIE 7660,* pp. 76601P (9 pp.), 2010.

[14] M. Razeghi, D. Hoffman, B. Nguyen, P. Delaunay, E. K. Huang, M. Z. Tidrow and V. Nathan, "Recent advances in LWIR Type-II InAs/GaSb superlattice photodetectors and focal plane arrays at the center for quantum devices," *Proc IEEE,* vol. 97, pp. 1056-1066, 2009.

[15] F. Rutz, R. Rehm, J. Schmitz, J. Fleissner, M. Walther, R. Scheibner and J. Ziegler, "InAs/GaSb superlattice focal plane array infrared detectors: manufacturing aspects," *Proc. SPIE 7298,* pp. 72981R (10 pp.), 2009.

[16] I. Vurgaftman, C. L. Canedy, E. M. Jackson, J. A. Nolde, C. A. Affouda, E. H. Aifer, J. R. Meyer, A. Hood, A. J. Evans and W. T. Tennant, "Analysis and performance of type-II superlattice infrared detectors," *Optical Engineering,* vol. 50, 2011.

[17] D. Donetsky, G. Belenky, S. Svensson and S. Suchalkin, "Minority carrier lifetime in type-2 InAs-GaSb strained-layer superlattices and bulk HgCdTe materials," *Appl. Phys. Lett.,* vol. 97, pp. 052108 (3 pp.), Aug 2010.

[18] Y.-H. Zhang, "InAs/$InAs_xSb_{1-x}$ type-II superlattice midwave infrared lasers," in *Optoelectronic Properties of Semiconductors and Superlattices: Antimonide-Related Strained-Layer Heterostructures*, M. O. Manasreh, Ed. Gordon Breach, pp. 461-500, 1997.

[19] C. H. Grein, M. E. Flatte and H. Ehrenreich, "Comparison of ideal InAs-$InAs_{1-x}Sb_x$ and InAs-$In_xGa_{1-x}Sb$ superlattice IR detectors," in *Proceedings of the Third International Symposium on Long Wavelength Infrared Detectors and Arrays: Physics and Applications III*, pp. 211-18, 1995.

[20] Y. Huang, J.-H. Ryou, R. D. Dupuis, V. R. D'Costa, E. H. Steenbergen, J. Fan, Y.-H. Zhang, A. Petschke, M. Mandl and S.-L. Chuang, "Epitaxial growth and characterization of InAs/GaSb and InAs/InAsSb type-II superlattices on GaSb substrates by metalorganic chemical vapor deposition for long wavelength infrared photodetectors," *J. Cryst. Growth,* vol. 314, pp. 92-6, Jan 2011.

[21] S. R. Kurtz, L. R. Dawson, R. M. Biefeld, D. M. Follstaedt and B. L. Doyle, "Ordering-induced band-gap reduction in $InAs_{1-x}Sb_x$ (x=0.4) alloys and

superlattices," *Physical Review B (Condensed Matter),* vol. 46, pp. 1909-12, July 1992.

[22] D. Lackner, O. J. Pitts, M. Steger, A. Yang, M. L. W. Thewalt and S. P. Watkins, "Strain balanced InAs/InAsSb superlattice structures with optical emission to 10 μm," *Appl. Phys. Lett.,* vol. 95, pp. 081906 (3 pp.), Aug 2009.

[23] G. C. Osbourn, "Strained-layer superlattices from lattice mismatched materials," *J. Appl. Phys.,* vol. 53, pp. 1586-9, Mar 1982.

[24] G. S. Lee, Y. Lo, Y. F. Lin, S. M. Bedair and W. D. Laidig, "Growth of $InAs_{1-x}Sb_x$ ($0<x<1$) and InSb-InAsSb superlattices by molecular beam epitaxy," *Appl. Phys. Lett.,* vol. 47, pp. 1219-21, Dec 1985.

[25] S. R. Kurtz, G. C. Osbourn, R. M. Biefeld and S. R. Lee, "Photoluminescence and the band structure of InAsSb strained-layer superlattices," *Appl. Phys. Lett.,* vol. 53, pp. 216-18, July 1988.

[26] S. R. Kurtz, L. R. Dawson, T. E. Zipperian and S. R. Lee, "Demonstration of an InAsSb strained-layer superlattice photodiode," *Appl. Phys. Lett.,* vol. 52, pp. 1581-3, May 1988.

[27] S.R. Kurtz, L.R. Dawson, R.M. Biefeld, T.E. Zipperian and I.J. Fritz, "Prototype InAsSb strained-layer superlattice photovoltaic and photoconductive infrared detectors," in *Electron Devices Meeting, 1988. IEDM '88. Technical Digest., International,* pp. 479-482, 1988.

[28] S. R. Kurtz, R. M. Biefeld and T. E. Zipperian, "MOCVD-grown InAsSb strained-layer superlattice infrared detectors with photoresponses 10 μm," *Semicond. Sci. Technol.*, vol. 5, pp. S24-6, 1990.

[29] D. H. Chow, R. H. Miles, J. R. Soderstrom and T. C. McGill, "Growth and characterization of InAs/$Ga_{1-x}In_xSb$ strained-layer superlattices," *Appl. Phys. Lett.,* vol. 56, pp. 1418-20, April 1990.

[30] R. M. Biefeld, K. C. Baucom and S. R. Kurtz, "The growth of $InAs_{1-x}Sb_x$/InAs strained-layer superlattices by metalorganic chemical vapor deposition," *J. Cryst. Growth,* vol. 137, pp. 231-234, 1994.

[31] Y.-H. Zhang, "Continuous wave operation of InAs/$InAs_xSb_{1-x}$ midinfrared lasers," *Appl. Phys. Lett.,* vol. 66, pp. 118-20, Jan 1995.

[32] M. J. Pullin, P. J. P. Tang, S. J. Chung, C. C. Phillips, R. A. Stradling, A. G. Norman, Y. B. Li and L. Hart, "300 K light emitting devices for the 3-10 μm band from arsenic rich InAs/$InAs_{1-x}Sb_x$ strained layer superlattices," in *Proceedings of*

Seventh International Conference on Narrow Gap Semiconductors 1995, pp. 8-12, Jan 1995.

[33] A. Y. Lew, E. T. Yu and Y. H. Zhang, "Atomic-scale structure of $InAs/InAs_{1-x}Sb_x$ superlattices grown by modulated molecular beam epitaxy," *J. Vac. Sci. Technol. B,* vol. 14 (4), pp. 2940-2943, July/Aug 1996.

[34] E. H. Steenbergen, Y. Huang, J.-H. Ryou, L. Ouyang, J. Li, D. J. Smith, R. D. Dupuis and Y.-H. Zhang, "Structural and optical characterization of type-II $InAs/InAs_{1-x}Sb_x$ superlattices grown by metalorganic chemical vapor depositio," *Appl. Phys. Lett.,* vol. 99, pp. 071111-3, Aug 2011.

[35] K. C. Hass and D. J. Kirill, "In(As,Sb) sawtooth doping superlattices for long wavelength infrared detection," *J. Appl. Phys.,* vol. 68, pp. 1923-6, Aug 1990.

[36] L. L. Chang, L. Esaki, W. E. Howard, R. Ludeke and G. Schul, "Structures grown by molecular beam epitaxy [GaAs and GaAs-$Ga_{1-x}Al_xAs$]," in *1973 Conference on Thin Film Phenomena*, pp. 655-62, 1973.

[37] G. C. Osbourn, "Novel material properties of strained-layer superlattices," *J. Vac. Sci. Technol. A,* vol. 3 (3), pp. 826-828, May/June 1985.

[38] G. Belenky, G. Kipshidze, D. Donetsky, S. P. Svensson, W. L. Sarney, H. Hier, L. Shterengas, D. Wang and Y. Lin. "Effects of carrier concentration and phonon energy on carrier lifetime in type-2 SLS and properties of $InAs_{1-x}Sb_x$ alloys". *Proc. SPIE 8012(1),* pp. 80120W. 2011. Available: http://dx.doi.org.ezproxy1.lib.asu.edu/doi/10.1117/12.883625.

[39] G. C. Osbourn, "Strained-layer superlattices: a brief review," *IEEE J. Quant. Electron.,* vol. QE-22, pp. 1677-81, 1986.

[40] J. W. Matthews and A. E. Blakeslee, "Defects in epitaxial multilayers. I. Misfit dislocations," *J. Cryst. Growth,* vol. 27, pp. 118-25, Dec 1974.

[41] S. Chadda, A. Datye and L. R. Dawson, "Microstructural evaluation of strained multilayer InAsSb/InSb infrared detectors by transmission electron microscopy," *J. Appl. Phys.,* vol. 73, pp. 4232-9, May 1993.

[42] W. Walukiewicz, "Defect reactions at metal-semiconductor and semiconductor-semiconductor interfaces," in *Chemistry and Defects in Semiconductor Heterostructures Symposium*, pp. 137-48, 1989.

[43] N. Ekins-Daukes, K. Kawaguchi and J. Zhang, "Strain-balanced criteria for multiple quantum well structures and its signature in X-ray rocking curves," *Crystal Growth & Design,* vol. 2, pp. 287-92, July 2002.

[44] F. Szmulowicz, E. R. Heller, K. Fisher and F. L. Madarasz, "Optimization of absorption in InAs/$In_xGa_{1-x}Sb$ superlattices for long-wavelength infrared detection," *Superlattices and Microstructures,* vol. 17, pp. 373-9, 1995.

[45] I. Vurgaftman, J. R. Meyer and L. Ram-Mohan, "Band parameters for III-V compound semiconductors and their alloys," *J. Appl. Phys.,* vol. 89, pp. 5815-75, June 2001.

[46] S. R. Kurtz and R. M. Biefeld, "Magnetophotoluminescence of biaxially compressed InAsSb quantum wells," *Appl. Phys. Lett.,* vol. 66, pp. 364-6, Jan 1995.

[47] S.-H. Wei and A. Zunger, "InAsSb/InAs: a type-I or a type-II band alignment," *Physical Review B (Condensed Matter),* vol. 52, pp. 12039-44, Oct 1995.

[48] P. J. P. Tang, M. J. Pullin, Y. B. Li, C. C. Phillips, R. A. Stradling, S. J. Chung, W. T. Yuen, L. Hart, D. J. Bain and I. Gaibraith, "A magneto-photoluminescence investigation of the band offset between InAs and arsenic-rich $InAs_{1-x}Sb_x$ alloys," *Appl. Phys. Lett.,* vol. 69, pp. 2501-3, Oct 1996.

[49] Y. B. Li, R. A. Stradling, A. G. Norman, P. J. P. Tang, S. J. Chung and C. C. Phillips, "Band offsets for $InAs_{1-x}Sb_x/InAs_{1-y}Sb_y$ strained layer superlattices derived from interband magneto-optical studies," in *Proceedings of 22nd International Conference on the Physics of Semiconductors*, pp. 1496-9, 1995.

[50] P.-W. Liu, G. Tsai, H. H. Lin, A. Krier, Q. D. Zhuang and M. Stone, "Photoluminescence and bowing parameters of InAsSb/InAs multiple quantum wells grown by molecular beam epitaxy," *Appl. Phys. Lett.,* vol. 89, pp. 201115-1, Nov 2006.

[51] C.-J. Wu, G. Tsai and H.-H. Lin, "Band alignment of $InAs_{1-x}Sb_x$ ($0.05<x<0.13$)/$InAs_{0.67}P_{0.23}Sb_{0.10}$ heterostructures," *Appl. Phys. Lett.,* vol. 94, pp. 211906 (3 pp.), May 2009.

[52] P. Bhattacharya, "Lattice-mismatched and pseudomorphic materials," in *Semiconductor Optoelectronic Devices*, 2nd ed, pp. 22-25,1997.

[53] R. People and J. C. Bean, "Calculation of critical layer thickness versus lattice mismatch for Ge_xSi_{1-x}/Si strained-layer heterostructures," *Appl. Phys. Lett.,* vol. 47, pp. 322-4, Aug 1985.

[54] J. R. Downes, D. J. Dunstan and D. A. Faux, "Numerical calculation of equilibrium critical thickness in strained-layer epitaxy," *Semicond. Sci. and Technol.,* vol. 9, pp. 1265-7, June 1994.

[55] J. R. Downes, D. J. Dunstan and D. A. Faux, "Analysis of the shortcomings of the Matthews-Blakeslee theory of critical thickness at higher strains," *Philosophical Magazine Letters,* vol. 76, pp. 77-81, Aug 1997.

[56] S.-L. Chuang, *Physics of Photonic Devices.* Hoboken, New Jersey: Wiley, 2009.

[57] Y. B. Li, D. J. Bain, L. Hart, M. Livingstone, C. M. Ciesla, M. J. Pullin, P. J. P. Tang, W. T. Yuen, I. Galbraith, C. C. Phillips, C. R. Pidgeon and R. A. Stadling, "Band alignments and offsets in In(As,Sb)/InAs superlattices," *Phys. Rev. B (Condensed Matter),* vol. 55, pp. 4589-95, Feb 1997.

[58] Y.-H. Zhang, R. H. Miles and D. H. Chow, "InAs-$InAs_xSb_{1-x}$ type-II superlattice midwave infrared lasers grown on InAs substrates," *IEEE Journal of Selected Topics in Quantum Electronics,* vol. 1, pp. 749-56, 06, 1995.

[59] Y.-H. Zhang, H. Q. Le, D. H. Chow and R. H. Miles, "Mid infrared lasers grown on InAs by modulated-molecular-beam-epitaxy," in *Proceedings of the International Conference on Narrow Gap Semiconductors*, J. L. Reno, Ed. London: Institute of Physics, pp. 36,1995.

[60] P. Christol, P. Bigenwald, A. Wilk, A. Joullie, O. Gilard, H. Carrere, F. Lozes-Dupuy, A. Behres, A. Stein, J. Kluth, K. Heime and E. M. Skouri, "InAs/InAs(P,Sb) quantum-well laser structure for the midwavelength infrared region," *IEE Proc.-Optoelectron.,* vol. 147, pp. 181-7, June 2000.

[61] P. J. P. Tang, M. J. Pullin, S. J. Chung, C. C. Phillips, R. A. Stradling, A. G. Norman, Y. B. Li and L. Hart, "4-11 μm Infrared emission and 300 K light emitting diodes from arsenic-rich $InAs_{1-x}Sb_x$ strained layer superlattices," *Semicond. Sci. and Technol.,* vol. 10, pp. 1177-1180, 1995.

[62] C. G. Van de Walle, "Band lineups and deformation potentials in the model-solid theory," *Phys. Rev. B (Condensed Matter),* vol. 39, pp. 1871-83, Jan 1989.

[63] A. Qteish and R. J. Needs, "Improved model-solid-theory calculations for valance-band offsets at semiconductor interfaces," *Phys. Rev. B (Condensed Matter),* vol. 45, pp. 1317-26, Jan 1992.

[64] J. C. Woolley and J. Warner, "Optical energy-gap variation in InAs-InSb alloys," *Can. J. Phys.,* vol. A2, pp. 1879-1885, Oct 1964.

[65] M. Y. Yen, B. F. Levine, C. G. Bethea, K. K. Choi and A. Y. Cho, "Molecular beam epitaxial growth and optical properties of $InAs_{1-x}Sb_x$ in 8-12 μm wavelength range," *Appl. Phys. Lett.,* vol. 50, pp. 927-9, April 1987.

[66] Z. M. Fang, K. Y. Ma, D. H. Jaw, R. M. Cohen and G. B. Stringfellow, "Photoluminescence of InSb, InAs, and InAsSb grown by organometallic vapor phase epitaxy," *J. Appl. Phys.,* vol. 67, pp. 7034-9, June 1990.

[67] H. H. Wieder and A. R. Clawson, "Photo-electronic properties of $InAs_{0.07}Sb_{0.93}$ films," *Thin Solid Films,* vol. 15, pp. 217-21, Feb 1973.

[68] M. Y. Yen, R. People, K. W. Wecht and A. Y. Cho, "Long-wavelength photoluminescence of $InAs_{1-x}Sb_x$ ($0<x<1$) grown by molecular beam epitaxy on (100) InAs," *Appl. Phys. Lett.,* vol. 52, pp. 489-91, Feb 1988.

[69] S. N. Smith, C. C. Phillips, R. H. Thomas, R. A. Stradling, I. T. Ferguson, A. G. Norman, B. N. Murdin and C. R. Pidgeon, "Interband magneto-optics of $InAs_{1-x}Sb_x$," *Semicond. Sci. and Technol.,* vol. 7, pp. 900-6, July 1992.

[70] G. Bastard, "Superlattice band structure in the envelope-function approximation," *Phys. Rev. B (Condensed Matter),* vol. 24, pp. 5693-7, Nov 1981.

[71] G. Bastard, "Theoretical investigations of superlattice band structure in the envelope-function approximation," *Phys. Rev. B (Condensed Matter),* vol. 25, pp. 7584-97, June 1982.

[72] R. A. Rosas, R. Riera, J. L. Marin and G. Campoy, "Electro-optical and transport properties of quasi-two-dimensional nanostructured materials," in *Handbook of Thin Film Materials*, H. S. Nalwa, Ed. San Diego, CA: Academic Press, pp. 208-222, 2002.

[73] G. Bastard, *Wave Mechanics Applied to Semiconductor Heterostructures*. France: Les Editions de Physique, 1988.

[74] C. Weisbuch and B. Vinter, *Quantum Semiconductor Structures: Fundamentals and Applications.* San Diego, CA: Academic Press, 1991.

[75] M. W. Prairie and R. M. Kolbas, "A general derivation of the density of states function for quantum wells and superlattices," *Superlattices and Microstructures,* vol. 7, pp. 269-77, 1990.

[76] R. M. Biefeld, S. R. Kurtz and S. A. Casalnuovo, "Reproducible growth of $InAs_xSb_{1-x}$/InSb strained-layer superlattice photodiodes by low pressure MOCVD," *J. Cryst. Growth,* vol. 124, pp. 401-8, 1992.

[77] Y. Huang, J.-H. Ryou, R. D. Dupuis, A. Petschke, M. Mandl and S.-L. Chuang, "InAs/GaSb type-II superlattice structures and photodiodes grown by metalorganic chemical vapor deposition," *Appl. Phys. Lett.,* vol. 96, pp. 251107 (3 pp.), June 2010.

[78] H. Y. Fan, "Temperature dependence of the energy gap in semiconductors," *Phys. Rev.,* vol. 82, pp. 900-905, June 1951.

[79] B. Bansal, V. K. Dixit, V. Venkataraman and H. L. Bhat, "Temperature dependence of the energy gap and free carrier absorption in bulk $InAs_{0.05}Sb_{0.95}$ single crystals," *Appl. Phys. Lett.,* vol. 82, pp. 4720-4722, 2003.

[80] I. A. Vainshtein, A. F. Zatsepin and V. S. Kortov, "Applicability of the empirical Varshni relation for the temperature dependence of the width of the band gap," *Physics of the Solid State,* vol. 41, pp. 905-8, June 1999.

[81] W. Martienssen and H. Warlimont, Eds., *Springer Handbook of Condensed Matter and Materials Data.* Berlin Heidelberg: Springer, 2005.

[82] B. C. Connelly, G. D. Metcalfe, H. Shen and M. Wraback, "Direct minority carrier lifetime measurements and recombination mechanisms in long-wave infrared type II superlattices using time-resolved photoluminescence," *Appl. Phys. Lett.,* vol. 97, pp. 251117 (3 pp.), Dec, 2010.

[83] S. Bandara, P. Maloney, N. Baril, J. Pellegrino and M. Tidrow, "Performance of InAs/GaSb superlattice infrared detectors and dependence on minority carrier lifetime," *Infrared Phys. Technol.,* vol. 54, pp. 263-6, June 2011.

[84] S. P. Svensson, D. Donetsky, D. Wang, P. Maloney and G. Belenky, "Carrier lifetime measurements in InAs/GaSb strained layer superlattice structures," *Proc. SPIE 7660,* pp. 76601V (6 pp.), 2010.

[85] S. R. Kurtz, L. R. Dawson, R. M. Biefeld, I. J. Fritz and T. E. Zipperian, "Long-wavelength, InAsSb strained-layer superlattice photovoltaic infrared detectors," *IEEE Electron Device Lett.,* vol. 10, pp. 150-2, April 1989.

[86] S. R. Kurtz, R. M. Biefeld, A. A. Allerman, A. J. Howard, M. H. Crawford and M. W. Pelczynski, "Pseudomorphic InAsSb multiple quantum well injection laser emitting at 3.5 μm," *Appl. Phys. Lett.,* vol. 68, pp. 1332-4, Mar 1996.

[87] H. Miyoshi and Y. Horikoshi, "Substrate lattice constant effect on the miscibility gap of MBE grown InAsSb," *J. Cryst. Growth,* vol. 227-228, pp. 571-6, 2001.

[88] H. Miyoshi, R. Suzuki, H. Amano and Y. Horikoshi, "Sb surface segregation effect on the phase separation of MBE grown InAsSb," *J. Cryst. Growth,* vol. 237-239, pp. 1519-24, April 2002.

[89] L. Ouyang, E. H. Steenbergen, Y.-H. Zhang, K. Nunna, D. L. Huffaker and D. J. Smith, "Structural properties of $InAs/InAs_{1-x}Sb_x$ type-II superlattices grown

by molecular beam epitaxy," *J. Vac. Sci. Technol. B,* vol. 30, pp. 02B106, March 2012.

[90] J. Steinshnider, J. Harper, M. Weimer, C. -. Lin, S. S. Pei and D. H. Chow, "Origin of antimony segregation in GaInSb/InAs strained-layer superlattices," *Phys. Rev. Lett.,* vol. 85, pp. 4562-5, Nov 2000.

[91] B. Ullrich and G. J. Brown, "Phase sensitive detection of photoluminescence with fourier transform spectroscopy," *Rev. Sci. Instrum.*, vol. 83, pp. 016105 (3 pp.), 2012.

[92] A. R. Reisinger, R. N. Roberts, S. R. Chinn and Myers,T.H.,,II, "Photoluminescence of infrared-sensing materials using a FTIR spectrometer," *Rev. Sci. Instrum.,* vol. 60, pp. 82-6, Jan 1989.

[93] C. R. Nave. HyperPhysics : Planck radiation formula. 2010. Available: http://hyperphysics.phy-astr.gsu.edu/hbase/mod6.html#c3.

[94] P. R. Griffiths and J. A. de Haseth, *Fourier Transform Infrared Spectroscopy*. Hoboken, New Jersey: Wiley, 2007.

[95] Mathworks. Fmincon. 2011. Available: http://www.mathworks.com/help/toolbox/optim/ug/fmincon.html.

[96] D. Donetsky, S. P. Svensson, L. E. Vorobjev and G. Belenky, "Carrier lifetime measurements in short-period InAs/GaSb strained-layer superlattice structures," *Appl. Phys. Lett.,* vol. 95, pp. 212104 (3 pp.), Nov 2009.

[97] J. Pellegrino and R. Dewames, "Minority carrier lifetime characteristics in type II InAs/GaSb LWIR superlattice n^+p^+ photodiodes," *Proc. SPIE 7298,* pp. 72981U (10 pp.), 2009.

[98] B. C. Connelly, G. D. Metcalfe, H. Shen and M. Wraback. "Study of recombination mechanisms limiting the performance of Sb-based III-V type-II superlattices for infrared detectors", *Proc. SPIE 8155(1),* pp. 81550L. 2011.

[99] S. P. Svensson, D. Donetsky, D. Wang, H. Hier, F. J. Crowne and G. Belenky, "Growth of type II strained layer superlattice, bulk InAs and GaSb materials for minority lifetime characterization," *J. Cryst. Growth,* vol. 334, pp. 103-107, 2011.

[100] S. Bandara, P. Maloney, N. Baril, J. Pellegrino and M. Tidrow, "Doping dependence of minority carrier lifetime in long-wave Sb-based type II superlattice infrared detector materials," *Optical Engineering,* vol. 50, pp. 061015 (5 pp.), June 2011.

[101] A. Rakovska, V. Berger, X. Marcadet, G. Glastre and B. Vinter, "Non-cryogenic quantum detection in the mid-IR using InAsSb photovoltaic structures," *Proc. SPIE 4130,* pp. 537-46, 2000.

[102] R. F. Pierret, "Carrier lifetimes," in *Advanced Semiconductor Fundamentals*, Second ed., Prentice Hall, pp. 145-146, 2002.

[103] A. Rogalski, K. Adamiec and J. Rutkowski, "Generation-recombination processes: Carrier lifetime," in *Narrow-Gap Semiconductor Photodiodes,* Bellingham, Washington: SPIE - The International Society for Optical Engineering, pp. 83, 2000.

[104] J. S. Blakemore, "Semiconductor statistics," in *International Series of Monographs on Semiconductors*, H. K. Henisch, Ed. London: Pergamon Press, 1962.

[105] J. R. Dixon and J. M. Ellis, "Optical properties of n-type indium arsenide in the fundamental absorption edge region," *Physical Review,* vol. 123, pp. 1560-1566, 1961.

[106] J. D. Vincent, *Fundamentals of Infrared Detector Operation and Testing.* New York: Wiley, 1990.

[107] R. K. Ahrenkiel, *Semiconductors and Semimetals*, R. K. Ahrenkiel and M. S. Lundstrom, Eds. New York: Academic, pp. 39-150, 1993.

[108] C. L. Canedy, W. W. Bewley, C. S. Kim, M. Kim, I. Vurgaftman and J. R. Meyer, "Dependence of type II "W" mid-infrared photoluminescence and lasing properties on growth conditions," *J. Appl. Phys.,* vol. 94, pp. 1347-55, Aug 2003.

[109] F. Daiminger, A. F. Dite, E. Tournie, K. Ploog and A. Forchel, "Time-resolved investigations of excitonic recombination in highly strained InAs/$Al_{0.48}In_{0.52}As$ quantum wells," *J. Appl. Phys.,* vol. 76, pp. 618-20, July 1994.

[110] G. Rajanna, W. Feng, S. Sohal, V. V. Kuryatkov, S. A. Nikishin, A. A. Bernussi and M. Holtz, "Temperature and excitation intensity dependence of photoluminescence in AlGaN quantum wells with mixed two-dimensional and three-dimensional morphology," *J. Appl. Phys.,* vol. 110, pp. 073512 (7 pp.), Oct 2011.

[111] Z. Yang, L. Li, Z. Zuo and J. L. Liu, "Temperature-dependent photoluminescence of CdZnO thin films grown by molecular-beam epitaxy," *J. Cryst. Growth,* vol. 312, pp. 68-72, Dec 2009.

[112] M. A. Marciniak, R. L. Hengehold, Y. K. Yeo and G. W. Turner, "Optical characterization of molecular beam epitaxially grown InAsSb nearly lattice matched to GaSb," *J. Appl. Phys.,* vol. 84, pp. 480-8, July 1998.

[113] A. V. Filinov, F. M. Peeters, C. Riva, Y. E. Lozovik and M. Bonitz, "Exciton molecules in quantum wells: Influence of the well width fluctuations," *Few-Body Systems*, vol. 34, pp. 149-54, 2004.

[114] F. Saidi, F. Hassen, H. Maaref, L. Auvray, H. Dumont and Y. Monteil, "Excitons localization effects in GaAsN/GaAs epilayers grown by MOCVD," *Mater. Sci. Eng. C*, vol. 21, pp. 245-9, 2002.

[115] C. M. Ciesla, B. N. Murdin, C. R. Pidgeon, R. A. Stradling, C. C. Phillips, M. Livingstone, I. Galbraith, D. A. Jaroszynski, C. J. G. M. Langerak, P. J. P. Tang and M. J. Pullin, "Suppression of auger recombination in arsenic-rich $InAs_{1-x}Sb_x$ strained layer superlattices," *J. Appl. Phys.*, vol. 80 (5), pp. 2994-7, 1996.

[116] L. R. Dawson, "Molecular beam epitaxial growth of InAsSb alloys and superlattices," *J. Vac. Sci. Technol. B*, vol. 4 (2), pp. 598-9, 1986.

[117] S. R. Kurtz, G. C. Osbourn, R. M. Biefeld, L. R. Dawson and H. J. Stein, "Extended infrared response of InAsSb strained-layer superlattices," *Appl. Phys. Lett.,* vol. 52, pp. 831-3, Mar 1988.

[118] S. R. Kurtz, L. R. Dawson, T. E. Zipperian and R. D. Whaley J., "High-detectivity ($>1x10^{10}$ cm√Hz/W), InAsSb strained-layer superlattice, photovoltaic infrared detector," *IEEE Electron Device Lett.,* vol. 11, pp. 54-6, Jan 1990.

[119] B. Lane, D. Wu, A. Rybaltowski, H. Yi, J. Diaz and M. Razeghi, "Compressively strained multiple quantum well InAsSb lasers emitting at 3.6 μm grown by metal-organic chemical vapor deposition," *Appl. Phys. Lett.,* vol. 70, pp. 443-5, Jan 1997.

[120] A. A. Allerman, S. R. Kurtz, R. M. Biefeld, K. C. Baucom and J. H. Burkhart, "Development of InAsSb-based light emitting diodes for chemical sensing systems," *Proc. SPIE*, vol. 3279, pp. 126-33, 1998.

[121] R. M. Biefeld, A. A. Allerman and S. R. Kurtz, "Recent advances in mid-infrared (3-6 μm) emitters," *Mater. Sci. Eng. B*, vol. B51 (1-3), pp. 1-8, 1998.

[122] P. J. P. Tang, H. Hardaway, J. Heber, C. C. Phillips, M. J. Pullin, R. A. Stradling, W. T. Yuen and L. Hart, "Efficient 300 K light-emitting diodes at ~5 and ~8 μm from $InAs/InAs_{1-x}Sb_x$ single quantum wells," *Appl. Phys. Lett.,* vol. 72, pp. 3473-5, June 1998.

[123] C. Phillips, H. Hardaway, J. Heber, P. Moeck, M. Pullin, P. Tang and P. Yuen, "Recent advances in In(As,Sb) SLS and QW LEDs for the 3-10 micron region," *Proc. SPIE,*, vol. 3279, pp. 154-60, 1998.

[124] H. Hardaway, J. Heber, P. Mock, M. Pullin, T. Stradling, P. Tang and C. Phillips, "Optical studies of InAs/In(As,Sb) single quantum well (SQW) and strained-layer superlattice (SLS) LED's for the mid-infrared (MIR) region," *Proc SPIE,* vol. 3621, pp. 124-133, 1999.

[125] C. Van Hoof, S. Nemeth, B. Grieten, K. Dessein, J. Genoe, P. Merken, G. Borghs, F. Fuchs and J. Wagner, "Mid-infrared LEDs using $InAs_{0.71}Sb_{0.29}$/InAs/$Al_{0.25}In_{0.75}As$/InAs strained-layer superlattice active layers," in *Second International Conference on Advances Semiconductor Devices and Microsystems*, pp. 287-90, 1998.

[126] A. Behres, D. Puttjer and K. Heime, "Low-pressure metal organic vapour-phase epitaxy and characterization of strained InAs(P)/InAsSb superlattices for infrared emitters," *J. Crys. Growth*, vol. 195, pp. 373-7, 1998.

[127] M. J. Pullin, H. R. Hardaway, J. D. Heber, C. C. Phillips, W. T. Yuen, R. A. Stradling and P. Moeck, "Room-temperature InAsSb strained-layer superlattice light-emitting diodes at λ=4.2 μm with AlSb barriers for improved carrier confinement," *Appl. Phys. Lett.,* vol. 74, pp. 2384-6, April 1999.

[128] A. Wilk, F. Genty, B. Fraisse, G. Boissier, P. Grech, M. El Gazouli, P. Christol, J. Oswald, T. Simecek, E. Hulicius and A. Joullie, "MBE growth of InAs/InAsSb/AlAsSb structures for mid-infrared lasers," *J. Cryst. Growth,* vol. 223, pp. 341-8, Mar 2001.

[129] S. R. Kurtz and R. M. Biefeld, "Infrared magneto-optical and photoluminescence studies of the electronic properties of In(As,Sb) strained-layer superlattices," *Phys. Rev. B (Condensed Matter),* vol. 44, pp. 1143-9, July 1991.

[130] Y. Tsou, A. Ichii and E. M. Garmire, "Improving InAs double heterostructure lasers with better confinement," *IEEE J. Quant. Electron.,* vol. 28, pp. 1261-8, May 1992.

[131] R. H. Miles, D. H. Chow, J. N. Schulman and T. C. McGill, "Infrared optical characterization of InAs/$Ga_{1-x}In_xSb$ superlattices," *Appl. Phys. Lett.,* vol. 57, pp. 801-3, Aug 1990.

[132] L. Liu, G. S. Lee and A. H. Marshak, "Band structure of InAsSb strained-layer superlattices," *J. Appl. Phys.,* vol. 71, pp. 1842-5, Feb 1992.

[133] P. J. P. Tang, M. J. Pullin, S. J. Chung, C. C. Phillips, R. A. Stradling, A. G. Norman, Y. B. Li and L. Hart, "Photo- and electro-luminescence studies of uncooled arsenic rich InAsSb strained layer superlattice light emitting diodes for the 4-12 μm band," *Proc. SPIE*, vol. 2397, pp. 389-98, 1995.

[134] Ioffe Physico-Technical Institute. Semiconductors on NSM: InAs, InSb, InAsSb. *2010*2001. Available: http://www.ioffe.ru/SVA/NSM/Semicond/index.html; http://www.ioffe.ru/SVA/NSM/Semicond/InAs/basic.html; http://www.ioffe.ru/SVA/NSM/Semicond/InSb/basic.html; http://www.ioffe.ru/SVA/NSM/Semicond/InAsSb/basic.html.

[135] S. Ben Rejeb, M. Debbichi, M. Said, A. Gassenq, E. Tournie and P. Christol, "Modelling of an InAs/GaSb/InSb short-period superlattice laser diode for mid-infrared emission by the k.p method," *J. Phys. D,* vol. 43, pp. 325102 (7 pp.), Aug 2010.

APPENDIX A

REVIEW OF PREVIOUSLY STUDIED $InAs_{1-y}Sb_y/InAs_{1-x}Sb_x$ SUPERLATTICE STRUCTURES IN THE LITERATURE

Year	Method	Substrate	Buffer	SL Layer 1	SL Layer 2	Results	Measurement	Reference
1985	MBE	GaAs 350℃		InSb 50 Å	$InAs_{0.26}Sb_{0.74}$ 100 Å	90 periods 1.5 μm thick	XRD, Electron microprobe	[24]
1986 1987		InSb 450℃		$InAs_{0.1}Sb_{0.9}$ 100 Å	$InAs_{0.3}Sb_{0.7}$ 100 Å	Homogenized, no SL	XRD, He backscattering	[116]
1986 1987	MBE MOCVD	InSb 400℃	$InAs_{0.3}Sb_{0.7}$ 500 nm	$InAs_{0.2}Sb_{0.8}$ 200 Å	$InAs_{0.4}Sb_{0.6}$ 200 Å	3 satellite peaks, dislocations	XRD, TEM	[8, 116]
1986 1987	MBE MOCVD	InSb	$InAs_{0.1}Sb_{0.9}$	InSb 190 Å	$InAs_{0.2}Sb_{0.8}$ 190 Å	no dislocations, microcracks		[8, 116]
1987	MBE MOCVD	InSb	$InAs_{1-x}Sb_x$ Step-graded x=0.96, 0.93, 0.90 ~1000 Å	InSb 200 Å	$InAs_{0.2}Sb_{0.8}$ 200 Å	no dislocations, no microcracks	TEM	[8]
1988	MOCVD	InSb	$InAs_{1-x}Sb_x$ linearly composition-graded	InSb 210 Å	$InAs_{0.13}Sb_{0.87}$ 210 Å	1.0 μm thick	TEM, XRD	[117]
				InSb 210 Å	$InAs_{0.13}Sb_{0.87}$ 210 Å	5.0 μm thick λ_g ~ 8.7 μm	XRD, Infrared transmission	
				InSb 260 Å	$InAs_{0.13}Sb_{0.87}$ 260 Å	5.0 μm thick λ_g ~ 8.0 μm		
				InSb 106 Å	$InAs_{0.13}Sb_{0.87}$ 106 Å	5.0 μm thick λ_g ~ 10.5 μm	Infrared transmission	
	MBE		Dislocated $InAs_{0.35}Sb_{0.65}$, Layers with lower x_{As}	$InAs_{0.06}Sb_{0.94}$ 200 Å	$InAs_{0.3}Sb_{0.7}$ 200 Å			
				$InAs_{0.12}Sb_{0.88}$ 400 Å	$InAs_{0.4}Sb_{0.6}$ 200 Å	λ_g ~ 10.7 μm		
1988	MBE	p+ InSb	p- $InAs_{1-x}Sb_x$ composition-graded 500 nm	InSb 130 Å	$InAs_{0.09}Sb_{0.91}$ 130 Å	λ_g ~ 8.0 μm	Current Responsivity, Absorption	nip diodes [26, 27]
				InSb 150 Å	$InAs_{0.15}Sb_{0.85}$ 150 Å	λ_g ~ 10.4 μm		

Year	Method	Substrate	Buffer	SL Layer 1	SL Layer 2	Results	Measurement	Reference
1988	MOCVD	p InSb		InSb 210 Å	$InAs_{0.11}Sb_{0.89}$ 210 Å	$\lambda_g \sim 9.0$ µm	Current Responsivity	2-layers per SL period, photoconductive [27]
				InSb\ $InAs_{0.07}Sb_{0.93}$ 185 Å	$InAs_{0.11}Sb_{0.89}$ \ $InAs_{0.07}Sb_{0.93}$ 185 Å	$\lambda_g \sim 9.0$ µm		4-layers per SL period, higher responsivity than 2-layers per period, photoconductive [27]
1989	MBE	p+, p-InSb	$InAs_{1-x}Sb_x$ composition-graded	InSb 150 Å	$InAs_{0.15}Sb_{0.85}$ 150 Å	$\lambda_g \sim 10.7$ µm 4.5 µm thick	I-V, Responsivity, Absorption (p-sub), noise	nip diodes [85]
				InSb 76 Å	$InAs_{0.18}Sb_{0.82}$ 76 Å	$\lambda_g \sim <10$ µm 4.5 µm thick		
	MOVCD	p+, p-InSb		InSb 102 Å	$InAs_{0.17}Sb_{0.83}$ 102 Å	$\lambda_g \sim >10$ µm 1.0 µm thick		nip diodes [28, 86]
1990	MBE	n-InSb	$In_xGa_{1-x}Sb$ x=1.0-0.9 composition-graded	InSb 150 Å	$InAs_{0.15}Sb_{0.85}$ 150 Å	$E_g \sim 119$ meV 4.5 µm thick	I-V, C-V, Responsivity	pin diode [118]
1990	MOCVD			InSb 230 Å	$InAs_{0.19}Sb_{0.81}$ 230 Å	$\lambda_g \sim 14.4$ µm	Current responsivity	photoconductive [28]
1992	MOCVD	p-InSb	Zn-doped 4-0.6 µm layers step-graded to $InAs_{0.12}Sb_{0.82}$	InSb 97 Å	$InAs_{0.18}Sb_{0.82}$ 97 Å	$\lambda_g \sim 10$ µm	I-V, Current Responsivity, PL	90 periods undoped, 60 periods Sn-doped diode [77]

Year	Method	Substrate	Buffer	SL Layer 1	SL Layer 2	Results	Measurement	Reference
1992	MBE	GaSb	$Al_{0.7}In_{0.3}Sb$/AlSb SLS graded layer thicknesses	$InAs_{0.62}Sb_{0.38}$ 83 Å	$InAs_{0.54}Sb_{0.46}$ 83 Å	$\lambda_g \sim 10.6$ µm, 4.0 µm thick	XRD, TEM, PL, Photoconductance	Lower growth temp of 425℃ to promote ordering [21]
1993	MBE	InSb 425℃	3 composition graded buffer schemes	InSb 110 Å	$InAs_{0.15}Sb_{0.85}$ 110 Å		TEM	pin [41]
1994	MOCVD	InAs 475-525℃		InAs	$InAs_{1-x}Sb_x$ $x < 0.20$	PL peaks ~ 0.23 - 0.31 eV	XRD, PL, Absorption, dislocations, cross-hatch	[30]
1995	MMBE	InAs 480-500 ℃	InAs 200 Å	InAs 77 Å	$InAs_{0.93}Sb_{0.07}$ 23 Å	$\lambda_g \sim 3.3$ µm at 95 K, 30 nm thick	EL	[31, 58]
1995	MBE	GaAs	1 µm $InAs_{0.80}Sb_{0.20}$	InAs 107.5 Å	$InAs_{0.61}Sb_{0.39}$ 107.5 Å	$\lambda_g \sim 10.5$µm, 2.0 µm thick	XRD, PL, Magneto-transmission	[32, 57, 61]
			1 µm $InAs_{0.84}Sb_{0.16}$	InAs 100 Å	$InAs_{0.68}Sb_{0.32}$ 100 Å	$\lambda_g \sim 8.7$ µm, 2.0 µm thick		
			1 µm $InAs_{0.86}Sb_{0.14}$	InAs 117.5 Å	$InAs_{0.73}Sb_{0.27}$ 117.5 Å	$\lambda_g \sim 7$ µm, 2.0 µm thick		
			1 µm $InAs_{0.93}Sb_{0.07}$	InAs 80 Å	$InAs_{0.86}Sb_{0.14}$ 80 Å	$\lambda_g \sim 4$ µm, 2.0 µm thick		
			1 µm $InAs_{0.93}Sb_{0.07}$	InAs 124 Å	$InAs_{0.86}Sb_{0.14}$ 124 Å	$\lambda_g \sim 4$ µm, 2.0 µm thick		
1995	MBE	GaAs	1 µm $InAs_{0.86}Sb_{0.14}$	InAs 102 Å	$InAs_{0.73}Sb_{0.27}$ 102 Å	$\lambda_g \sim 7$ µm, 2.0 µm thick	EL	pin LED, SL the i-region [32]
			1 µm $InAs_{0.95}Sb_{0.05}$	InAs 121 Å	$InAs_{0.9}Sb_{0.1}$ 121 Å	$\lambda_g \sim 3.8$ µm, 2.0 µm thick	EL	
1995	MOCVD	InAs		InAs 500 Å	$InAs_{0.91}Sb_{0.09}$ 318, 159, 106, 53 Å MQW	4 K PL peaks 310, 320, 335, 365 meV	XRD, Magneto-PL at 4 K	[46]

Year	Method	Substrate	Buffer	SL Layer 1	SL Layer 2	Results	Measurement	Reference
1996	MBE	p-GaSb	GaSb	InAs 172Å	$InAs_{0.76}Sb_{0.24}$ 52 Å 4 periods of InAs 7.8 Å InSb 5.2 Å	Ordered $InAs_{1-x}Sb_x$ alloys	STM	[33]
1996	MOCVD	n-InAs	n-$InP_{0.69}Sb_{0.31}$ 3 μm	InAs 450Å	$InAs_{0.94}Sb_{0.06}$ 90 Å	77 K lasing 3.52-3.57 μm	XRD, Lasing at 14 - 135 K	[86]
1996	MBE	InAs		InAs 475 Å	$InAs_{0.865}Sb_{0.135}$ 50, 101, 151 Å MQW	4 K PL peaks 291, 262 meV	XRD, Magneto-PL at 4 K	[48]
1997	MBE	GaAs 450℃	GaAs 300 nm, InAsSb of avg SL composition, 1 μm	InAs 124 Å InAs 117.5 Å InAs 100 Å InAs 107.5 Å	$InAs_{0.86}Sb_{0.14}$ 124 Å $InAs_{0.73}Sb_{0.27}$ 117.5 Å $InAs_{0.73}Sb_{0.32}$ 100 Å $InAs_{0.61}Sb_{0.39}$ 107.5 Å	2 μm thick SL 303 meV 2 μm thick SL 173 meV 2 μm thick SL 146 meV 2 μm thick SL 132 meV	Magneto-T at 4 K	[57]
1997	MOCVD	n+ InAs 490 ℃		InAs 500Å	$InAs_{0.94}Sb_{0.06}$ 100 Å	10 periods 3.65 μm lasing at 90 K	MQWs	[119]
1998	MOCVD			InAs 450Å	$InAs_{1-x}Sb_x$ x = 0.04 – 0.14 80 Å	10 periods 3 – 4.5 μm	PL	[120]
1998	MCVD	n-InAs 500 ℃		InAs 450Å	$InAs_{1-x}Sb_x$ x = 0.11 – 0.20 90 Å	10 periods 4 – 6 μm	PL	[121]

Year	Method	Substrate	Buffer	SL Layer 1	SL Layer 2	Results	Measurement	Reference
1998	MBE	p-InAs	p+ InAs 1 μm	InAs 500 nm	$InAs_{0.84}Sb_{0.16}$ 160 Å	SQW 5.3 μm	LED	[122-124]
				InAs 500 nm	$InAs_{0.74}Sb_{0.26}$ 160 Å	SQW 8 μm	LED	
1998	MBE	p-InAs		InAs 120 nm	$InAs_{0.875}Sb_{0.125}$ 120 Å	AlSb barrier	LED, negative luminescence	[123, 124]
1998				InAs 0, 30, 70, 120Å	$InAs_{0.90}Sb_{0.10}$ 25 Å	30 periods, $In_{0.85}Al_{0.15}As$ 25 Å PL peaks 2.79-3.84 μm	PL at 10 K	[125]
				InAs 125 Å	$InAs_{0.71}Sb_{0.29}$ 25 Å	PL peak 4.77 μm	LED	
1998	MOVPE	InAs	InAs	InAs 500Å	$InAs_{0.943}Sb_{0.057}$ 100 Å	10 periods	XRD, PL	[126]
				InAs 500Å	$InAs_{0.88}Sb_{0.12}$ 100 Å	10 periods		
				$InAs_{0.947}P_{0.053}$ 500Å	$InAs_{0.86}Sb_{0.14}$ 100 Å	10 periods 3.95 μm		
1999	MBE	p+ InAs 465 ℃		InAs 120 Å	$InAs_{0.918}Sb_{0.082}$ 120 Å	79 % relaxed PL 342.5 meV	EL at 20 K	[127]
				InAs 120 Å	$InAs_{0.914}Sb_{0.086}$ 120 Å	74 % relaxed PL 341 meV		

Year	Method	Substrate	Buffer	SL Layer 1	SL Layer 2	Results	Measurement	Reference
2000	MOVPE	InAs 570℃		$InAs_{0.90}Sb_{0.10}$ 100 Å $InAs_{0.87}Sb_{0.13}$ 100 Å $InAs_{0.855}Sb_{0.145}$ 100 Å $InAs_{0.85}Sb_{0.15}$ 100 Å $InAs_{0.835}Sb_{0.165}$ 100 Å	$InAs_{0.485}P_{0.37}Sb_{0.115}$ 300 Å $InAs_{0.31}P_{0.48}Sb_{0.21}$ 300 Å $InAs_{0.29}P_{0.50}Sb_{0.21}$ 300 Å $InAs_{0.275}P_{0.51}Sb_{0.215}$ 300 Å $InAs_{0.25}P_{0.53}Sb_{0.22}$ 300 Å	3.3 – 3.78 μm	20 K PL peaks	[60] 10 QWs
2001	MBE	InAs 420℃	$AlAs_{0.16}Sb_{0.84}$ 1-2 μm	InAs 200 Å InAs 200 Å	$InAs_{0.92}Sb_{0.08}$ 50 Å $InAs_{0.94}Sb_{0.06}$ 50 Å	3.5 μm at 90 K lasing 15 periods 3.25 μm at 7K 6 meV FWHM	PL, XRD	[128]
2006	MBE	n^+ InAs	InAs 1000 Å	InAs 500 Å	$InAs_{0.935}Sb_{0.065}$ 70 Å $InAs_{0.915}Sb_{0.085}$ 70 Å $InAs_{0.905}Sb_{0.095}$ 70 Å $InAs_{0.895}Sb_{0.105}$ 70 Å	Type-II alignment for InAs/InAsSb with electrons in InAs layer, 60% bowing in valence band	PL 4 K	[50] 7 MQWs

Year	Method	Substrate	Buffer	SL Layer 1	SL Layer 2	Results	Measurement	Reference
2006	MBE	n^+ InAs	InAs 1000 Å	InAs 500 Å	$InAs_{0.88}Sb_{0.12}$ 70 Å $InAs_{0.863}Sb_{0.137}$ 70 Å $InAs_{0.83}Sb_{0.17}$ 70 Å	Type-II alignment for InAs/InAsSb with electrons in InAs layer, 60% bowing in valence band	PL 4 K	[50] 7 MQWs
2009	MBE	n^+ InAs	InAs 950 Å InAsPSb 4750 Å	$InAs_{0.95}Sb_{0.05}$ 87 Å $InAs_{0.92}Sb_{0.08}$ 97 Å $InAs_{0.92}Sb_{0.08}$ 103 Å $InAs_{0.91}Sb_{0.09}$ 95 Å $InAs_{0.91}Sb_{0.09}$ 96 Å $InAs_{0.87}Sb_{0.13}$ 95 Å	$InAs_{0.67}P_{0.23}Sb_{0.10}$ 218 Å 243 Å 258 Å 238 Å 240 Å 238 Å	Type-I alignment for InAsSb/InAsPSb Type-II alignment for InAs/InAsSb with electrons in InAs layer, 65% bowing in valence band	PL 10-300 K	[51] 5 MQWs
2009	OMVPE	GaSb 500℃	$InAs_{0.91}Sb_{0.09}$ 50 nm	InAs 200 Å InAs 220 Å InAs 200 Å InAs 200 Å	$InAs_{0.862}Sb_{0.138}$ 200 Å $InAs_{0.843}Sb_{0.157}$ 220 Å $InAs_{0.832}Sb_{0.168}$ 210 Å $InAs_{0.826}Sb_{0.174}$ 200 Å	5 μm	PL 4 K	[22] 6 MQWs

Year	Method	Substrate	Buffer	SL Layer 1	SL Layer 2	Results	Measurement	Reference
2009	OMVPE	GaSb 500℃	$InAs_{0.91}Sb_{0.09}$ 50 nm	InAs 200 Å	$InAs_{0.792}Sb_{0.208}$ 210 Å	5 μm	PL 4 K	[22] 6 MQWs
				InAs 260 Å	$InAs_{0.733}Sb_{0.267}$ 130 Å	10 μm		

APPENDIX B

SUMMARY OF DIFFERENT BAND ALIGNMENTS AND BAND OFFSETS REPORTED FOR $InAs_{1-y}Sb_y/InAs_{1-x}Sb_x$

Valence Band Offset (VBO) (eV)	Measurement Type	Reference
	InSb/InAs	
0.410 ± 0.1		[25] $InAs_{1-x}Sb_x$ unstrained valence band energy = $(0.41 \pm 0.1)x$ for $InAs_{1-x}Sb_x$/InSb at 77 K.
Unstrained; 0.360 ± 0.04	PL, magneto-transmission	[21, 129] $InAs_{1-x}Sb_x$ unstrained valence band energy = $(0.36 \pm 0.04)x$.
0.43	Empirical estimation	[130]
0.61	PL, Photo-conductance	[58, 131]
Unstrained; 0.50	Calculation	[47]
Strained on InAs substrate; 0.91	Calculation	[47]
Substrate of average lattice constant between InAs and InSb; 0.57	Calculation	[47]
Strained on InSb substrate; 0.25 (InAs has $-E_g$)	Calculation	[47]
Unstrained; 0.84, 0.36	Magneto-transmission	[49]
0.59	Recommendation	[45]
	$InAs_{1-x}Sb_x$/InSb	
$InAs_{1-x}Sb_x/InAs_{0.39}Sb_{0.61}$ CBO=0.04·(x-0.61); CBO=0.21·(x-0.61)		[6]
Strained $InAs_{0.13}Sb_{0.87}$/InSb Heavy hole = 0.084; Light hole = 0.023; CBO = 0.153		[25] $InAs_{1-x}Sb_x$ unstrained valence band energy=$(0.41 \pm 0.1)x$ eV for $InAs_{1-x}Sb_x$/InSb at 77 K.
Type-II for $x > 0.6$		[25, 27, 117]
Assumed Type-II VBO proportional to x		[28]
Unstrained; 0.047, x = 0.13; 0.029, $InAs_{0.62}Sb_{0.38}/InAs_{0.54}Sb_{0.46}$	PL, magneto-transmission	[21, 129]

Valence Band Offset (VBO) (eV)	Measurement Type	Reference
VBO = -0.667·x + 0.65 CBO = -1.4·x + 1.38	Calculation at 77 K	[132] Compared to two x values experimental data
Unstrained on InSb; 0.05 for x = 0.9	Calculation	[47]
Strained on InSb; 0.025 for x = 0.9	Calculation	[47]
VBO = 0.360Δx for $InAs_{0.18}Sb_{0.82}/InAs_{0.11}Sb_{0.89}$	Magneto-transmission	[49]
	$InAs/InAs_{1-x}Sb_x$	
Unstrained on InSb; 0.05 for x = 0.1	Calculation	[47]
Strained on InAs; 0.91 for x = 0.1	Calculation	[47]
Type-IIa; VBO = 830 x	PL	[133]
Type-I Strained 4 K; $InAs/InAs_{0.91}Sb_{0.09}$ CBO = 0.074	PL	[46]
Unstrained 0.274 for x = 0.32 VBO = 0.840x	Magneto-transmission	[49]
Unstrained Type-IIa, for x = 0.39 VBO = 710x for x = 0.32 VBO = 830x for x = 0.27 VBO = 790x for x = 0.14 VBO = 880x Unstrained Type-IIb, for x = 0.39 VBO = 631x for x = 0.32 VBO = 780x for x = 0.27 VBO = 620x for x = 0.14 VBO = 940x	PL	[32]
Unstrained, Type-IIa, x = 0.32, VBO = 0.216	Magneto- absorption	[115]

Valence Band Offset (VBO) (eV)	Measurement Type	Reference
Unstrained, Type-IIa, with x = 0.135, VBO = 0.130 with x = 0.09, VBO = 0.083	Magneto- PL	[48]
Type-IIa, $Q_c = \Delta E_c/\Delta E_g = 2.06 \pm 0.11$	Magneto-transmission	[57]
Type-IIa, $Q_c = \Delta E_c/\Delta E_g = 2.30$; $Q_v = -1.30$	PL	[60]
Type-IIb, for x = 0.07 – 0.14, 60% of E_g bowing in the valence band	PL	[50]
Type-IIb, for x = 0.05 – 0.13, 65% of E_g bowing in the valence band	PL and VBAC model	[51]
Type-IIb, for x = 0.14 – 0.27, ~60-70% of E_g bowing in the valence band	PL	[22]

APPENDIX C

MATERIAL PARAMETERS USED TO CALCULATE THE $InAs/InAs_{1-x}Sb_x$ SUPERLATTICE BANDGAPS

Parameter	Value	Unit	Reference
Effective Masses			
InAs			
Electron	0.023		
Heavy hole	0.41	m_o	
Light hole	0.026		[134]
$InAs_{1-x}Sb_x$			
Electron	$0.023 - 0.039 \cdot x + 0.03 \cdot x^2$		
Heavy hole	$0.41 + 0.02 \cdot x$	m_o	
Light hole	$0.026 - 0.011 \cdot x$		
InAs			
Electron Γ	0.026		
Heavy hole in z-dir	$1/(\gamma_1 - 2\gamma_2)$		
Heavy hole in [110]	$1/[½ (2\gamma_1 - \gamma_2 - 3\gamma_3)]$	m_o	[45]
Light hole in z-dir	$1/(\gamma_1 + 2\gamma_2)$		
Light hole in [110]	$1/[½ (2\gamma_1 + \gamma_2 + 3\gamma_3)]$		
Spin-orbit hole	0.14		
InSb			
Electron Γ	0.0135		
Heavy hole in z-dir	$1/(\gamma_1 - 2\gamma_2)$		
Heavy hole in [110]	$1/[½ (2\gamma_1 - \gamma_2 - 3\gamma_3)]$	m_o	[45]
Light hole in z-dir	$1/(\gamma_1 + 2\gamma_2)$		
Light hole in [110]	$1/[½ (2\gamma_1 + \gamma_2 + 3\gamma_3)]$		
Spin-orbit hole	0.11		
$InAs_{1-x}Sb_x$	Bowing factor		
Electron Γ	0.035		
Electron X	Linearly interpolate		[45]
Electron L	Linearly interpolate		
Heavy hole	Linearly interpolate		
Light hole	Linearly interpolate		
Luttinger Parameters			
InAs			
γ_1	20.0		[45]
γ_2	8.5		
γ_3	9.2		
InSb			
γ_1	34.8		[45]
γ_2	15.5		
γ_3	16.5		
$InAs_{1-x}Sb_x$	Direct linear interpolation NOT recommended		[45]
Lattice Constants			
InAs	$6.0583 + 2.74 \cdot 10^{-5} \cdot (T-300)$	Å	
GaSb	$6.0959 + 4.72 \cdot 10^{-5} \cdot (T-300)$	Å	[45]
InSb	$6.4794 + 3.48 \cdot 10^{-5} \cdot (T-300)$	Å	
$InAs_{1-x}Sb_x$	$a_{InAsSb} = (1-x) \cdot a_{InAs} + x \cdot a_{InSb}$	Å	

Parameter	Value	Unit	Reference
Elastic Constants			
InAs			
C11	832.9	GPa	[45]
C12	452.6	GPa	
b	-1.8	eV	
ac	-5.08	eV	
av	1	eV	
InSb			
C11	684.7	GPa	[45]
C12	373.5	GPa	
b	-2	eV	
ac	-6.94	eV	
av	0.36	eV	
$InAs_{1-x}Sb_x$	Linearly interpolate		
Bandgaps			
InAs	$0.417 - 0.276 \cdot 10^{-3} \cdot T^2/(T+93)$	eV	[45]
InSb	$0.235 - 0.32 \cdot 10^{-3} \cdot T^2/(T+170)$	eV	
InAsSb bowing factor ($C_{Eg\ InAsSb}$)	0.67	eV	
$InAs_{1-x}Sb_x$	$(1-x) \cdot E_{g\_InAs} + x \cdot E_{g\_InSb} - x \cdot (1-x) \cdot C_{Eg\ InAsSb}$	eV	
Spin-Orbit Energies			
InAs	0.39	eV	[45]
InSb	0.81	eV	
InAsSb bowing factor ($C_{bowing\ SO}$)	1.2	eV	
$InAs_{1-x}Sb_x$	$(1-x) \cdot \Delta_{SO\_InAs} + x \cdot \Delta_{SO\_InSb} - x \cdot (1-x) \cdot C_{bowing\ SO}$	eV	
Valence Band Offsets			
InAs	-0.59	eV	[45]
InSb	0	eV	
GaSb	-0.03	eV	
InAsSb bowing factor ($C_{Ev\ InAsSb}$)	0.65	eV	
$InAs_{1-x}Sb_x$	$(1-x) \cdot VBO_{InAs} + x \cdot VBO_{InSb} + x \cdot (1-x) \cdot C_{Ev\ InAsSb}$	eV	
Kane Potentials			
InAs	21.11	eV	[135]
InSb	23.3	eV	
GaSb	22.88	eV	
$InAs_{1-x}Sb_x$	Linearly interpolate	eV	

APPENDIX D

SUMMARY OF $InAs/InAs_{1-x}Sb_x$ SUPERLATTICE SAMPLES

Sample set 1 grown by MOCVD.

Sample Set 1	x ± 1 (%)	Thickness (nm)		Number of Periods X	Buffer layer thickness (nm)
		InAs	$InAs_{1-x}$ Sb_x		
A (3-2006)	22	7.0	3.3	100	100
B (3-2008)	23	7.0	2.3	50	67
C (3-2009)	37	7.0	2.0	50	85

Sample set 2 grown by MBE.

Sample Set 2	x ± 0.01	Period ± 0.5 (nm)	Number of Periods	GaSb Cap layer (nm)
A (0203-1)	0.27	26.5	20	100
B (0218-1)	0.28	24.6	20	100
C (0218-2)	0.29	24.6	20	100
D (0218-3)	0.33	24.5	20	100

Sample set 3 grown by MBE with ordered InAsSb alloys.

Sample Set 3	x ± 0.01	Period ± 0.5 (nm)	Number of Periods	Sb Duty Cycle (%)	No. of InAs/InSb periods per $InAs_{1-x}Sb_x$ layer	InSb (s)	InAs (s)
E (0221-1)	22	24.2	20	35	6	3	5.5
F (0221-2)	23	24.1	20	47	6	4	4.5
G (0221-3)	36	24.0	20	47	4	6	6.7

Sample set 4 grown by MBE with smaller periods and AlSb layers for confinement.

Sample Set 4	x ± 0.01	Period ± 0.5 (nm)	Number of Periods	Sb Duty Cycle (%)	No. of ½InSb/InAs/ ½InSb periods per $InAs_{1-x}Sb_x$ layer	½ InSb (s)	InAs (s)
H (0512-1)	0.30	7.4	60	N/A	N/A	N/A	N/A
I (0512-2)	0.13	7.4	60	33	2	1.5	6

Sample set 5 grown by MBE with AlSb barrier layers.

Sample Set 5	x ± 0.01	Period ± 0.5 (nm)	Number of Periods
J (2301027)	0.34	8.48	58
K (2301029)	0.37	8.40	58
L (2301030)	0.39	8.62	58
M (2301031)	0.35	10.72	47
N (2301032)	0.35	9.49	52
O (2301033)	0.28	24.47	20
P (2301043)	0.41	7.30	69
Q (2301044)	0.30	17.95	28
R (2301060)	0.35	9.79	209